Exploring TCR/CAR Antagonism from a Functional and Mechanistic Perspective

Sooraj Achar

DPhil Programme in Biomedical Sciences

Supervisors: Dr. Gregoire Altan-Bonnet, Prof. Michael Dustin

Balliol College, University of Oxford

Thesis submitted for the degree of Doctor of Philosophy

Trinity Term 2025

To Appa and Amma

Contents

Abstract

Chimeric antigen receptor (CAR) T cells have transformed therapy for blood cancers, yet their limited specificity has hindered success in solid tumors. In contrast, endogenous T cell receptor (TCR)–bearing T cells can distinguish neoantigen-positive tumor cells from healthy self-tissues, but typically lack robust antitumor potency. Here, we engineered a customizable robotic platform, named the IMMUNOtron, and a high throughput data processing pipeline, named plateypus, to decipher how these two receptors interacted with one another. We utilized the IMMUNOtron and plateypus to systematically stimulate CAR T cells that co-expressed a TCR and a CAR with different combinations of TCR and CAR signal strengths. These quantitative measurements allowed us to discover that strong TCR–antigen engagements potentiated CAR signaling, whereas weak TCR–antigen interactions suppressed activation. A mathematical model recapitulated this TCR/CAR crosstalk and guided the design of dual-receptor AEBS (Antagonism Enforced Breaking System) T cells recognizing neoantigens via the TCR and HER2 ligands via the CAR. When tested in a humanized solid-tumor mouse model, these dual TCR/CAR T cells showed superior antitumor efficacy with minimal damage to healthy tissues compared with conventional CAR and TCR T cells. A clinically translatable version of this construct that expressed a p53-R175H targeting TCR was able to display similar behavior even with endogenous levels of ligand. Exploiting intracellular crosstalk between immune receptors therefore could offer a path towards more precise and safer cancer immunotherapies.

Acknowledgments

I have to start by thanking my DPhil supervisors, Dr. Grégoire Altan-Bonnet and Prof. Mike Dustin, for being incredible mentors throughout my academic career. You both have too many impressive qualities to list, so I will keep myself to describing just one each. Grégoire, your willingness to get to get involved in the day-to-day minutiae of the lab was exceptionally motivating, especially during the painful early days of the lockdown when every available hand was needed just to keep equipment running. The technical adventure we had to undertake when installing the robot's fridge together will forever stand out to me as a highlight of my DPhil (along with your celebratory couscous). Mike, your wealth of knowledge about the history of immune signaling is truly impressive. At a certain point I should have stopped being surprised when you dug up specific experiments from thirty year old papers with incredible relevance to the topic at hand purely from memory, but I've continued to be astonished every time. I hope we will be able to find a way to continue to work together on future projects.

I also need to thank the fantastic set of collaborators I've had been lucky enough to work closely with over the course of my DPhil. First, I want to thank Dr. François Bourassa and his supervisor, Prof. Paul François from McGill University (and later University de Montréal). You both have been absolutely invaluable partners to have from the very beginning of my academic journey as we've worked our way from one high impact project to the next. The aspect of my work I'm perhaps most proud of is how closely we've managed blend theory and experiment throughout all of these projects, and this wouldn't have been possible without having such skilled yet understanding (of my own limited biophysics knowledge) theoreticians on our side. Secondly, I want to thank Dr. Taisuke Kondo and his supervisor, Dr. Naomi Taylor, for being a great set of clinical collaborators during the TCR/CAR antagonism project. Taisuke, your experimental skills are impressive all around, but I'm particularly inspired by your cloning expertise; I learn something new every time I look at one of your plasmid maps. I wish you the best of luck in your new position in Japan. Naomi, it's been great to work with you and various members of your lab throughout this project (and for numerous other FLEX grant projects that couldn't make their way into this thesis). It's been tremendously rewarding to see how our basic science work can make a direct clinical impact

through the projects your lab have been working on, and I hope the collaboration between your lab, Grégoire's lab, and of course the IMMUNOtron will continue in the future.

Next, I want to thank all of the lab colleagues that have supported me in both the Altan-Bonnet and Dustin labs. Emanuel, it's been a pleasure to work alongside you in Grégoire's lab since we both started there seven (!) years ago and see you develop your project from ground zero to an (almost) completely published, high impact, story. I still miss our lunchtime chats; they're a huge part of why I was able to stay (mostly) sane during lockdown. I'm excited to see how you'll be able translate your computational and experimental talent to industry. Dongya, it's been great to go on a variety of journeys with you, both scientifically and travel wise. Really glad we both got the opportunity to play the part of tour guide during our joint conference trips to Shenzhen and Oxford. Adam, it's been very rewarding to see you turn marQup from a python package I coded during my DC metro commutes into a full fledged scientific paper. Best of luck at Mt. Sinai, the great thing about your MD/PhD is that you won't be going anywhere for a while so I'll get to visit you often in NYC. Ed, it's been great to learn about the finer details of microscopy from you, as well as go on various culinary expeditions together. I'm excited to see how you'll push the TCR/CAR antagonism project in new directions, and wish you the best of luck as you prepare to start your own lab. We've still got to find a way to get through a round of croquet before you leave though!

Finally, I want to thank all my friends and family who've supported me on this journey. There are too many names to list properly here but I will do my best: thanks to Andrew, Philip, Adithya, Jonny, Chloe, Steve, Erika, and Taylor for making sure I remembered to have fun outside the lab during my time at the NIH; thanks to Sini, Ashley, Poorva, Corinne, Yasmin, Lauren, Jackson, Emery, John, and the rest of the NIH/Oxford crew for allowing me to pretend I was still in the US during my time at Oxford; and of course thanks to Siddarth, Amma, and Appa for making sure I felt welcome every time I visited home. It truly takes a village to get through a DPhil, and you all made for about the best transatlantic village I could have asked for.

Prior DPhil publications

The IMMUNOtron robotic platform, control software, and plateypus analysis pipeline from Chapter 1 were first described in [1]. All results from Chapters 2-4 were first communicated in [2], with the exception of the data in Figure 23 in Chapter 2, which was first communicated in [3], and the marQup pipeline used to process the bioluminescence data in Figure 54, which was communicated in [4].

Author contributions

The projects detailed herein stem from highly interdisciplinary collaborations. The bulk of the thesis focuses on my original contributions but I also include several figures created by other co-first authors in order to generate a complete story. Figures 2,3,4, and 5 in the introduction were made by Dr. François Bourassa for a submitted review article we wrote together, and Figures 24 and 33 in Chapter 3 were made by Dr. François Bourassa for [2] and modified to fit this thesis. The code in Chapter 2 is primarily the result of my own work, with key contributions from Madison Wahlsten for the IMMUNOtron-Interface. In Chapter 2, Dr. Taisuke Kondo manufactured the B16-CD19 cell lines as well as the mouse CAR T cells used for experiments, and collected the *in vivo* survival, tumor size, and specific killing data. All *in vitro* data as well as all *in vitro* and *in vivo* analysis in Chapter 3 was generated by me, while all theoretical modeling was performed by Dr. François Bourassa. In Chapter 3, Dr. Kondo manufactured the human NYESO-TCR/CD19-CAR T cells, and Dr. Pablo Cespedes performed the experiments, with analysis by Dr. Audun Kvlaag and Dr. Edward Jenkins. In Chapter 5, Dr. Taisuke Kondo manufactured all tumor cell lines used for experiments as well as the human AEBS CAR T cells used for experiments, and performed all *in vivo* experiments. All *in vitro* data in Chapter 5 was collected by me, with the exception of the Incucyte cytotoxicity measurements, and any experiments relating to the p53 TCR/HER2 CAR AEBS construct. All *in vitro* and *in vivo* analysis in Chapter 5 was conducted by me, while all theoretical modeling was performed by Dr. Bourassa. The first draft of the publication [2] detailing these results was primarily written by Dr. Bourassa and I, with input from all authors for subsequent drafts.

1 Introduction

1.1 Structural vs kinetic explanations for T cell receptor function

T cells, a key component of the adaptive immune system, primarily rely upon a single receptor, the titular T cell receptor (TCR), to distinguish between friend ("self") and foe ("nonself") when surveying the body for threats. The degree to which the TCR can discern between self and nonself antigens is therefore of paramount importance to the overall functionality of the immune system. Previous studies comparing the T cell receptor to other common recognition receptors have shown that the TCR is uniquely proficient at being able to distinguish between very similar antigens [5]. What features of the TCR and its associated signaling network could be responsible for the singular discriminatory capabilities of the TCR? Two competing explanations are described in Figure 1 below.

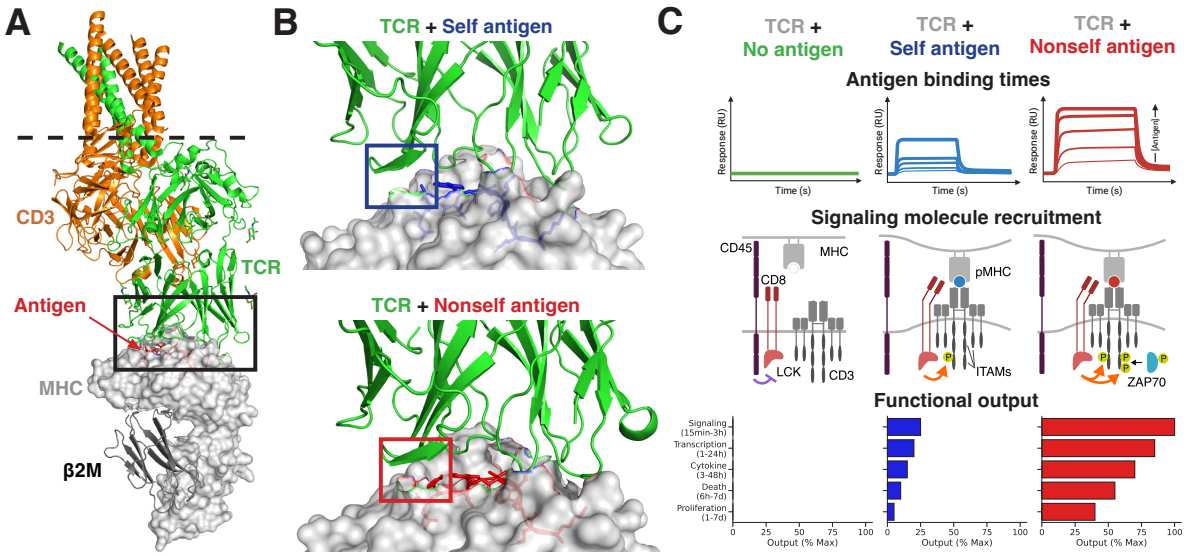

Figure 1: **Overview of TCR Signaling.** (A) Structure of a TCR interacting with Class I pMHC, the initial step for T cell activation (PDB structure 7PHR from [6]). (B) Close-up and comparison of the presented peptides for anagonist neo-antigen (PDB: 6UK2) and its wild-type counterpart (PDB: 6UK4) from [7]: note that, despite structural similarities, the neo-antigen pMHC is a 20-fold better binder to TCR compared to the self pMHC, and 1000-fold more potent in activating T cells. (C) Sketch of the biophysical/functional characteristics of ligand discernment by TCR. We sketch 3 discrete categories of antigen (no antigen, self antigen, neo-antigen) that do not bind at all, or bind mildly and strongly respectively (top), inducing increasing degrees of phosphorylation on the TCR and associated proteins (center) with different functional outputs (bottom).

Figure 1A displays the major structural components of the T cell receptor and other directly

interacting proteins. The core component of this complex is the TCRab heterodimer and colocalized CD3 molecules (two CD3ϵ chains, two CD3ζ chains, a CD3δ chain, and a CD3γ chain). These associated chains harbor, on their intracellular segments, dual phosphorylation sites known as immunoreceptor tyrosine-based activation motifs (ITAMs), which consist of short amino acid sequences containing two phosphorylatable tyrosines. Each ϵ, δ, and γ chain contains one ITAM, while each ζ chain has three, summing up to a total of 10 ITAMs and therefore 20 phosphorylatable tyrosines.

This type of complexity in the T cell receptor's associated signaling complex would, at first glance, seem to point towards a simple structural explanation for the excellent antigen discriminatory powers of the TCR, as detecting a conformational shift in the TCR recognition domain upon engagement with agonist pMHC could account for multiple facets of T cell behavior at once. As an intramolecular process, such conformational shifts could occur within milliseconds, aligning with the rapid onset of T cell activation. In addition, single–amino-acid substitutions in MHC-presented peptides could plausibly drive large, specific conformational changes in the bound TCR (as observed during antibody affinity maturation against soluble antigens in B cells), explaining how even a single peptide–MHC complex is sufficient to trigger a T cell response [8]. In addition, other structural explanations that do not require large conformational changes in TCR structure have also been published. These studies revolve around how the amount of mechanical force required to overcome differing levels of "catch bond" formation (on a per TCR baseis) could potentially allow the TCR to differentiate between antigens [9]. Yet these types of purely structural explanations fall short of other observations. First, TCR ligand discrimination is highly tunable: the same ligand set can function as agonists, partial agonists, or non-agonists depending on the T cell's differentiation state; specificity can swing from broad, to sharply selective, and back to broad as T cells mature. Second, recent cryoEM analyses have not revealed substantive conformational rearrangements in the TCR$\alpha\beta$ dimer, even under activating conditions (Figure 1B). Third, biophysical work with engineered systems, either expressing TCR components in non-T cells [10] and/or deploying synthetic receptors with nucleic-acid-based ectodomains and TCR-derived intracellular domains [10], has demonstrated robust ligand discrimination despite the absence of catch bonds.

What other, non-structural, features differ among antigens upon TCR engagement? A partic-

ularly prominent difference is the lifetime (dwell time) of the TCR–peptide–MHC complex, which can differ markedly between weak self antigens and strong nonself antigens (Figure 1C top). A recent study provides compelling evidence that antigen lifetime, rather than conformation, is pivotal in T cell decision-making. Britain et al. [11] introduced a next-generation optogenetic platform, building on [12], in which increasing blue-light intensity raises the effective unbinding rate between a ligand and an engineered receptor without altering the bond's mechanical behavior under load. They observed a tight correlation between T cell activation and ligand half-life across 0.5–10s (the physiological range for TCR antigens [13]) with little dependence on receptor occupancy. These findings support a model in which TCR discrimination hinges on binding lifetime, rather than on mechanical sensing, catch bonds, or conformational shifts.

1.2 Combinatorial complexity of TCR phosphorylation patterns

This type of biophysical understanding of TCR ligand discernment based on the kinetics of ligand–receptor complex dissociation would offer a more universal, flexible and actionable explanation for the TCR's unique antigen discernment capabilities, but there still remains a central question: How are the relatively small differences in the lifetime of the TCR/pMHC complex translated into large differences in T cell activation?

Surveying the biochemistry of the TCR signalosome highlights the abundance of tyrosines within the complex, particularly across its ten CD3 ITAMs (Figure 1C). Early efforts to parse how multisite phosphorylation shapes signaling suggested a role in TCR ligand discrimination. Kersh et al. [14] generated antibodies recognizing distinct phospho-peptides corresponding to different states of the CD3ζ chains. Using these reagents, they showed that CD3ζ is phosphorylated in a stepwise manner, with higher-potency antigens driving access to additional phospho-states, leading them to conclude that CD3ζ phosphorylation can impose multiple activation thresholds that underlie precise ligand discernment. Subsequent work by Aivazian and Stern [15] revealed that CD3ζ reversibly associates with—and dissociates from—the plasma membrane upon phosphorylation. In this model, prior to antigen engagement, CD3ζ embeds within the lipid bilayer, making brief excursions into the cytoplasm. Upon TCR–pMHC binding, Lck is recruited to the engaged TCR, phosphorylates CD3ζ during one such cytoplasmic excursion, and stabilizes this domain away from the membrane,

enabling engagement of downstream signaling partners (such as ZAP70, LAT etc.), (Figure 1C center). This elegant framework, corroborated by more recent cryoEM structural analyses, accounts for the sequential character of TCR phosphorylation, a cornerstone of ligand-discrimination fidelity. Pitcher and van Oers [16] proposed that the combinatorial and ordered phosphorylation of the TCR–CD3–associated chains can channel signaling into distinct downstream pathways. Consistent with this idea, Voisinne et al. [17] employed mass spectrometry to chart phosphorylation patterns within the TCR signalosome triggered by ligands of differing immunological potency. By carefully titrating ligands to equalize receptor occupancy, they uncovered a hierarchical set of phosphorylation states that tunes the stoichiometry of TCR-associated proteins, with CD6 acting as a critical negative regulator that constrains responses to weak ligands. Such a nested assembly of the TCR signalosome plausibly maps onto nested functional outputs in T cells (e.g. differentiation, cytokine production, and proliferation). Thus, the existence of many phosphorylated states may explain how T cells appropriately multiplex their responses in response to different levels of stimulation (Figure 1C bottom).

1.3 Kinetic proofreading

Importantly, the idea that successive phosphorylation states are responsible for mediating the antigen discernment powers of the TCR not only fits experimental data qualitatively well, but also can be adapted into a robust quantitative theoretical framework for improving biological error correction called kinetic proofreading. Kinetic proofreading is a process where ligand/target binding triggers a succession of time-consuming modifications of the target until an end state is reached. Only targets that have reached this final state contribute to further signaling, which greatly improves the specificity of the interaction beyond what simple binding affinity between the ligand/receptor alone would predict. This process was first described by [18] and [19], and has now been tied to a variety of other biological phenomenona where minimizing erroneous binding events is critical, including ribosomal decoding [20], DNA replication [21], and pre-mRNA splicing [22]. The first application of this process to explain characteristics of T cell receptor/antigen binding was made by Mckeithan et al. in [23], and helped explain how small differences in antigen unbinding rates could be amplified into large differences in T cell activation.

Since Mckeithan's initial proposal, many lines of experimental and theoretical evidence have arisen to support the involvement of a kinetic proofreading mechanism in T cell activation. In addition to the previously described recent optogenetic experiments, classic perturbations of pMHC binding kinetics showed that the duration of TCR–pMHC engagement, rather than occupancy, better predicts activation, consistent with KPR's time-gated progression [24]. Subsequent work formalized how fast on-rates can enable effective rebinding to extend apparent dwell time and thereby meet proofreading thresholds even for ligands with modest single-encounter lifetimes [25]. In model selection on large response datasets spanning multiple orders of magnitude in dose and affinity, architectures that embed KPR at the receptor (combined with simple network motifs) best reproduce observed levels of discrimination, antagonism, and bell-shaped dose responses [26]. Taken together, these results support the idea that kinetic proofreading is a critical component of TCR signaling.

If KPR is indeed the mechanism underlying the superb antigen discernment capabilities of the TCR, what type of biochemical event is responsible for initiating the chain of phosphorylation reactions? There are again two prominent competing theories in this area: conformational change and kinetic segregation. The conformational change hypothesis (CC) states that small differences in the conformational structure of the TCR upon pMHC binding (for example the movement in the β strand towards the tumor neoantigen boxed in Figure 1B bottom compared to Figure 1B top) modify ligand off rates to a sufficient degree to allow for different levels of TCR signaling to be achieved [27]. Meanwhile, the kinetic segregation (KS) hypothesis posits that the true triggering event for TCR signaling stems from the exclusion of key inhibitory molecules (such as CD45 phosphotases) from the immune synapse during the early stages of T cell activation due to steric differences between molecules [28]. In brief, this theory states that at homeostasis, CD45 phosphotases cluster closely together with other key components of the initial TCR activation complex (such as the coreceptors CD8 and CD4, and the associated Lck signaling molecule), dephosphorylating them and therefore preventing the coreceptors+Lck from initiating TCR phosphorylation. However, because the surface exposed region of CD45 is much taller than the combined surfaced exposed regions of a TCR + pMHC, when a T cell produces an area of close contact with an APC during initial intercell engagement, CD45 is pushed away, or kinetically segregated, from this

close contact region, allowing the CD8/CD4 coreceptors+Lck to initiate the TCR phosphorylation cascade.

Both theories offer reasonable explanations for a TCR triggering event, and often can be adapted to produce very similar outcomes to one another in terms of final functional output upon TCR engagement, but there are certain key differences between the model that can be tested experimentally. For example, the KS model implies that T cells can be induced to signal in the absence of any ligand binding to the TCR, simply by excluding CD45 phosphotase. This phenomenon does seem to occur both in synthetic [29] and natural [30] settings, lending support for this hypothesis. In addition, recent computational results have shown that kinetic segregation + kinetic proofreading produces experimental predictions of ligand activity that are much more in line with experimentally measured EC50s than conformational change + kinetic proofreading [31]. These types of results led the authors to conclude that the KS-KP model has a firmer body of evidence to support its validity currently, though they also take the view that the two hypotheses are likely endpoints of a spectrum, and that both are likely involved to a certain degree in T cell activation.

1.4 Adaptive Kinetic Proofreading

While the KS-KP model of T cell activation can explain many of the features foundational to TCR antigen discrimination, there are still several components to TCR signaling that it struggles with capturing. The most prominent example is a phenomenon known as absolute ligand discrimination. In essence, in the context of TCR activation, absolute ligand discrimination refers to the idea that antigens weaker than a certain affinity will never induce signaling regardless of how densely they are presented on a surface of a cell. In other words, there is a threshold of antigen quality where it can no longer be compensated for through quantity. A summary of the issues with KPR with regards to absolute ligand discrimination is shown in Figure 2 below.

The self ligands a T cell typically encounters have very weak affinities to any given TCR clone in the periphery due to active pruning of TCRs with high affinities to self antigens during the negative selection phase of T cell development in the thymus, but many of these antigens are still seen at very high densities. An analysis of pMHC frequency data for self ligands from a recent immunopeptidomics study [32] revealed that the distribution of the top 1000 peptides in terms

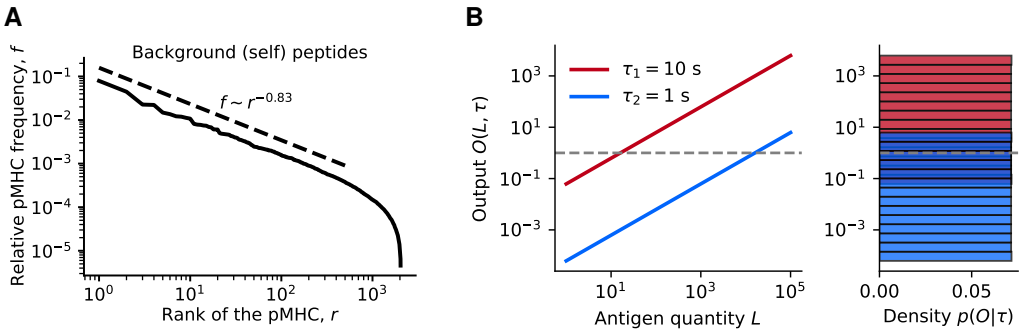

Figure 2: **KPR cannot produce absolute ligand discrimination** (A) Relative frequency distribution of class I peptide MHCs on the surface of antigen presenting cells (melanoma cells here). Replotting "background peptides" (self) data in the "DMSO" control condition, averaged over three repeats, from figure 1D of [32]. We notice a power-law behavior for the first 103 peptides, followed by a sharp cutoff. Of note, these abundances are approximate, based on direct spectrometry readouts that may be biased by, e.g., unequal processing efficiencies in the mass spectrometry pipeline for different peptides [33]. (B) Illustration of the antigen quality discrimination problem. (Left) Pure KPR model (N = 4, phi = 0.1) output curves for two antigen qualities (red: τ_s = 10s, blue: τ_s = 1s) over a wide range of antigen quantities L. (Right) Marginalization of the TCR output distribution over the range of L, to obtain p(O given τ). With an absolute discernment model, these distributions would not overlap for different antigens

of frequency follows a surprisingly strict power law relationship, where many self antigens have have very similar (and high) frequencies (Figure 2A). The total pool of self antigens available to interact with a given TCR at weak affinities is therefore quite large, meaning that absolute ligand discrimination is critical for proper functioning of all TCRs during self/nonself discrimination. Conventional KPR (with signaling initiated through either KS or CC) cannot produce absolute ligand discrimination, as its output varies linearly with antigen quantity, causing even very weak antigens to eventually pass the activation threshold when they are presented at a high enough density (Figure 2B left). This leads to a large number of densities where weak and strong antigens cannot be easily distinguished by TCRs operating under a KS-KP signaling regime, as displayed in Figure 2B right.

An initial solution to this issue was produced by the landmark theory/experiment study of Altan-Bonnet and Germain, which introduced a new systems-biology model of T cell activation [34]. The detailed biochemical network is essentially a kinetic proofreading scaffold with two principal extensions.

First, TCRs are coupled through the phosphatase SHP-1, activated by an early intermediate in the proofreading cascade and capable of dephosphorylating TCR complexes. This implements negative feedback, in line with experimental evidence for inhibition and antagonism mediated by SHP-1 [35] and partially phosphorylated ITAMs [36, 37, 38, 39]. Previous work using artificial dual TCR cells [40, 41] had even shown this type of inhibitory interaction could occur across receptors.

Second, the terminal step of the proofreading cascade activates a MAP kinase that ultimately drives ERK phosphorylation, which then self-activates and suppresses the SHP-1–dependent inhibitory loop [42]. This composite model achieves absolute discrimination as a function of antigen quality, predicting a critical binding time (around $\tau_c = 3$ s) below which even high antigen doses fail to elicit a response. The activation threshold can be shifted by modulating intrinsic ERK signaling, SHP-1, or CD8 levels, with model predictions matching observed cell-to-cell variability—for example, antigen responses are lost in T cells whose SHP-1 levels are a few-fold above the wild-type average ([43]). Thus, adding feedback loops to KPR appears to solve the difficult problem of how TCRs discriminate antigen independently of ligand quantity.

To clarify key mechanisms, Lipniacki et al. reduced the complex model from [34] to 37 rate-equations that could reproduce its important properties and capture stochasticity in individual T cells exposed to similar antigens. Yet, the size of their network still obfuscated deeper understanding of ligand discernment. In [44], a phenomenological model, further simplifying the biochemical network, was proposed and analytically studied. The model includes a negative feedback with a dephosphorylation reaction b + y_S, where S is a pool of active SHP-1 phosphatases shared between receptors, negatively coupling them. The phosphatase is activated by receptors in the first proofreading state, C1. A schematic of this simplified model is shown in Figure 3 below:

The phenomenological model in 3A reproduces the predictions of the original Altan-Bonnet and Germain framework [34], and continues to produce absolute antigen discrimination ac ross a broad range of antigen quantities (Figure 3B). Building on this insight, Lalanne and François [45] used evolutionary algorithms to derive minimal biochemical networks that optimize the mutual information between different quality antigens measured at multiple ligand densities.They identified multiple KPR-based architectures with kinases and phosphatases implementing feedback, all achieving comparable mutual information. In their most streamlined form, these reduce to a KPR

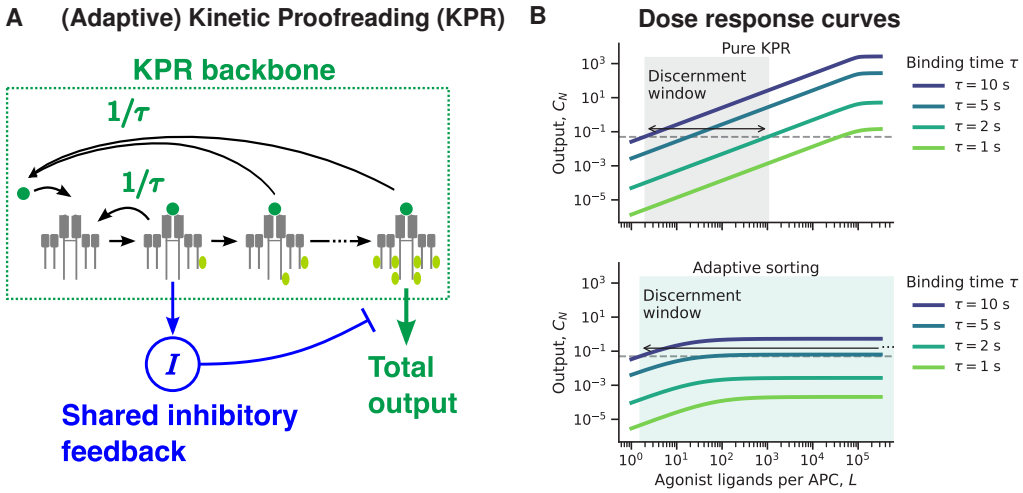

Figure 3: **Adding negative feedback to KPR improves ligand discrimination** (A) Core reactions in Adaptive Kinetic Proofreading (AKPR) models, which consist of a KPR backbone and an inhibitory feedback module. (B) Model response curves to single antigen types for KPR without (top) and with (bottom, N = 6) negative feedback reveals a much larger antigen "discernment window" (the range of L over which the response is above threshold for agonists (τ = 10 s) but remains below for self-like ligands (τ = 2s)) after the addition of negative feedback.

cascade whose terminal reaction is carried out by a kinase K that is inactivated by an intermediate complex Cm. In such models, when L is sufficiently large to generate strong feedback, antigens with different τ values settle into distinct plateaus of CN activation at ligand doses L Rtot well below receptor saturation (Figure 3B). An incoherent feedforward loop (IFFL) emerges within the KPR cascade [46] of these models, because Cm exerts both a positive effect (through the KPR chain) and a negative effect (through K) on CN. Such IFFLs are well known features of biochemical adaptation networks [47], and accordingly this class of models ranks antigens by quality τ while *adapting* to (i.e., compensating for) quantity L. We therefore refer to these augmented KPR schemes as Adaptive Kinetic Proofreading (AKPR) models.

1.5 Antagonism

As a side effect of the additional negative feedback incorporated into their mathematical structures, all AKPR models display an important and biologically relevant property known as antagonism: ligands below the detection threshold (i.e., not producing a response on their own, so potentially self-like) can hinder (antagonize) activation by ligands above the threshold of activation. A summary

of the differences between single ligand and dual ligand stimulation in AKPR class models is shown in Figure 4 below.

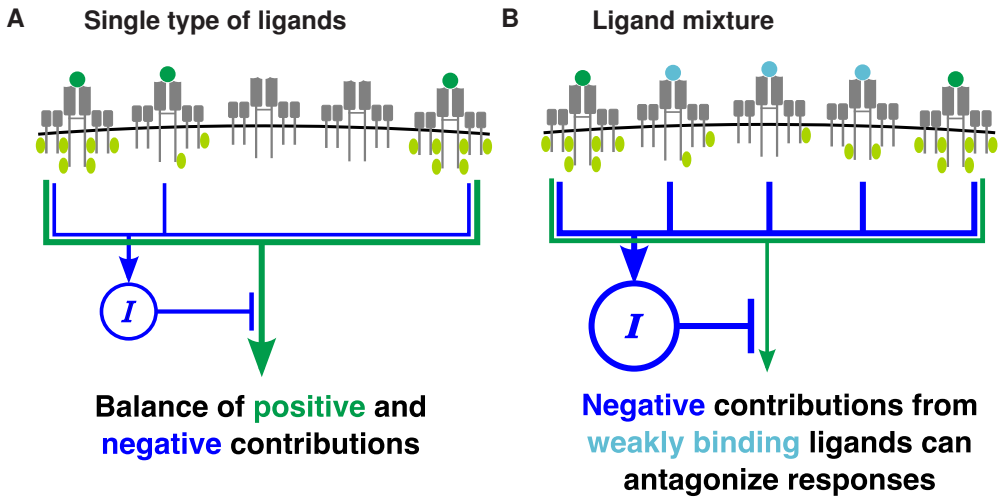

Figure 4: **Antagonism is unavoidable in an AKPR class model** (A) Illustration of single antigen responses, where the output is set by the balance of activating and inhibitory signals triggered by the antigen. (B) Illustration of antagonism: weak ligands cannot reach the activated proofreading state, but can trigger the negative feedback. Receptors bound to strong antigens are coupled to this inhibitory module and are thus inhibited, hence lowering the overall cell activation.

Antagonism is a familiar feature of many biochemical sensing systems [48]. Torigoe et al. [49] invoked the Aesop fable of the "dog in the manger" to describe an analogous effect for immunoglobulin E receptors (which are related to TCRs). In the story a dog prevents a hungry horse from eating grain, despite not being able to eat grain itself. In a similar way, antagonist ligands actively block agonists from triggering a response while producing little response of their own, as illustrated in Figure 4B. In contrast, classical KPR formulations do not display antagonism, underscoring a fundamental predictive limitation of models lacking feedback. It has since been proven mathematically that antagonism is in fact an unavoidable byproduct (an evolutionary "spandrel") of absolute discernment [50].

Antagonism can also help distinguish different classes of adaptive sorting models from one another, as shown in Figure 5 below.

The behavior of many of the adaptive sorting model types described above in response to single ligand stimulation can look qualitatively similar, especially at the low ligand densities typical of physiological scenarios (Figure 5A) [51]. However, by measuring antagonism in different AKPR

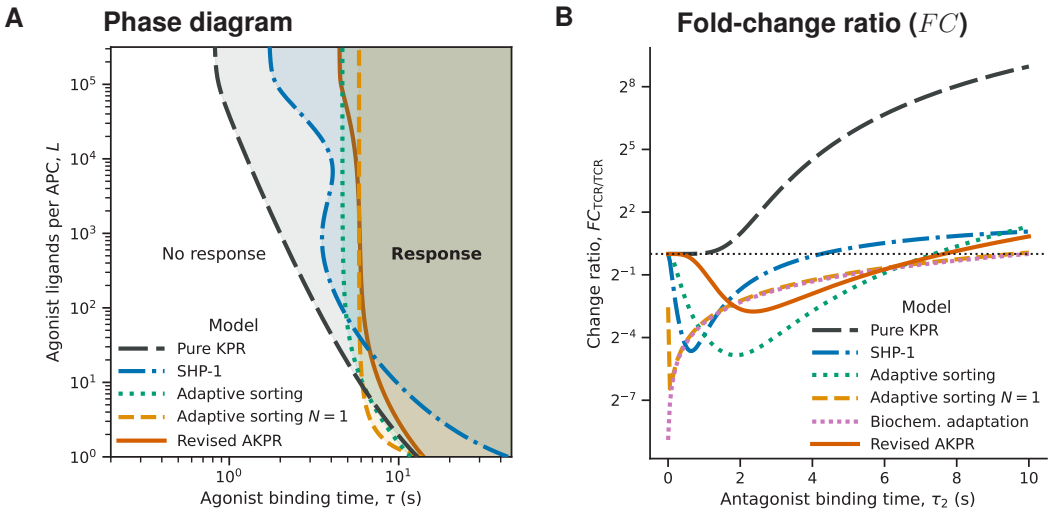

Figure 5: **AKPR models show significant differences in antagonistic behavior** (A) Phase diagram of the immune response predicted by different models. The decision boundary is built by setting a threshold for activation on the model output C_N, and computing for every antigen quantity L what antigen τ would be necessary to reach the threshold at that dose. (B) Fold-change (FC) antagonism curves of different models, in the presence of $L_1 = 10$ agonists of $\tau_1 = 10$s, and $L_2 = 5 \times 10^3$ antagonist ligands with τ_2 given by the horizontal axis.

models using a ratio of dual antigen (agonist+antagonist) signal to single antigen (agonist) signal, we notice that the quantitative details of these curves can vary considerably (Fig. 5B). We can then determine which of these models most accurately describes the true biology underlying T cell activation by comparing their results to experimental data.

The first experimental reports of TCR antagonism appear in the early 1990s, where De Magistris et al. [52] report that antigen presenting cells pulsed with two different affinity ligands could elicit a lower functional response in CD4+ T cells than antigen presenting cells presenting only a single affinity ligand. This observation was later expanded on in 1993, where Alexander et al. [53] created a library of mutated variants of the endogenous hemagglutinin antigen, and showed that these peptide variants could be divided into four distinct classes based on how they caused a T cell to behave when combined with an strong TCR signal: null (has no effect on strong TCR signal), antagonist (can only reduce strong TCR signal), partial agonist (can increase or reduce strong TCR signal depending on ligand density), and agonist (can only increase strong TCR signal). Another study that same year [54] revealed that antagonism could reduce multiple markers of T cell activation (CD25, proliferation, calcium influx), but that antagonism could not be observed

when the agonist and antagonist peptides were placed onto different cells. Shortly afterwards, Jameson et al. showed that antagonism could affect CD8+ T cells as well [55] using combinations of stimulations utilizing ovalbumin altered peptide ligands. This observation allowed several other labs to discover that natural altered peptide ligands derived from HIV could act as antagonists [56, 57], showing for the first time that TCR antagonism had the potential to play a role in human disease. At around the same time, Franco et al. showed that antagonism could be used for therapeutic purposes to reduce experimental autoimmune encaphalitis in a murine model [58]: mice immunized with an antagonist peptide and an adjuvant showed reduced levels of disease compared to those immunized with an adjuvant alone. Several years later, Basu et al. [59] showed that antagonism could be observed *in vivo* using entirely endogenous antagonist signals. This flurry of research into antagonism culminated in the initiation of several clinical trials that attempted to use antagonism to help control the autoimmune reactions underlying multiple sclerosis [60, 61].

Disappointingly, these trials were largely unsuccessful due to excessive adverse events, partly due to unexpected cross reactions between the antagonist peptide and other TCR clones present within the patient [60]. Research interest in antagonism as a therapeutic tool dropped sharply after the publication of these negative clinical results. Although there has continued to be research focused on better understanding the theoretical underpinnings of antagonism [34, 44], and the signaling mechanisms driving the phenomenon [62], there is a noticeable lack of recent studies attempting to apply antagonism to the treatment of disease. Particularly surprisingly, almost no work has been done examining antagonism in the context of an oncology treatment known as chimeric antigen receptor (CAR) T cell cancer immunotherapy.

1.6 CAR T cell immunotherapy

CAR T cell therapy is a form of cancer immunotherapy where a patient's own immune cells are reprogrammed to target cancer through insertion of a chimeric antigen receptor (CAR) recognizing a tumor specific protein. The basic components of CAR T cell therapy are shown in Figure 6 below.

Contemporary CARs typically combine an antibody-derived binding domain (single-chain variable fragment) with intracellular signaling modules (CD3ζ plus co-stimulatory domains such as CD28 or 4-1BB) to trigger potent, antigen-specific T-cell activation upon contact with cancer

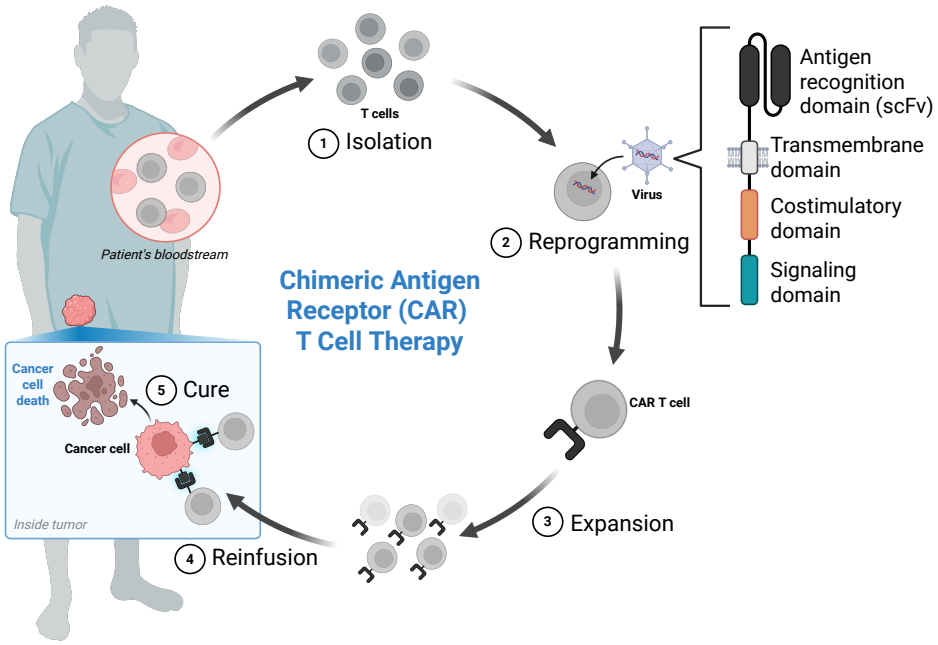

Figure 6: **CAR T cell immunotherapy.** Outline of conventional CAR T cell manufacturing and treatment protocol (left) and structural components (right)

cells. This design has produced deep and sometimes durable remissions in patients with otherwise treatment-refractory disease [63]. The first clinical breakthough that used CAR T cell immunotherapy came in CD19-positive B-cell malignancies. Early academic reports in adults with chronic lymphocytic leukemia and in children with acute lymphoblastic leukemia showed dramatic responses [64], laying the groundwork for subsequent multicenter trials. In a pivotal study of tisagenlecleucel in children and young adults with relapsed/refractory B-cell ALL, high response rates and sustained remissions established CAR T cells as a new standard for this population [65]. The positive results of this clinical trial led to numerous additional studies that aimed to apply CAR T cell therapy to new disease indications. As of August 2025, multiple autologous CAR T-cell products are FDA-approved for hematologic cancers, targeting CD19 (e.g., certain lymphomas, ALL, mantle cell lymphoma) and B-cell maturation antigen (BCMA) in multiple myeloma, reflecting broad uptake of the platform in blood cancers.

However, despite the remarkable success CAR T cell therapy has shown against liquid tumors, extending its benefits to cancer types beyond hematologic malignancies has proven to be a challenge. Solid tumors pose numerous additional hurdles to cell based immunotherapy: scarce truly tumor-

specific antigens, hostile tumor microenvironments, trafficking barriers, and antigen heterogeneity [66, 67]. Researchers have attempted to circumvent these hurdles by implementing innovative modifications to conventional CAR T cell therapy [68], such as armored CARs [69], logic-gated designs [70, 71], *in vivo* delivery [72], and combinations with other agents [73].

Parallel efforts are exploring allogeneic "off-the-shelf" CAR platforms and CAR-engineered NK cells to improve scalability and timeliness of treatment [74]. Allogeneic CAR T cells aim to decouple efficacy from the logistics of autologous manufacturing by banking donor-derived, gene-edited T cells that can be delivered on demand [75]; early clinical experiences now include a variety of anti-CD19 products, with response rates and manageable safety demonstrated across phase 1 programs [76, 77, 78, 79]. These products employed several different strategies to overcome the two central immunologic hurdles for allogenic CAR T treatment: graft-versus-host disease (GvHD) and host-versus-graft rejection. The gene-editing playbook used to address these issues primarily relies disrupting the T-cell receptor (typically via TRAC knockout) to prevent GvHD, removing CD52 to enable alemtuzumab-based lymphodepletion, and reducing allo-recognition by modulating HLA class I, often through β2-microglobulin (β2M) disruption combined with HLA-E expression to blunt NK-cell attack. Proof-of-concept for this strategy began with TALEN-edited UCART19 (TRAC and CD52 knockouts) [76] that induced clinical remissions in infants and was later expanded to adult cohorts. Additional clinical entrants include CRISPR-edited CTX110 [78] and CB-010 [79], the latter integrating the CAR into TRAC and knocking out PD-1 to limit exhaustion. Intriguingly, despite the critical importance of the endogenous TCR in the success of allogenic CAR T cell treatment, its exact role in CAR T cells has not yet been clarified. While precise TRAC-locus CAR insertion (which ablates TCR expression) improved potency and standardized CAR expression in preclinical models [80], other work found endogenous TCR-retaining CAR T cells could persist longer *in vivo* than their TCR-knockout counterparts [81].

How can we explain these seemingly contradictory results? Our prior experience with AKPR and antagonism led us to hypothesize that the level of signal the TCR received during CAR T cell stimulation could cause differential effects on treatment efficacy. Recently published work, shown in Figure 7 below, seemed to support this hypothesis, as preliminary results in this study that suggested there could be crosstalk between the CAR and TCR in during CAR T cell immunotherapy.

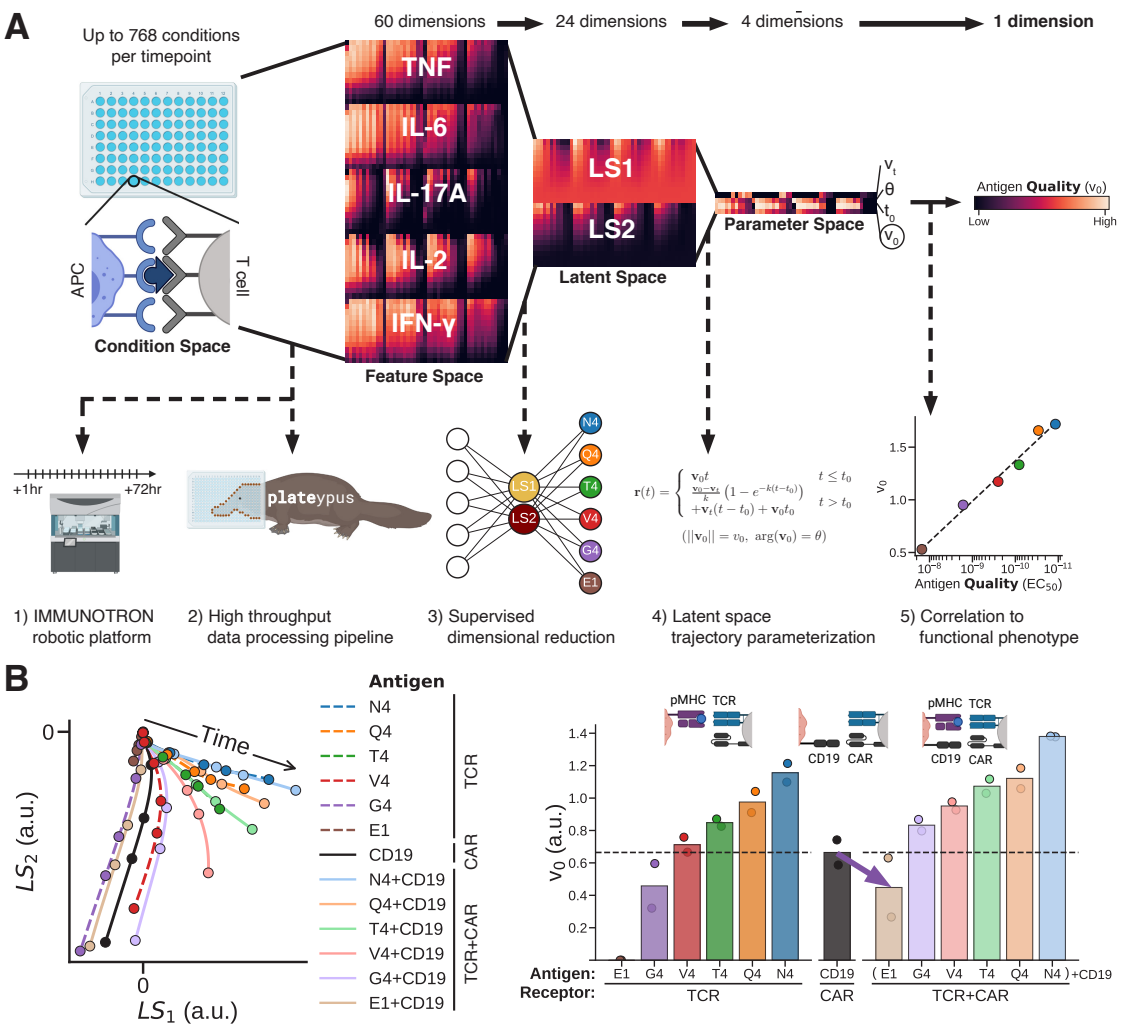

Figure 7: **Hints of TCR/CAR antagonism.** (A) Schematic of antigen encoding pipeline to deconvolve high throughput T cell activation data. (B) Antigen encoding of anti-CD19 CAR-T cells (left) revealed a pattern of weak activation and antagonism for cytokine responses (right, purple arrow).

Figure 7A describes the basic computational and experimental pipeline used in this work (termed an "antigen encoding" pipeline) to develop a robust, density agnostic measure of T cell activation. Figure 7B shows that the level of this metric measured in an OT1/CAR T cell stimulated with both the lowest affinity TCR signal (E1) and a CAR signal (CD19) is indeed lower than the overall cytokine level produced by a OT1/CAR cell receiving stimulation through its CAR alone. This data further indicates that antagonism is unlikely to be the result of ligand competition, as the antagonist and agonist signal are now associated with two independent ligand/receptor systems with very little cross-reactivity. My thesis work therefore sought to follow up on this initial

observation to better understand this novel form of cross-receptor interaction.

2 Developing a cheap, high throughput method of surveying multiplexed readouts of T cell activation

2.1 Introduction

Upon recognition of a foreign antigen (or two foreign antigens in our case), T cells alter their behavior in a variety of different ways. To quantify the strength of this antigen/cell interaction, immunologists have long relied upon measuring the dose of peptide required to elicit a half maximal response of a readout of T cell activation. While this metric, termed an EC50, can indeed be useful, the diversity of activity a T cell undergoes upon antigen recognition makes it exceedingly difficult to use any single readout to measure overall cell activation. Numerous studies have shown that different readouts saturate at different levels of activation, making the choice of a single readout at a single timepoint insufficient to accurately characterize the level of stimulation a T cell receives across a wide range of densities. To circumvent this problem, we constructed a robotic platform, named the IMMUNOtron, wrote an easily customizable wrapper for the robot's software called the IMMUNOtron-Interface, and programmed a high throughput data analysis package, named plateypus, that allowed us to cheaply and effectively collect large sets of data from dual ligand T cell activation assays.

2.2 Robotics: IMMUNOtron

2.2.1 Physical design

The IMMUNOtron is a semi-custom Freedom Evo 100 robotic platform purchased from Tecan, and is designed to automate collection of highly multiplexed readouts of T cell activation dynamics. To accomplish this goal, it is equipped with two programmable robotic arms: a robotic manipulator arm (RoMa) responsible for moving other components around the robot's workbench, and a liquid handling arm (LiHa) responsible for all pipetting actions. The other automated components on the workbench are an incubator and fridge sourced from Liconic, which both contain 44 individual shelves split across two hotels within them as well as transfer stations to interface with the main workbench, and a tabletop centrifuge sourced from Agilent. The workbench itself contains several

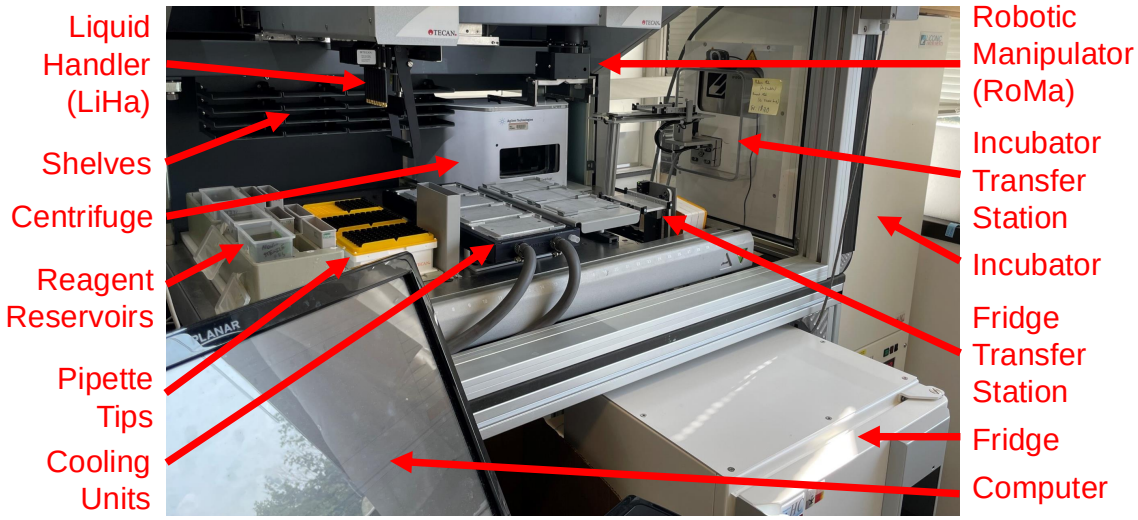

Figure 8: **Overview of IMMUNOtron robotic platform.** Essential components consist of the RoMa (robotic arm), LiHa (liquid handling arm), automated incubator, and automated fridge.

static components, including reagent reservoirs, stacked tip wafers, chilled/room temperature plate holders, and shelves. These components are all assigned specific positions in the Evoware software package used to program the robot, allowing for simple commands to be defined to move plates to or pipette liquids into/out of certain different locations. However, these commands are written using a fairly inflexible visual basic style coding software, so an additional python add-on called the IMMUNOtron interface was written in order to enhance flexibility when interacting with the robot.

2.2.2 Control software: IMMUNOtron-Interface

This IMMUNOtron-Interface control software (https://github.com/soorajachar/immunotron-interface) is a graphical user interface (GUI) written in python that allows for multiple experimental time series to be scheduled and run on the IMMUNOtron simultaneously. After opening the GUI, the user has access to the main menu screen, which contains information about all currently running experiments on the IMMUNOtron as well as empty slots for more experiments to be added. The software currently supports eight experiments at once to be run simultaneously, with each potential experiment being given a slot from A-G. An overview of the package is shown in Figure 9 below.

Upon running the package, the user is confronted with the main experiment status window, shown in Figure 9A. This screen displays the status of all currently running or completed exper-

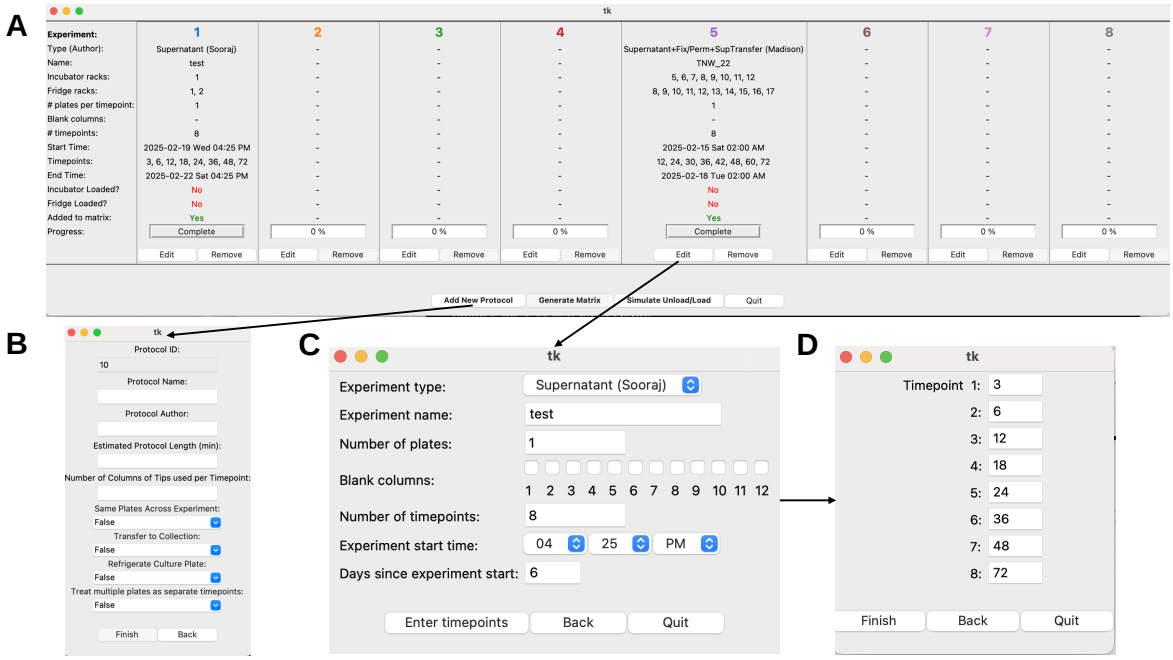

Figure 9: **Overview of IMMUNOtron interface.** This figure displays the essential windows in the IMMUNOtron robotic control interface. (A) is the main window which displays the status of all currently running experiments on the IMMUNOtron. New protocols can be added in the window shown in panel (B). Adding an experiment to the set of currently running experiments can be accomplished in two stages: most experiment specific info is added in panel (C), while the timepoints can be added in the window shown in panel (D).

iments on the IMMUNOtron. Users are able to immediately observe essential information about each experiment (Protocol, name, timepoint number etc.) as well as information about the progress of the experiment through a status bar. In addition, the load/unload status of the fridge and incubator positions associated with experiment are shown towards the bottom of each status column. These labels are controlled by a part of the script that is constantly scanning the status of each experiment's automated fridge/incubator positions; whenever all of the positions are loaded/unloaded, the label flips color and text. In order to generate a matrix, all experiments must have "loaded" positions. To remove an experiment, both the fridge and the incubator must read as "unloaded". These two locks prevent accidental unloading of empty positions or loading of full positions in the incubator/fridge.

To add a new protocol to the program, the user selects the "add new protocol" button, which opens a new window shown in Figure 9B. This window allows the user to control several key

parameters that differentiate protocols from one another.

To add a new experiment to an empty slot on the robot, the user can select the "edit" button located towards the bottom of the status screen, which produces the window shown in panel 9C. This window has several inputs to allow the user to enter all necessary information about the experiment. Critical input information includes the number of plates of samples to be run in the experiment, which columns on the sample plates should be left blank (if any), and the exact experiment start time (in 5 min increments). The final input parameter "Days since experiment start" is used when modifying a previously created experiment's information, and updates automatically as wallclock time passes. After all blanks/dropdowns in this window are filled out, the "enter timepoints" button is enabled, and pressing this button takes the user to the next experiment information window, shown in panel Figure 9D, where they can enter the exact time delays between timepoints for this experiment. Completion of this window takes the user back to the main experiment status screen.

2.3 Analysis pipeline: plateypus

To process the high volume of data generated by experiments utilizing the IMMUNOtron, as well as other high throughput experiments involving many samples spread across multiple plates, we built a software package named plateypus (https://github.com/soorajachar/plateypus) to allow for efficient processing of large plate based experiments. The package is completely controlled through a graphical user interface, and can be split into three sections: setup, labeling, and plotting of experiments.

2.3.1 Experiment setup

Data in plateypus is organized in a multi-tier, hierarchical format. Users must first create a project folder through the interface, and can then use the interface to add experiments to this project. These experiment folders are further broken down into four subfolders: inputData, outputData, misc, and plots. The inputData folder contains the raw data plateypus uses to assemble fully labeled data, which are stored in python dataframes in the outputData folder. The plots folder stores all plateypus created figures as well as plate labeling maps. Finally, the misc folder stores the label and plate layout information used to assemble the final dataframes. These subfolders are

created automatically when a user creates an experiment folder through the interface.

After creating a project then adding an experiment to the project, the user can then export data from Flowjo/Incucyte into the experiment folder in order to start the labeling process. plateypus can currently handle five distinct types of biological data: bulk cytokine data (collected through cytokine bead arrays on flow cytometers), bulk cell protein expression data (collected through flow cytometers), single cell protein expression data, cell killing data (collected with Incucyte systems), and bulk PCR data (not discussed). The export process for each type of data is detailed in the next few subsections.

Bulk cytokine: Processing bulk cytokine data through plateypus involves several steps. First, the raw fcs data must be loaded into Flowjo, gated, then exported as a Flowjo csv for plateypus to read. The raw fcs data will consist of two types of files: calibration wells, and sample wells. The calibration wells are typically acquired in a separate plate to sample wells, and represent the output of a serial dilution of a known concentration of cytokine standards. Sample wells represent actual samples. .

The gating strategy for cytokine bead array kits is fairly straightforward. There are three broad classes of gates required, described in hierarchical order: bead gates, cytokine gates, and barcode gates. The first two gate categories are required, while the third is optional. The "Bead" gate uses the characteristic FSC and SSC of beads to remove debris from the acquisition. The "Cytokine" gate(s) use one or more fluorescence channels (most commonly APC and APC/Cy7) to distinguish different cytokine specific bead populations from one another. Finally, "Barcode" gate(s) use additional fluorescent channels to distinguish samples from different plates that have been mixed together (but had been labeled with different barcoding antibodies first). Barcoding samples in this way allows for much higher throughput acquisition, as the output from anywhere from 2-8 plates can be acquired simultaneously using just 1-3 barcoding antibodies. Once these gates have been applied, the user can compute the geometric mean of the quantification channel (usually PE) for all gated populations, then export those statistics as a csv in Flowjo. plateypus will automatically fit and apply calibration curves to the samples. Figure 10 shows an example of cytokine samples that have been put through this process:

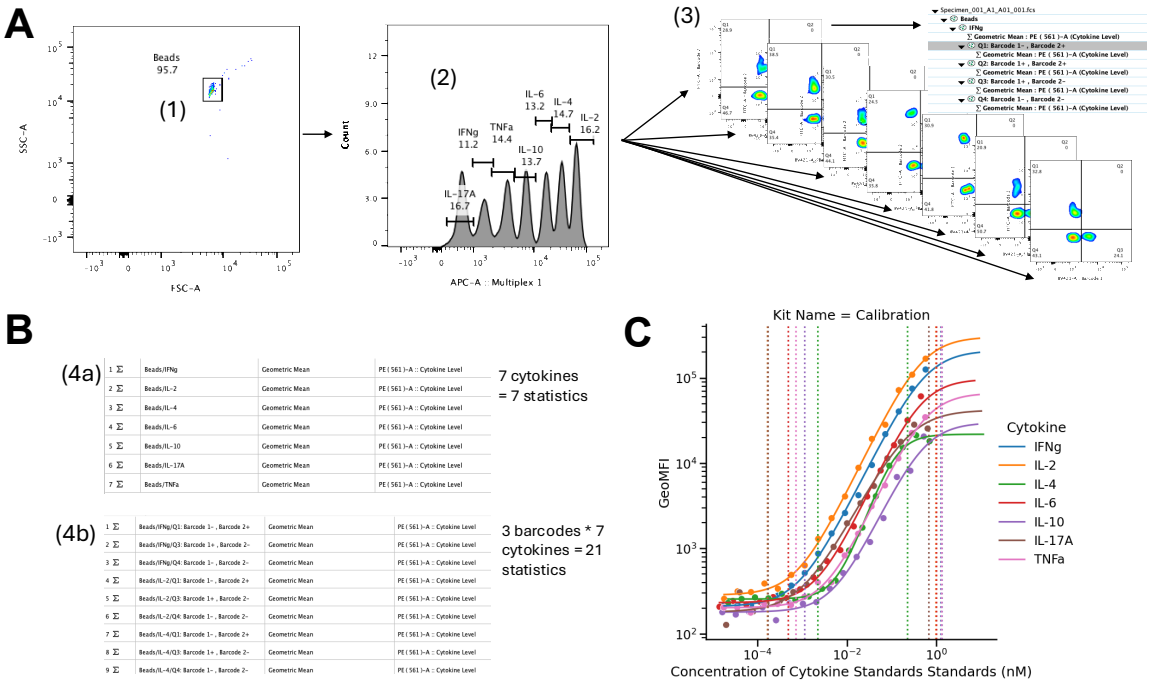

Figure 10: **Overview of cytokine exporting process.** (A) Gating and (B) export procedure for a basic cytokine bead array dataset: (1) gate beads on size (2) gate individual cytokine beads based off of identification channel(s), (3) gate each cytokine's beads for barcoding channel(s) (4) Export all individual gated populations applied to every sample; (4a) Example of populations for set of samples without barcoding, (4b) Example of populations for set of samples with barcoding (C) Example of calibration curves automatically fit to calibration samples by plateypus before being applied to data. Dotted lines correspond plateypus calculated lower and higher limits of detection for each cytokine's calibration curve.

Bulk cell protein: Processing bulk cell data through plateypus follows a similar procedure to processing bulk cytokine data. After compensating the samples, any gates of interest are first applied onto each individual sample, then any bulk statistics of interest are applied onto the gated populations. All gate+statistic combinations are then dragged into the table editor menu and exported as a csv. Just as before, all samples must have the same set of gates and statistics. Barcodes can be applied in the same way as in the cytokine exporting process.

Single cell protein: To process single cell flow cytometry data, plateypus needs to read the individual cell values from fcs files after logicle scaling. To do this, the user must export "channel" csv files from Flowjo for each fcs file. These files can be exported after doing initial cleanup gating by selecting a gate in a group for export. Each group needs to be exported one by one into the correct

folder that plateypus pre-prepares for the user after they create a plate layout file. Individual gate populations (for different cell types for example) need to each be dragged into each plate/group and exported one by one into the relevant single cell csv folder made by plateypus. Barcoded single cell samples have a slightly trickier exporting phase. The relevant barcoding gates must be dragged onto all samples plate by plate. The user can then click on each one of the barcoding gate populations in turn by plate/group and again export them to the correct single cell csv folder made by plateypus. If these barcoded samples also have individual cell populations, these cell populations must be distinguished from the barcode gates by adding in a double underscore before the cell population name as the suffix of the population during the exporting process. This process is summarized in Figure 11 below.

Cell Killing: To export cell killing data from the output of an incucyte machine, a user must navigate to the "view" tab of the incucyte console, change the analysis definition by going to the "graph analysis metric" tab, select the "green object count" statistic, highlight all wells on a plate, then export the data, making sure to sort by column, onto the clipboard. The data can then be pasted into an excel file and saved as a "plate name + _killing" csv. This process is summarized in Figure 12 below.

Once bulk cytokine, cell, or killing statistics have been moved into the table editor in flowjo, the tables can be exported as csvs for plateypus to read. The naming format of these csvs is critical in order for plateypus to read the correct files and associate them with the correct labels. All cytokine csvs will end in the suffix "_cyt" in order to signal to plateypus that the samples in that particular csv are from a cytokine plate, while bulk cell csvs will end in the suffix "_cell" and killing csvs will end in the suffix "_killing". Calibration samples csvs will always be named "Calibration_cyt.csv". Bulk sample plates are named with the letter "A", then their plate number (as defined in the plate layout editor from the previous step), There are two important exceptions to this rule.

The first occurs when samples whose cocultures were plated in a 96 well plate are moved into a 384 well plate for acquisition (when the box "96->384 well acquisition" is ticked in window X. These are labeled differently; each 384 well plate that is acquired gets named AX-X+4, where X and X+4 represent the starting and ending number of the 96 well plates the samples were originally

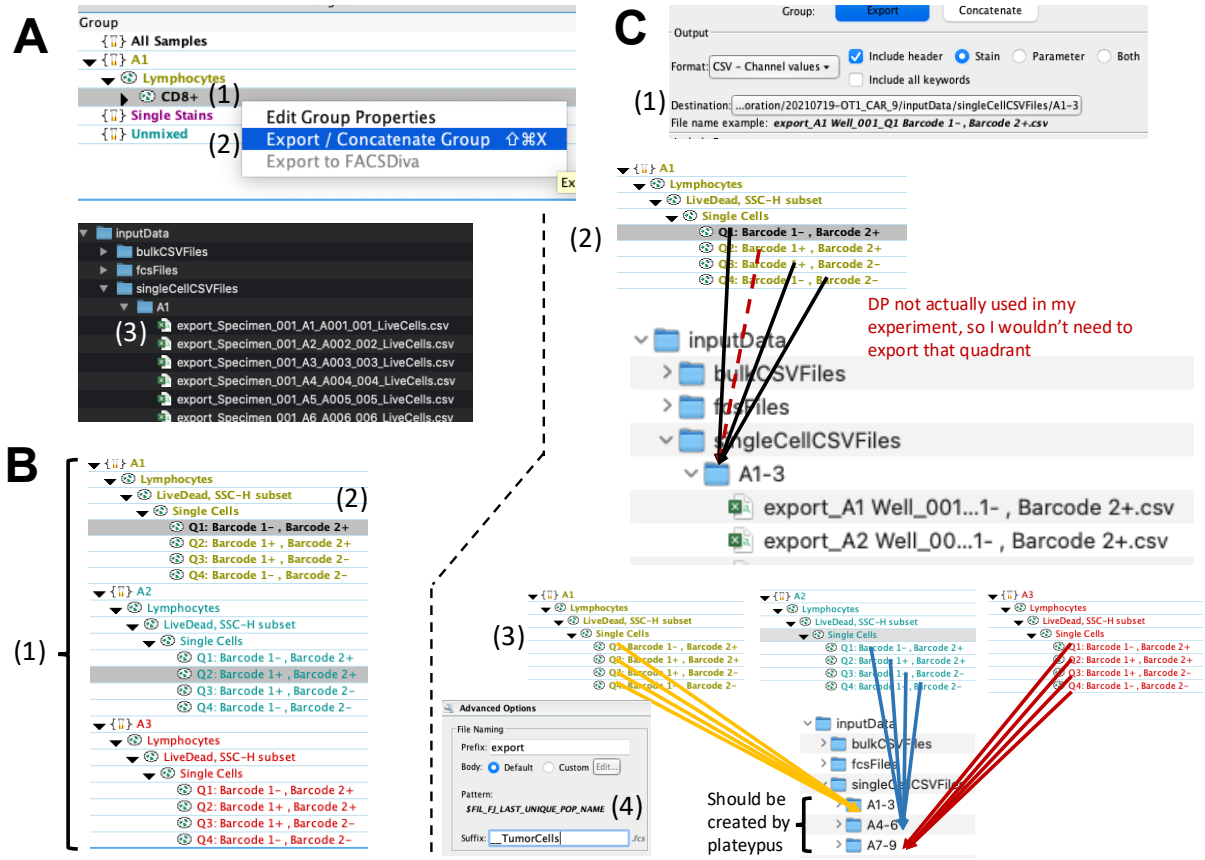

Figure 11: **Overview of single cell exporting process.** (A) The parent gate of the population of interest (1) needs to be applied to all samples in a plate, then exported (2). (B) With barcoded cell samples, the barcoding gates need to be the child gates of the population of interest and applied to each plate individually, in order to ensure the suffix of these files consists of the barcoding sequence (1), then are individually exported (per combination of plate + barcode) (2) as before. (C) In either case, the channel values of all relevant fluorescent parameters (1) need to be exported into the corresponding folder automatically created by plateypus in the singleCellCSVFolder (2). In the case of barcoded samples, all barcoded samples go into the same plate folder (3). If multiple populations from a barcoded samples need to be exported, the population name must be added in manually as a suffix with a double underscore in front (4) in order to be identified and concatenated together correctly

plated in. For example, if an experiment consisting of 8 96 well plates was moved into two 384 well plates for faster acqusition, the names of these two 384 well plates would be A1-4 (Plates 1-4 of the original samples) and A5-8 (Plates 5-8 of the original samples). This naming convention signals to plateypus to split these aggregate csvs into their original 96 well formats in order to assign labels to them correctly.

The second occurs when samples are barcoded together before acqusition. The same principles

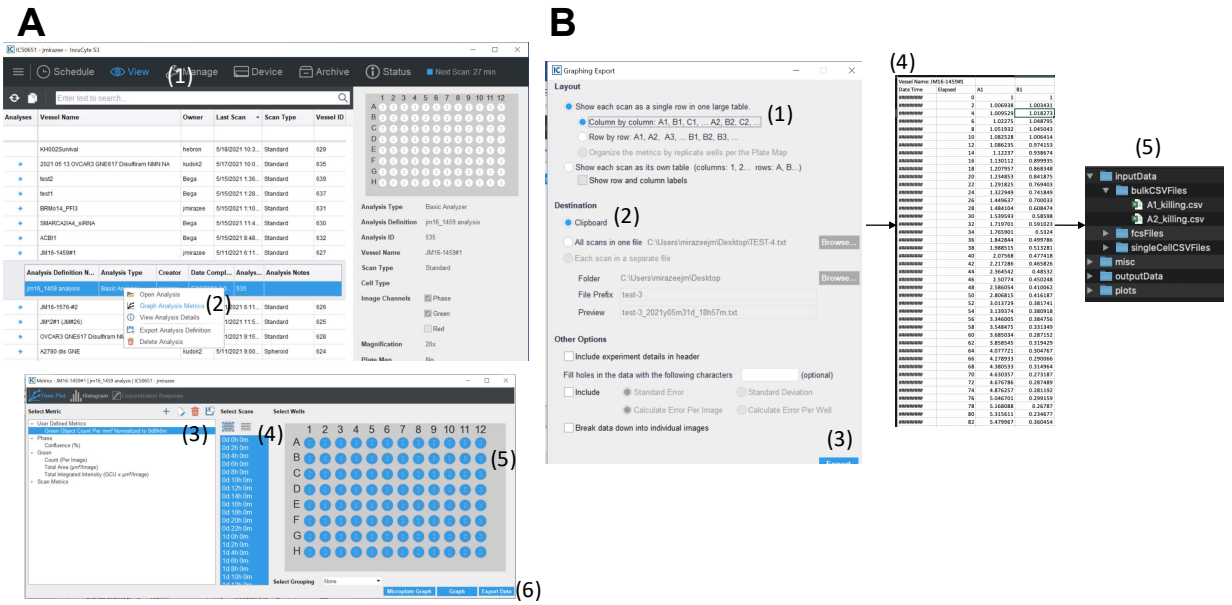

Figure 12: **Overview of killing data exporting process.** (A) Incucyte display screens and (B) Export screens required to generate (C) CSV that is exported into the (D) correct folder in plateypus, with a underscore+"killing" suffix attached

apply; for example if a 8 96 well plate experiment was labeled with 2 different barcodes, and each set of 2 barcodes was mixed together and acquired (resulting in 4 96 well plates), the barcoded plates would be labeled "A1-2_...", "A3-4_..." etc.

If both barcoding and 96->384 well acquisition are used, the changes in naming convention stack on top of one another, with barcoding taking precedence (due to the logistics of sample preparation). For example in the aforementioned 8 96 well plate experiment, if the plates are moved into two 384 well plates, then those two plates are barcoded differently and mixed together, the single resulting plate would be named "A1-8_...". Because both high throughput options are checked for this experiment, plateypus would know to split the single plate into two 384 well plates based on barcode first, then split each of these 384 well plates into 4 96 well plates using 96->384 demultiplexing.

2.3.2 Plate labeling

Labeling plate positions in plateypus consists of two distinct phases: Creating labels for all samples and assigning these labels to each sample in the experiment in a plate based GUI. The interface workflow for label creation is shown in Figure 13 below.

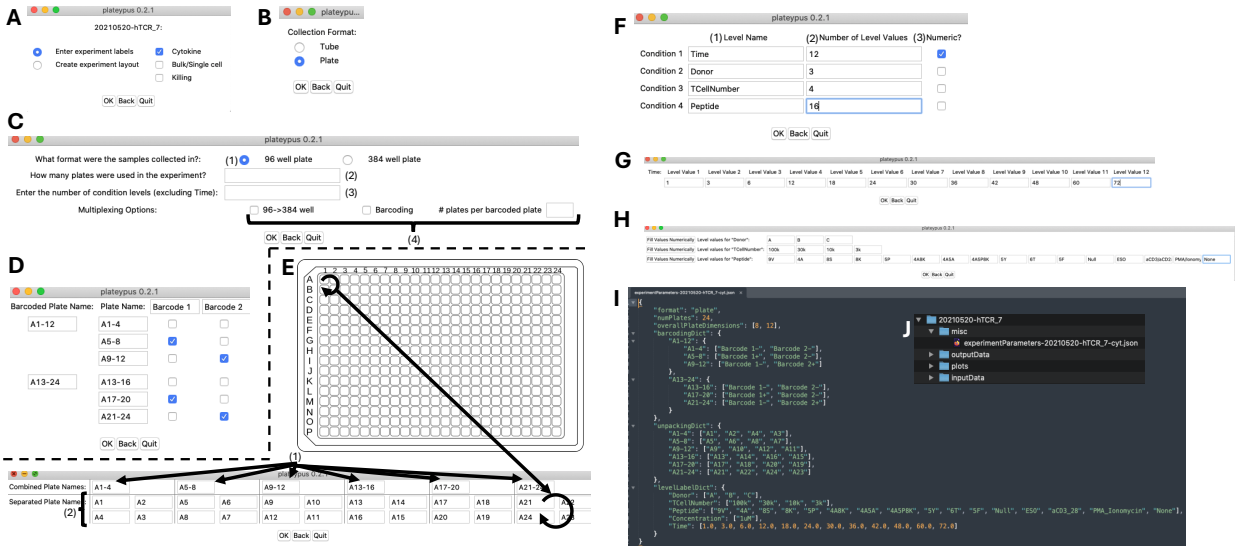

Figure 13: **Overview of plateypus labeling layout workflow.** Options required to be selected in (A) first and (B) second plateypus windows in order to access (C) main plate labeling layout screen. (A user can select the plate type their samples were plated on and the number of those plates used in the experiment in (1) and (2) respectively. (3) refers to the number of types of experimental groupings there are (Donor, T cell number etc.). (4) refers to methods of expanding how many samples can be processed at once by the program. If barcoded samples were used, the " plates per barcoded plate" entry needs to be filled before selecting the "Barcoding" option presents the user with the screen in (D), where the correct sequence of barcodes and the plate types they're referring to can be clearly delineated. Selecting the "96-¿384" option presents the user with the window in (E) bottom, where the correct splitting procedure to turn 384 well plates into a certain number of constituent 96 well plates can be delineated. (F) shows the next window, where a user can enter the names of the "Levels" (groups) in (1), then the number of individual labels within that group in (2). Only the "Time" entry needs to have the numeric label checked, and the values of the "Time" group/level can be entered in (G). All other group's constitutent level values can be entered in the following window in (H). Note the "Fill values numerically" button that allows for simple numeric iteration across all entries in that row; useful for a "Replicate" level. The information entered by the user during this process is shown exported into a human-readable/editable JSON that plateypus can read later on, an example of which is shown in (I), with its file location shown in (J)

After label creation, the user can navigate to the plate label assigning window and start assigning labels to wells in their experiment. The two screens that make up this part of the interface are described in Figure 14 below.

Usage of the repeating/tiling buttons in particular are described in greater detail in Figure 15 below.

By using a combination of these repeating and tiling actions, users can quickly assign complex patterns of plate labels to large experiments, such as those generated by the IMMUNOtron. An

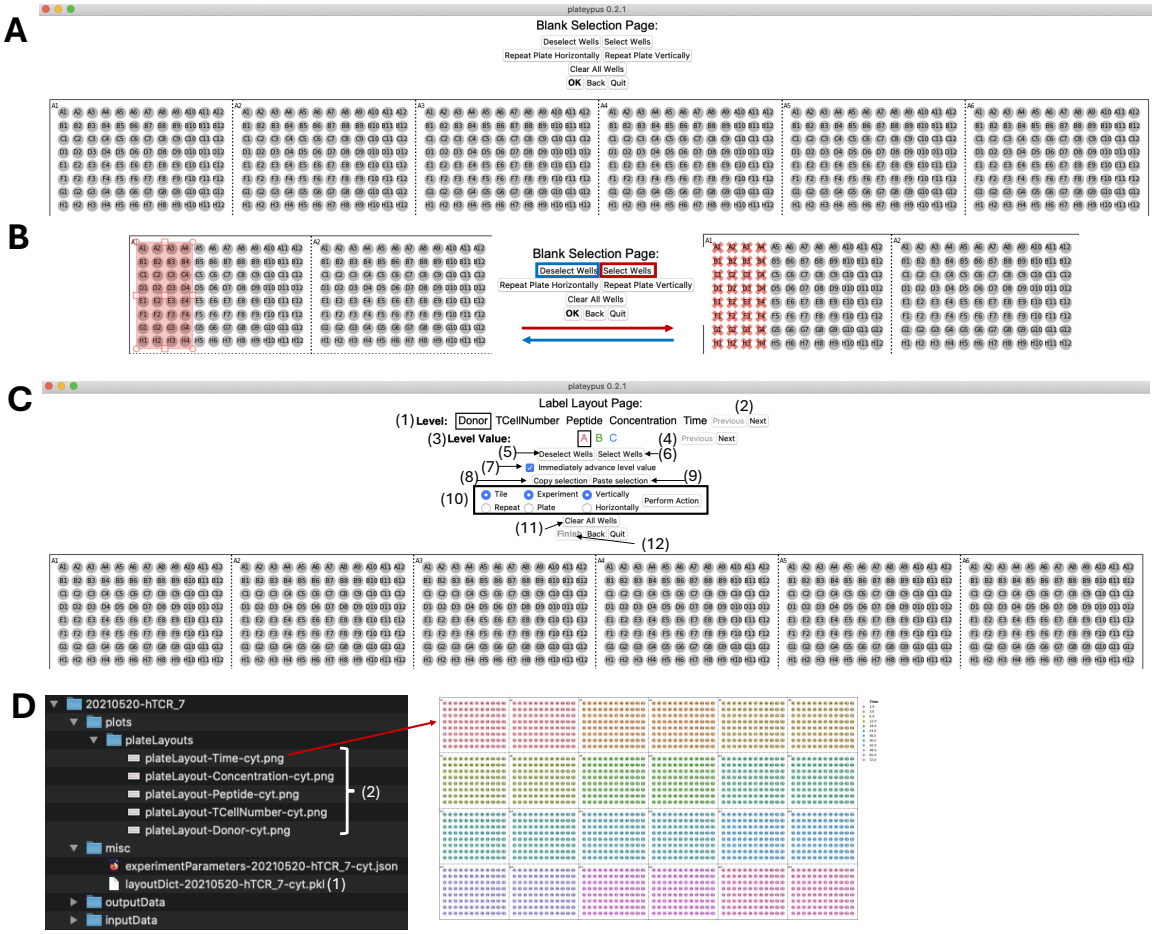

Figure 14: **Overview of plateypus plate layout workflow.** (A) Initial plate layout editor window, where (B) wells can be marked as "blanks" to avoid having to assign them labels. (C) Second plate layout editor window, where labels can be assigned to each well in the experiment. (1) displays the level that labels are being assigned from, with the buttons in (2) used to move between levels. (3) displays the level values that are being assigned, with the buttons in (4) used to move between level values. The buttons in (5) and (6) are used to mark or unmark a region of the experiment with a certain level value. The option in (7) automatically advances level value upon a press of (5) without having to manually press the next button in (4). (8) and (9) are used to copy/paste level value patterns between different parts of the experiment layout. The options in (10) are used to rapidly transfer label patterns to different parts of the experiment layout, and are described further in Figure 15. (11) is used to remove all level values at the current level, and (12) is used to finish the label assignment procedure (only is enabled on the final level's label assignment page).

example illustrating how chaining together sequences of plate actions can quickly label a large experiment is shown in Figure 16 below.

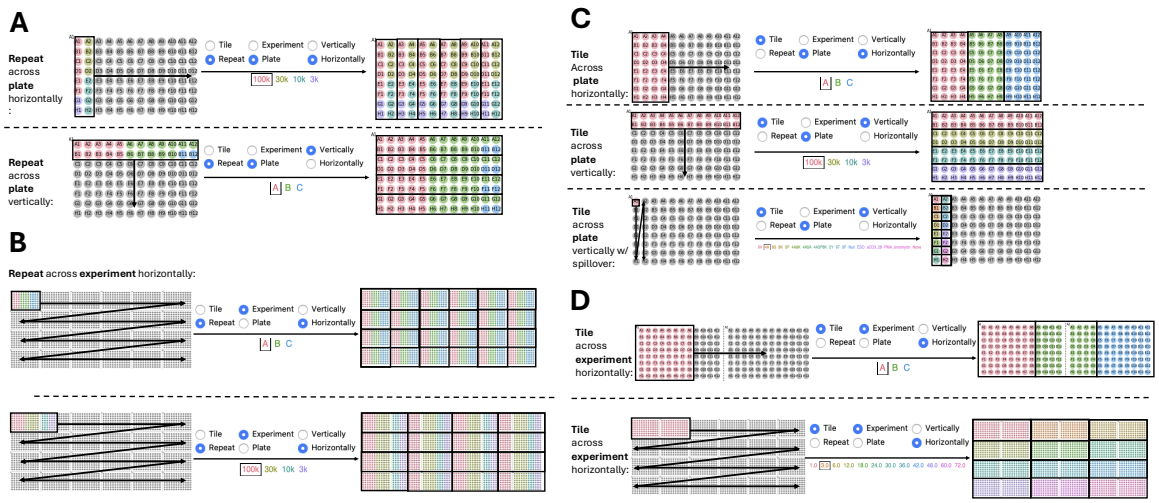

Figure 15: **Overview of plateypus plate layout actions.** This figure displays the essential plate layout actions in plateypus: repeating a sampling labeling pattern across a plate (A) or across an experiment (B), or tiling a sampling labeling pattern across a plate (C) or experiment (D)

	1D		Categorical (1.5D)						2D		3D
	Histogram	KDE	Bar	Violin	Box	Point	Swarm	Strip	Line	Scatter	Heatmap
Color	X	X	X	X	X	X	X	X	X	X	
Marker									X	X	
Size									X	X	
Order			X	X	X	X	X	X	X	X	
X axis									X	X	X
Y axis											X
Row	X	X	X	X	X	X	X	X	X	X	X
Column	X	X	X	X	X	X	X	X	X	X	X
None	X	X	X	X	X	X	X	X	X	X	

Table 1: **Overview of available plateypus graphical components by plot type.**

2.3.3 Data plotting

After creating processed dataframes, plateypus can be used to create simple plots in a wide variety of formats: bar/line graphs, heatmaps etc. While these plots are by no means publication quality, they do represent a quick way for users to graph their very high throughput data for basic analysis/quality control. The basic principle behind plateypus' approach to high throughput plotting is to break every type of graph down into a series of graphical components that can be assigned to any group of conditions in a dataframe.

The graphical components each plot type is broken down into is shown in Table 1:

Any condition groups not assigned to graphical components are then used to make separate

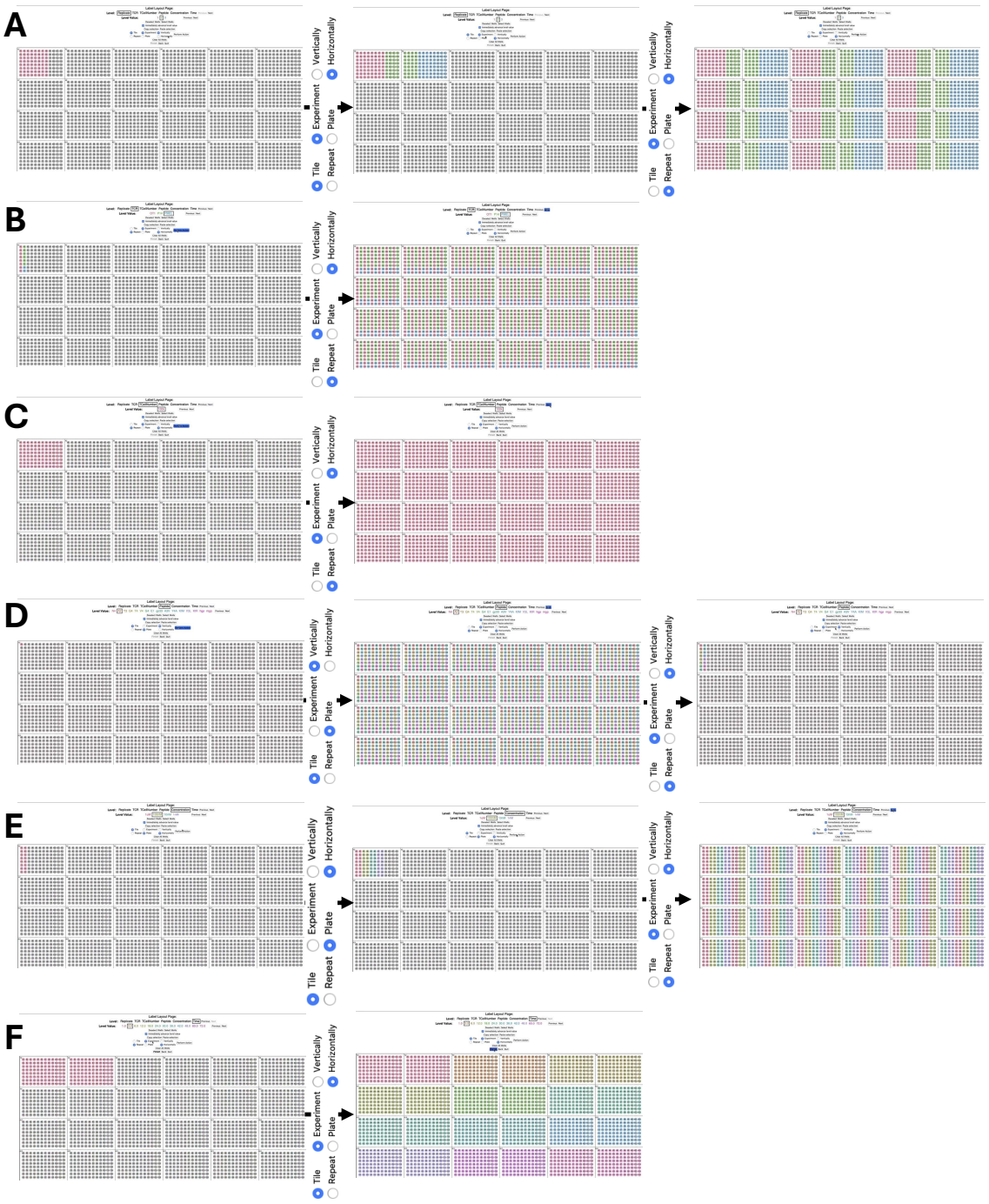

Figure 16: **Example of full plate layout action chain.**

plots. Individual conditions within a group can be selected or deselected for inclusion in the figure. Figure 17 below shows an example of this process:

This approach leads to rapid plotting of all data within a complex dataset, allowing users to quickly gain a sense of which aspects of their entire dataset are interesting enough to follow up on

with further analysis.

After developing the high throughput IMMUNOtron robotic analysis platform, control software, and data processing pipeline detailed in this chapter, we had sufficient data collection and analysis capabilities at our disposal to move on to the main topic of my thesis: understanding the rules governing dual ligand stimulation in CAR T cells.

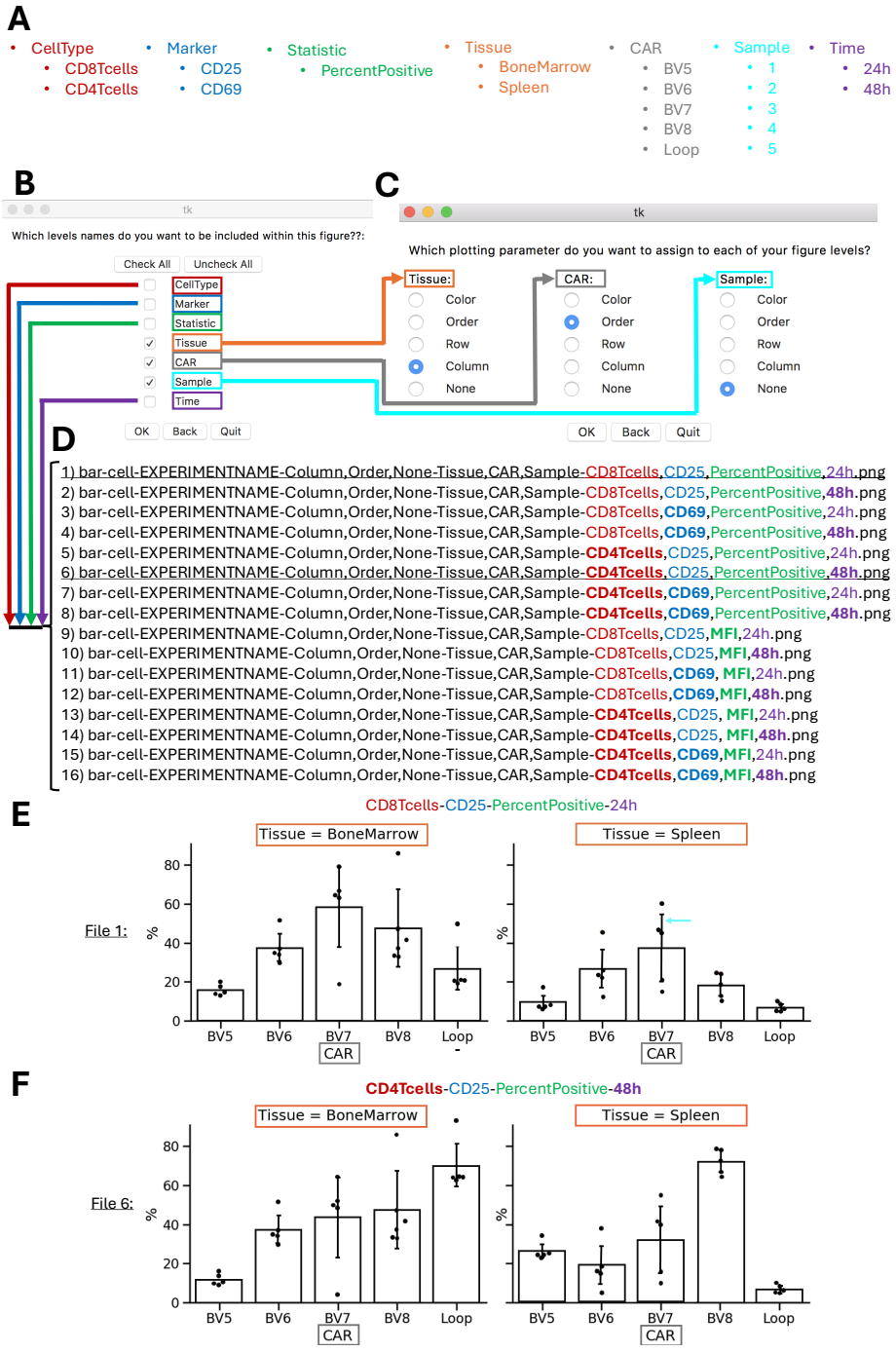

Figure 17: **Overview of plateypus plot multiplexing procedure.** (A) Sequence of levels and level values present in example dataset to be plotted (B) Level inclusion window. Levels that are selected can be assigned to plotting parameters, all other levels will be iterated through unique combination by unique combination and used to make separate plots. (C) Plotting parameter assignment window. The options presented here differ by plot type. None option is used for "Replicate" levels (D) Sequence of unique file names generated by plateypus using the level values in the levels left unselected in (B). (E and F) Two different final plot examples from list of files in (D); the type of plot stays the same between files, only the subset of data displayed differs.

3 How do different receptors in T cells interact with one another when stimulated with antigens of different densities and strengths?

3.1 Introduction

In order to build a comprehensive and generalizable model of T cell signal transduction during dual antigen stimulation, we opted for a two stage approach. We first collected data for the simpler, homogeneous receptor stimulation case, where monoclonal T cells expressing a single TCR were stimulated by antigen presenting cells pulsed with combinations of two antigens of different affinities and densities, and then attempted to develop and fit the parameters of a model of T cell activation that could explain the outputs we observed. We would subsequently fix these TCR-associated parameters in the model before moving onto collecting data for the more complex heterogeneous receptor case where a T cell expressing both a CAR and TCR is stimulated through both ligands simultaneously. Only parameters related to the activation of the CAR would be fit in this second round of model development, allowing for the generation of a robust, generic model of T cell activation during dual ligand stimulation that could be used for further predictions in more therapeutically relevant scenarios, including *in vivo* measurements.

3.2 Methods

Calibration of receptor and ligand abundances: Cells to be analyzed were washed once in FACS buffer and then stained for the molecule of interest coupled to either a FITC or PE dye at a 1:25 dilution at 4^oC for 20 min. Samples were run on a flow cytometer alongside FITC or PE quantification beads from Bangs Laboratory. The geometric mean fluorescence of the beads was then used to construct a calibration curve to relate the fluorescence of the samples to molecule numbers. To measure the MHC loading efficiency of peptide pulsing, TAP-deficient RMA-S cells were pulsed with SIINFEKL peptides of varied TCR affinities across different peptide concentrations at 37^oC overnight. Cells were then washed once before staining using an anti-H-2Kb antibody (1:600 dilution).

Generation of murine TCR/CAR T cells: Murine CD8+ T-cells were isolated from spleens of male or female OT-1 mice, OT-1 6Y/6Y mice, and OT-1 6F/6F mice using the EasySep Mouse CD8+ T-cell Isolation Kit (STEMCELL Technologies) and murine CD4+ T-cells were isolated from spleens of male or female SMARTA mice using the EasySep Mouse CD4+ T-cell Isolation Kit (STEMCELL Technologies) following the manufacturer's protocol. The isolated CD4+ or CD8+ T-cells were stimulated using immobilized anti-mouse CD3ϵ (5 µg mL^{-1}; clone: 145-2C11; #553057) and anti-mouse CD28 (2 µg mL^{-1}; clone: 37.51; #553294) monoclonal antibodies (BD Biosciences) with human IL-2 (Proleukin; Clingen; 120 IU mL^{-1}) in complete RPMI 1640 medium. Eighteen to twenty-four hours after T-cell stimulation, activated T-cells were transduced with viral supernatants harboring Thy1.1, 1 ITAM mCD19 CAR, or 3 ITAM mCD19 CAR retrovirus. Transductions were performed twice at 24 h intervals on retronectin-coated plates following the manufacturer's protocol (Takara Bio) in the presence of immobilized anti-mouse CD3ϵ (2 µg mL^{-1}) anti-mouse CD28 (2 µg mL^{-1}). Viral supernatants and T-cell stimulation antibodies were removed on day 3, and replaced with a complete medium containing IL-2. Transduction efficiencies were evaluated on day 6 by flow cytometry. Dead cells were removed from cultures using lympholyte-M (Cedar Lane Laboratories) and transduced T-cells were used for *in vitro* and *in vivo* analyses on day 7.

***in vitro* TCR/TCR activation measurements:** T-cell and antigen-presenting cell cocultures were prepared as follows. Spleens from C57BL/6N (B6) mice were crushed through an 80 µm filter to form a single-cell suspension of B6 antigen-presenting cells (APCs) in a complete RPMI medium. Cells were spun down at 500g for 5 min, then the supernatant was aspirated and resuspended in 1 ml of ACK lysis buffer at room temperature to remove red blood cells. The lysing reaction was quenched through the addition of 14 ml of complete RPMI medium. Cells were then spun down at 500g for 5 min and washed with complete RPMI medium twice before being resuspended at a concentration of 3M cells/ml. Agonist peptides were diluted to concentrations of interest and plated onto 96 well v-bottom plates in 100 µl aliquots, and the previously prepared APC cell suspension was then added to all wells in 100 µl aliquots. The agonist peptides and APCs were incubated together for 1.5 h at 37^{o}C and were subsequently washed with 200 µl of complete RPMI medium before being resuspended in 200 µl of antagonist peptide at the appropriate concentrations. After

an additional 1.5 h incubation of antagonist peptides and agonist-bearing APCs, the plates were washed twice with 200 µl of complete RPMI medium before being resuspended in an additional 100 µl of complete RPMI medium. The single-cell suspension preparation protocol outlined above was repeated for T-cells derived from the spleens of OT-1 mice, which were then diluted to a concentration of 1M cells/ml before being added to all wells of the pulsed APC plates in 100 µl aliquots to produce cocultures with total volumes of 200 µl. Plates were then spun down at 500g for 10 s to form contacts, and incubated at 37^{o}C. Manual, instead of robotic, time points were taken for this set of time series to maximize dynamic range. Briefly, at each time point during a TCR/TCR antagonism time series (typically at +3, +6, +12, +24, +48, and +72 h) 100 µl of the supernatant of a coculture (a different replicate coculture for each time point of the same condition) was collected and moved into a separate collection plate stored at -20^{o}C. Supernatants were then thawed and analyzed with a BD Cytokine Bead Array (CBA) kit on a flow cytometer.

***in vitro* TCR/CAR activation measurements:** TCR, CAR, or TCR/CAR T-cells (5×10^4 cells) were co-cultured with the indicated peptide-pulsed tumor cell lines in 200 µl of complete RPMI medium in V-bottom 96 well plates at a 1:1 E: T ratio. The IMMUNOtron robotic platform was programmed to perform automatic collection and replenishment of supernatants at given time points (typically, 1, 3, 6, 12, 18, 24, 30, 36, 42, 48, 60, 72 h post-initiation). Briefly, cell culture plates and medium plates were retrieved from the incubator, 10 µl of culture supernatants were collected with minimal disruption of cell pellet, and wells were replenished with 10 µl of fresh medium in order to keep the overall well volume constant throughout the experiment. Collected supernatants were stored at -20^{o}C until analysis with a BD Cytokine Bead Array (CBA) kit on a flow cytometer.

Cytokine bead array: Mouse/human Th1/Th2/Th17 or Flex cytokine kits (Table S7) from BD Biosciences were used to quantify 7 or 26 cytokines in each collected supernatant sample. Collected supernatants were thawed at room temperature, loaded with CBA reagents (beads and detection reagents), and incubated at 4^{o}C for 1 h. When running multiple cytokine plates by flow cytometry, plates were barcoded using fluorescently labeled Fab fragments. Typically, the FITC-

labeled anti-rat Fab fragment (Jackson ImmunoResearch) was added to a final concentration of 2 µg ml-1 and incubated for 15 min at room temperature. This reaction was then quenched by adding an excess of Rat IgG (Jackson ImmunoResearch) to a final concentration of 30 µg ml^{-1} and incubated for 15 min at room temperature. Fab-labeled CBA plates were then consolidated into one plate, spun down at 1,000g for 2 min, flipped to discard supernatants, vortexed, and resuspended in 100 µl of PBS containing 4% FBS for acquisition on a 5-laser/18-channel flow cytometer (FACS Fortessa, BD Biosciences).

***in vivo* mouse model of CAR T-induced cytotoxicity:** Eight- to twelve-week-old female Rag1−/− or CD45.1 C57BL/6 (B6) mice were used as recipients for *in vivo* adoptive transfer experiments. For the mouse leukemia model, E2aPBX or ovalbumin peptide-expressing E2aPBX leukemia cells (2 × 104) were injected intravenously into Rag1−/− mice. Three days later, 1 × 106 empty (Thy1.1) vector-transduced (OT-1) or mCD19 CAR-transduced (OT-1/CAR) T-cells were intravenously transferred into the mice. *in vivo* anti-leukemic activity of OT-1 and OT-1/CAR T-cells was assessed as a function of the survival time of E2aPBX-bearing Rag1−/− mice. For the mouse melanoma model, CD19+ B16 cells or ovalbumin peptide-expressing CD19+ B16 cells (5×10^5) were intradermally inoculated into the right flank of CD45.1 B6 mice. Nine days after B16 cell inoculation, mice were sublethally irradiated (600 cGy) and were treated 24 h later by adoptive transfer of either OT-1 or OT-1/CAR T-cells (1×10^6). Tumor sizes were measured every 2-3 days in a double-blind manner using a digital caliper and mice were euthanized at humane endpoints if tumor sizes surpassed 400 mm^2. Survival time was evaluated as duration until death or euthanization. For tumor-specific killing assay experiments, CD19+ B16 cells expressing mKate2-tagged low affinity (V4) ovalbumin peptide and mLNGFR-tagged CD19+ B16 cells (2.5×10^5 each) were co-injected intradermally into the right flank of CD45.1 B6 mice followed by sublethal irradiation. All tumor-bearing mice were randomized before T-cell transfer (1×10^6). Tumor size and survival measurements were conducted in a double-blind manner. All animal studies were conducted using Institutional Animal Care and Use Committee (IACUC)-approved research protocols.

Evaluation of tumor-infiltrating lymphocytes (TIL) and tumor cell isolations: For TIL analyses, harvested B16 tumor tissues were weighed and dissociated by gentleMACS (Miltenyi Biotec) following the manufacturer's protocol. The TIL population was purified by density gradient centrifugation. For analysis of specific tumor killing, harvested B16 tumor tissues were minced using scissors, dissociated by collagenase/hyaluronidase (STEMCELL Technologies) at 37^{o}C for 25 min, and processed with a plunger to prepare single-cell suspensions.

Flow cytometry: Cells were spun down in 96 well plates at 500g for 1 min and washed once with PBS (200 µl), then stained with Live/Dead dye (50 µl, ThermoFisher) per the manufacturer's instructions for 5 min at 37^{o}C. Staining was quenched by the addition of PBS containing 4Plates were then spun down and washed once with FACS buffer before being resuspended in FACS staining buffer (2antibodies of interest (50 µl) at the indicated dilutions. Cells were incubated with antibodies for 20 min at 4^{o}C, and staining was quenched by the addition of FACS buffer (150 µl). Cells were subsequently resuspended in FACS buffer (100 µl) and acquired at a rate of 1.5 µl/s on the BD LSRII Fortessa or medium speed on the Cytek Aurora 5L (Cytek Biosciences). BD UltraComp beads were used to prepare single stain controls to compensate (conventional flow cytometry) or unmix (spectral flow cytometry) samples after acquisition. All antibodies used in conventional flow cytometry and spectral flow cytometry are listed in Tables T1 and T2 below.

3.3 TCR/TCR interactions

3.3.1 Full Perturbation Matrix

Our general strategy to gain a comprehensive understanding of how interactions between differentially stimulated T cell receptors affected overall activation is shown in Figure 18 below.

As seen in Figure 18A, we chose to perturb parameters in our dual ligand stimulations along four different axes simultaneously: ligand 1 (agonist) affinity/density and ligand 2 (antagonist) affinity/density. Collecting this dataset would give us a complete map of how T cells responded to dual ligand stimulations, which in turn would allow a model fit on the data to be more robust than previous efforts at modeling dual ligand stimulation in T cells, such as [44], which attempted to fit data derived from dual ligand stimulations varied along 2-3 of these axes. Figure 18B shows the

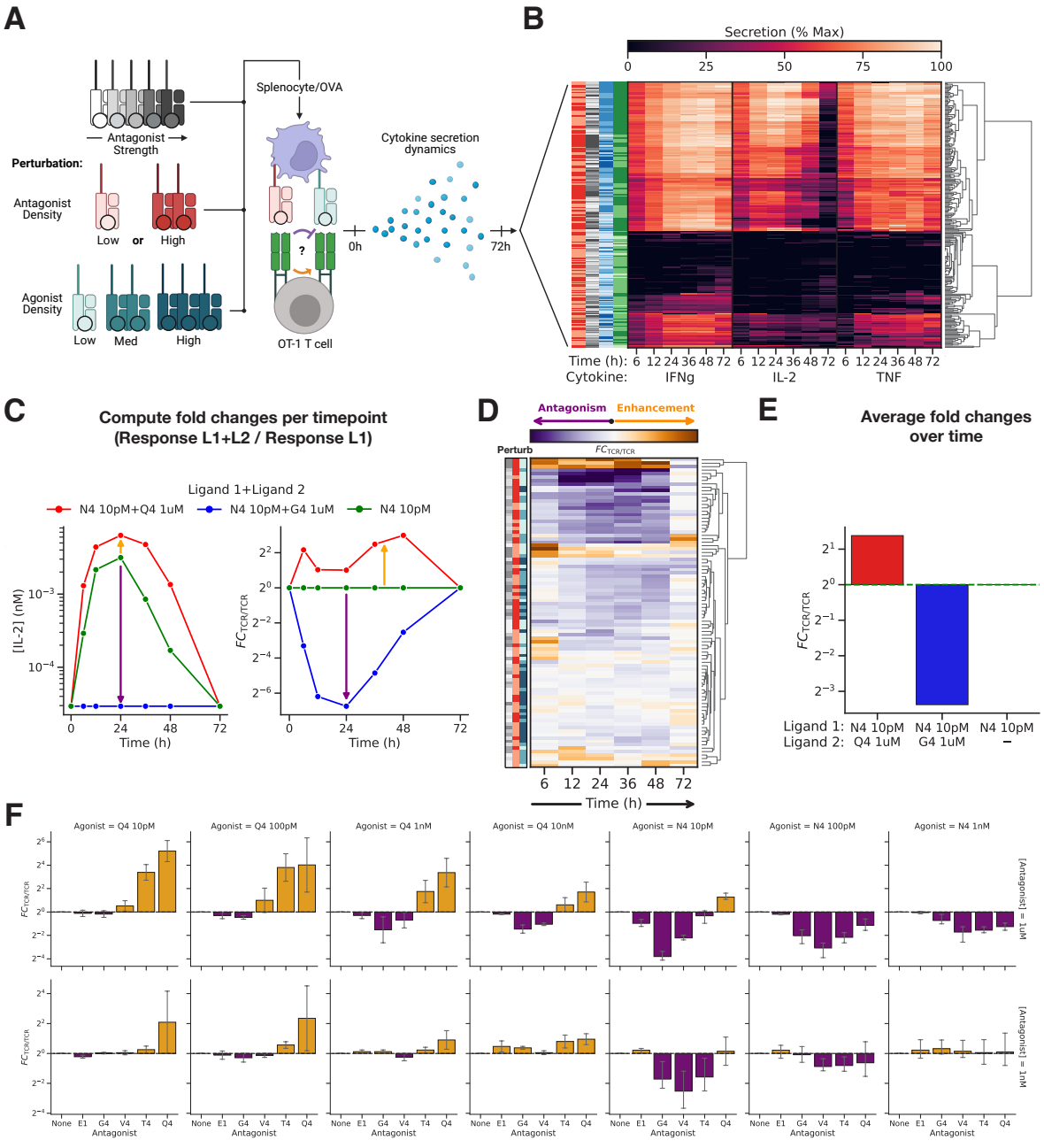

Figure 18: **TCR/TCR interaction ratio calculation procedure.** (A) Multiplexed experimental settings to quantify TCR/TCR crosstalk. (B) Full raw TCR/CAR perturbation matrix (4320 datapoints). (C) Example of conversion of raw TCR/TCR cytokine kinetics (left) into TCR/TCR fold changes (right) (D) Full TCR/TCR FC matrix per timepoint (E) Conversion of per timepoint TCR/TCR fold changes into time averaged fold changes (F) All TCR/TCR FC values averaged over time.

full cytokine production kinetics data for OT-1/CAR T cells stimulated with combinations of two TCR ligands with varied densities and affinities at different timepoints. Figure 18C shows how these

raw datapoints were then used to calculate fold changes for each perturbation in order to quantify the type and extent of TCR/TCR interaction at a given combination of timepoint+perturbation. These interaction ratios were calculated by dividing the amount of output (in this case the average amount of IL-2 produced over time) of the two ligands combined by the output of the agonist ligand alone. Ratios below the dashed line indicate the addition of the second ligand decreased, or antagonized, the T cell activation, while ratios above one indicate an increase, or enhancement, of T cell activation. The results of applying this procedure to all raw data is shown in Figure 18D. These fold changes were then averaged across time, as shown in Figure 18E, to produce summary statistics that described the overall level of antagonism (FC TCR/TCR < 1) or enhancement (FC TCR/TCR > 1) per perturbation. This summary data displays a broad range of antagonistic and enhancing outputs depending on the exact ligands combined in dual TCR stimulation, displaying the complexity of the overall phenomena. The effect of variation along each individual dimension is discussed in detail in the following sections.

3.3.2 Antagonist affinity modulated

Variation along the antagonist affinity dimension can have subtly different effects depending on the agonist used, but the general pattern in cases where antagonism is observed is quite similar, as can be seen in Figure 19 below.

Generally, when antagonism is observed at a given combination of agonist density/affinity, the overall pattern of TCR/CAR crosstalk varies non-monotonically as a function of antagonist affinity. Very weak ligands often do not affect T cell activation with the agonist at all, and very strong ligands only cause enhancement of activation. Ligands with intermediate affinities can cause either enhancement or antagonism, with the general progression being a transition from antagonism to enhancement as affinity increases.

3.3.3 Agonist affinity modulated

Decreasing agonist affinity (Figure 20 below) seems to generally decrease the magnitude of antagonism observed, as well as the range of ligand qualities eliciting antagonism.

This makes intuitive sense, as a lower affinity agonist will have a strength more similar to its

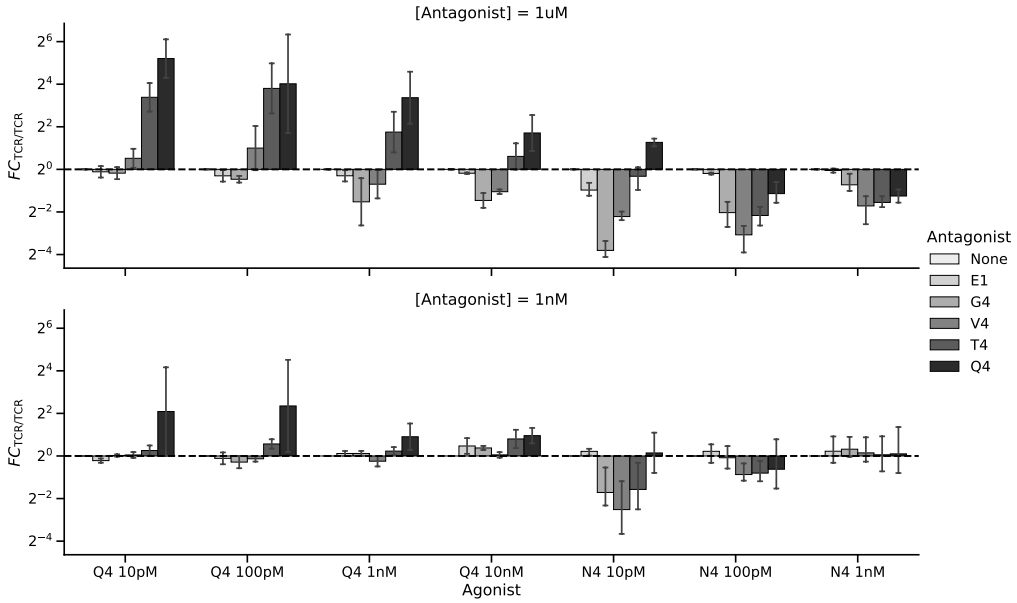

Figure 19: **TCR/TCR crosstalk as a function of antagonist affinity**. Fold change of OT-1 T cell IL-2 production in response to B6 splenocytes presenting agonist ligand alone vs agonist+antagonist ligands, plotted to emphasize changes based on antagonist affinity. Data is plotted from three independent experiments. Dataset also used in Figures 20,21,22.

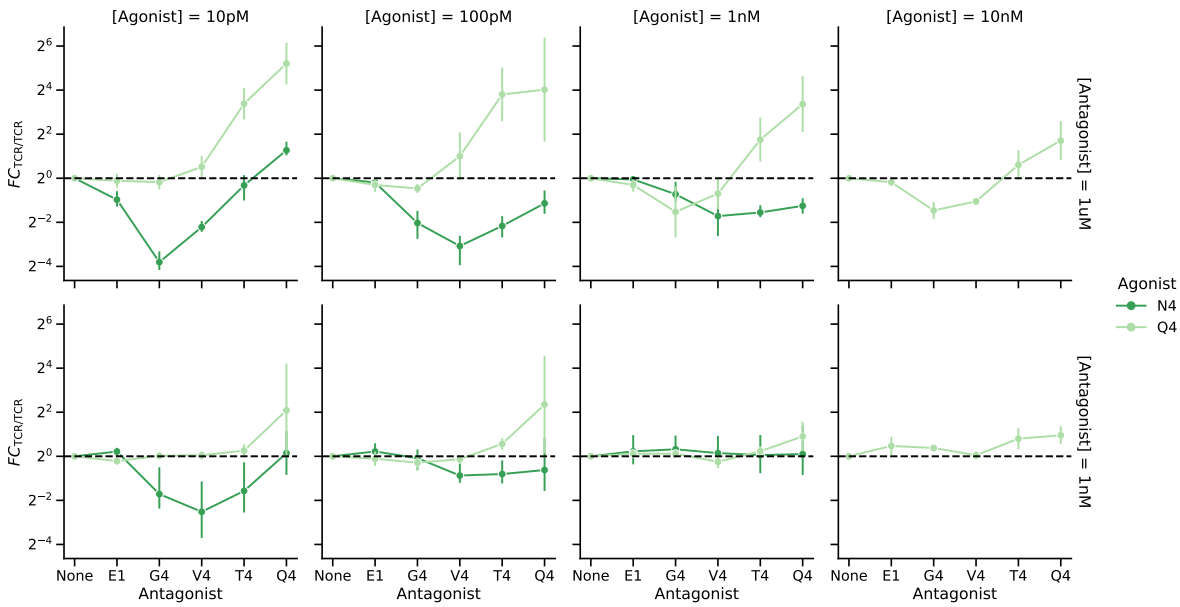

Figure 20: **TCR/TCR crosstalk as a function of agonist affinity**. Fold change of OT-1 T cell IL-2 production in response to B6 splenocytes presenting agonist ligand alone vs agonist+antagonist ligands, plotted to emphasize changes based on agonist affinity. Data is plotted from three independent experiments. Dataset also used in Figures 19,21,22.

antagonists, which would decrease the differential in signaling induced by the two ligands.

3.3.4 Antagonist density modulated

Modulating antagonist density has a very clear impact on the nature of cross-receptor interactions: the smaller the density, the lower the magnitude of cross-receptor interactions (both antagonizing and enhancing). This trend applies across all tested combinations of ligand density and affinity, as seen in Figure 21 below.

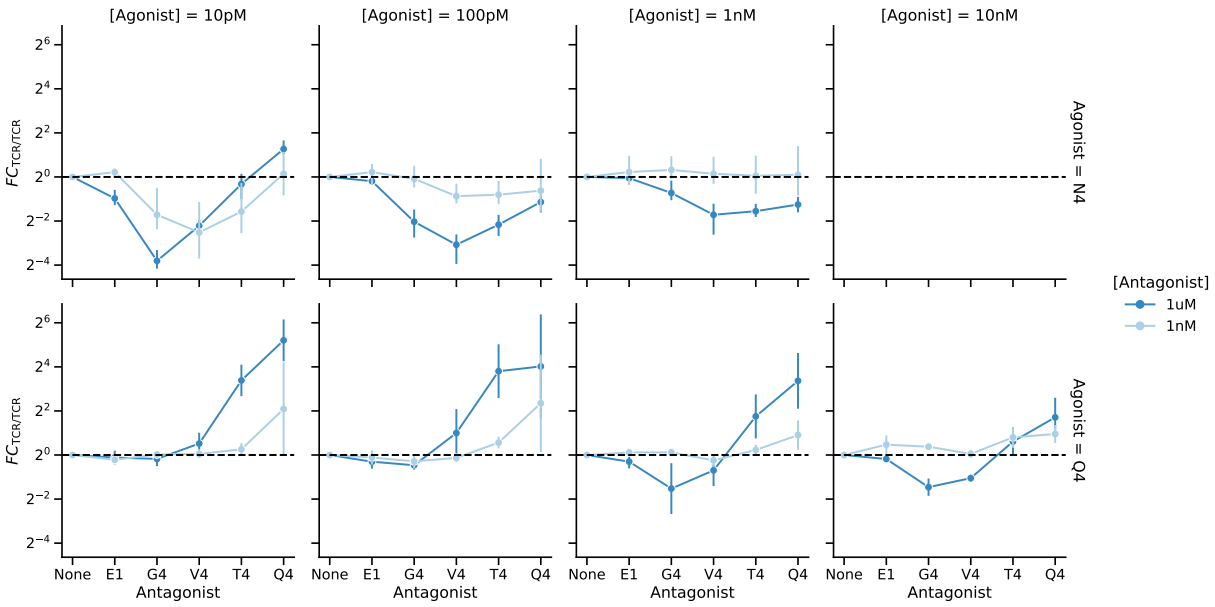

Figure 21: **TCR/TCR crosstalk as a function of antagonist density**. Fold change of OT-1 T cell IL-2 production in response to B6 splenocytes presenting agonist ligand (N4) alone vs agonist+antagonist ligands, plotted to emphasize changes based on antagonist density. Data is plotted from three independent experiments. Dataset also used in Figures 19,20,22.

However, in addition to modulating the magnitude of cross-receptor interactions, changing the antagonist density also shifts the overall interaction curve horizontally; in other words, a lower antagonist density means that stimulation with stronger ligands can now result in antagonism (and vice versa). In other words, it is the absolute level of stimulation a T cell receives through its TCR (a convolved measure of ligand density and affinity) that determines whether or a signal is antagonistic; antagonism can be achieved by either presenting a large quantity of a weak signal or a smaller quantity of a strong signal.

3.3.5 Agonist density modulated

Modulating agonist density has multiple impacts on cross-receptor interactions, as seen in Figure 22 below.

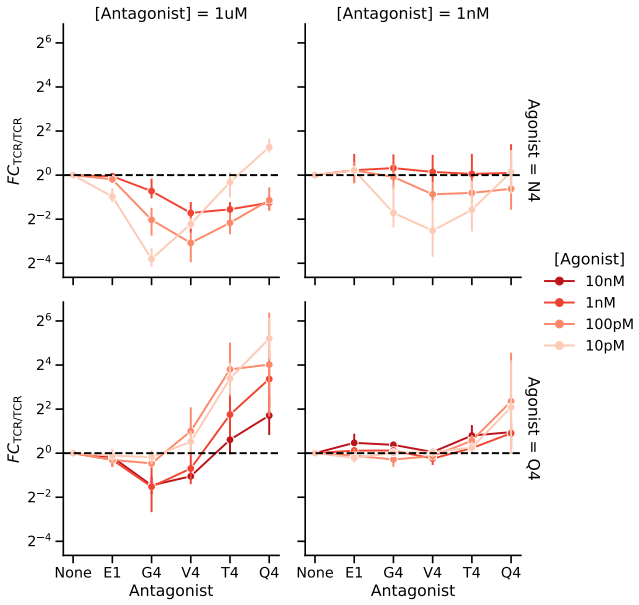

Figure 22: **TCR/TCR crosstalk as a function of agonist density**. Fold change of OT-1 T cell IL-2 production in response to B6 splenocytes presenting agonist ligand alone vs agonist+antagonist ligands, plotted to emphasize changes based on agonist density. Data is plotted from three independent experiments. Dataset also used in Figures 19,20,21.

First, the greater the density, the lower the magnitude of cross-receptor interactions (both antagonizing and enhancing). This trend applies across all tested combinations of ligand density and affinity. This makes intuitive sense, as a higher agonist density means that there are more agonist stimulated TCRs for every inhibitory antagonist stimulated TCRs (so less of the total signal is antagonized). Intriguingly, at least in the 1 µM antagonist, N4 agonist condition, this perturbation also seems to shift the curves to the right, so that a stronger antagonist can now antagonize the ligand. This is likely because a larger agonist dose requires a stronger antagonist to compensate for the effects of the inhibitory signal.

3.3.6 ITAM number changes

TCR/TCR ITAM number perturbations used a different experimental dataset than all other perturbations than in Figure 18, with a more restricted range of antagonist affinities tested. Despite

this limitation, important trends can still be observed in Figure 23 below.

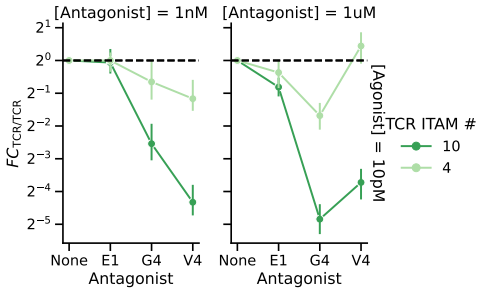

Figure 23: **TCR/TCR crosstalk as a function of TCR ITAM Number**. Fold change of OT-1 10-ITAM TCR (6Y) and 4-ITAM TCR (6F) T cell IL-2 production in response to B6 splenocytes presenting agonist ligand alone vs agonist+antagonist ligands. Data is plotted from three biological replicates.

Reducing TCR ITAM number shifts the antagonist curve upwards, signifying that stimulation across all antigen strengths generally produced less antagonism. This is likely because the reduction in phosphorylation sites also leads to a reduction inhibitory molecule recruitment (e.g. a phosphotase such as SHP-1), in turn reducing cross-receptor antagonism.

3.3.7 Model fitting

To better understand the complex inter-receptor crosstalk patterns observed in the data above, we constructed a model based on Adaptive Kinetic Proofreading framework first described in [2]. A more detailed procedure for model fitting is given in the source publication, but a summary of the procedure is given in Figure 24 below.

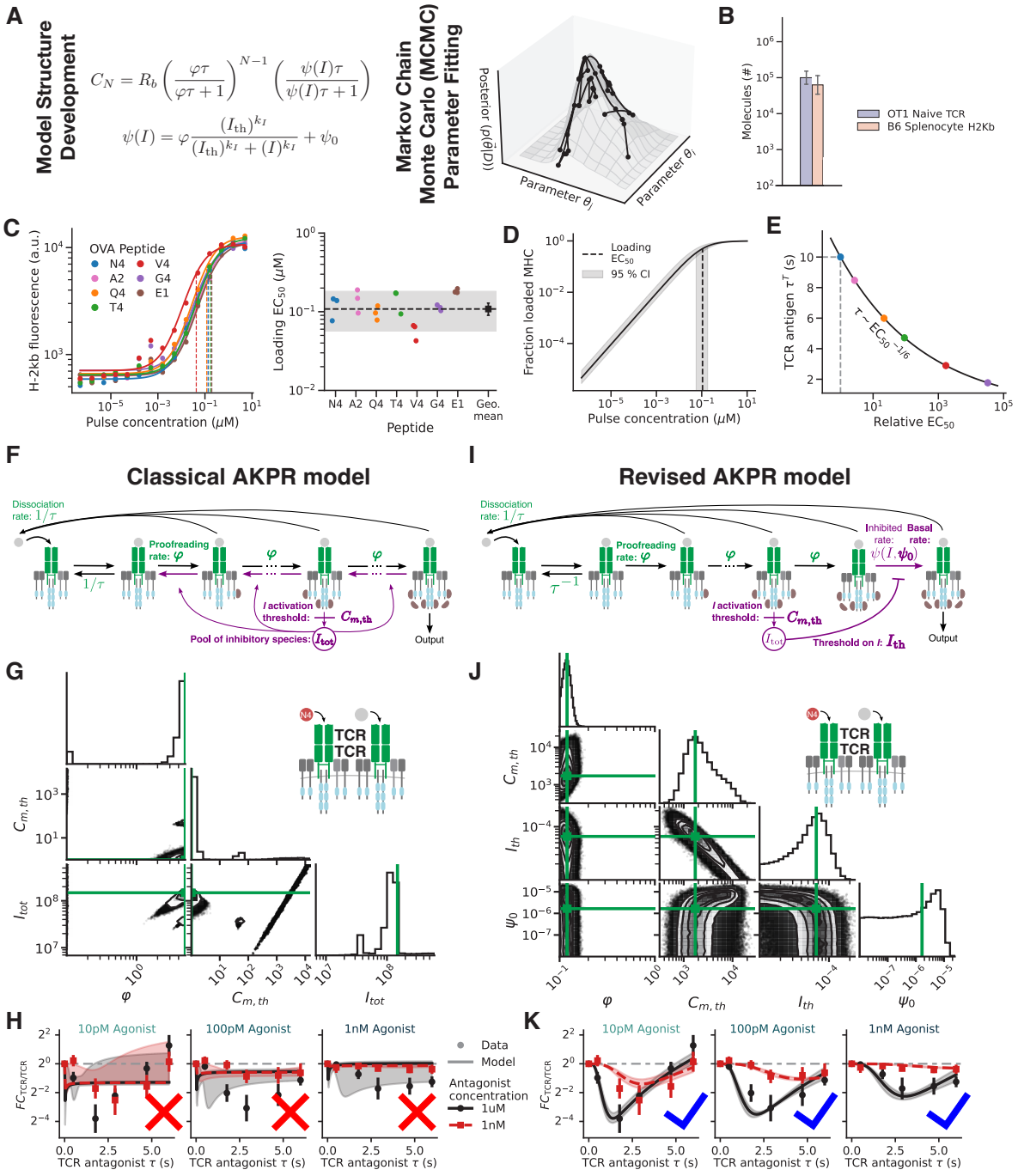

Figure 24: **TCR/TCR Model fitting figure.** (A) Development of analytically tractable mathematical models of receptor crosstalk and intracellular inhibition. Parameters were estimated using MCMC to fit FCTCR/TCR measurements. (B) Experimentally measured ligand (MHC) and receptor (TCR) densities used for TCR/TCR modeling (C) Calibration of OVA peptide MHC (pMHC) loading on transporter associated with antigen processing (TAP)-deficient RMA-S cells, quantified by immuno-fluorescence, as a function of peptide pulse concentration (representative example of three biological replicates shown, left), and peptide loading EC50s inferred from Hill fits on loading curves for each OVA peptide variant (right). (D) MHC loading curve built from EC50s shown in (C).

Figure 24: *(continued)* (E) KPR scaling law used to convert peptide affinity EC50s into ligand binding times t for the model. Error bars in (B) are cell population standard deviations in logarithmic scale. Shaded areas in (C, right) and (D) are 95% CI of loading EC50s across replicates and OVA peptides, and the error bar in (C, right) is the 95% CI on the geometric mean, obtained by bootstrapping. (F) Biochemical reaction network of the classical AKPR model. Bolded parameters were fitted by MCMC. (G) Posterior parameter distributions of the classical model sampled by MCMC to fit TCR/TCR antagonism data. Crosshairs indicate the maximum a posteriori parameter estimate. (H) Classical TCR/TCR antagonism model curves with the maximum a posteriori parameter estimates do not fit the experimental data. (I) Biochemical network of the revised AKPR model, differing from (D) by its inhibitory module, which only impacts the last KPR step. Model parameters are defined in Table S3. (J) Posterior parameter distributions of the revised model, obtained by MCMC. (K) Revised TCR/TCR antagonism model curves with the maximum a posteriori parameter estimates fit well TCR/TCR antagonism data.

Systems of ordinary differential equations describing the behavior of the T cell receptor when stimulated with different strength antigens (Figure 24A left) were fit to the TCR/TCR FC data described above using a standard Markov Chain Monte Carlo algorithm (Figure 24A right). Additional inputs for this model consisted of ligand/receptor densities (Figure 24B) and TCR antigen EC50s (Figure 24C which were combined with a peptide loading fraction curve (Figure 24D) to generate estimates for binding affinity (Figure 24E). These parameters were first used to fit the classical AKPR model described graphically in Figure 24F, however the MCMC simulations were largely unable to converge to unimodal values (Figure 24H), leading to poor fits of the experimental data (Figure 24J). However, after making several adjustments to the structure of the base model, the most prominent of which was to make the negative feedback of the model act only on the last n steps of the phosphorylation cascade, instead of all steps (Figure 24G) the MCMC simulations were able to converge appropriately (Figure 24I) resulting in excellent fits of the data (Figure 24K). The necessity of this modification seems to imply that any negative intracellular inhibitory molecule responsible for mediating antagonism (such as SHP-1) is recruited only by terminally phosphorylated ITAMs of the TCR. Exploring the biochemical validity of this hypothesis could be an interesting avenue for future study.

3.4 TCR/CAR interactions

3.4.1 Manufacturing and validating OT-1/CAR T cells

After our success measuring and fitting experimental TCR/TCR antagonism/enhancement data across a broad range of immunological conditions using an AKPR model, we returned to our main challenge; accounting for variation in TCR/CAR cross-receptor interactions. To accomplish this goal, we decided to express CARs against mouse CD19 in the OT-1 cells we used above. This would allow us to use very similar experimental settings to TCR/TCR antagonism when testing TCR/CAR antagonism, making it more feasible to construct a universal model of T cell activation during dual receptor stimulation. Our general protocol for constructing these OT-1/CAR T cells is shown in Figure 25 below.

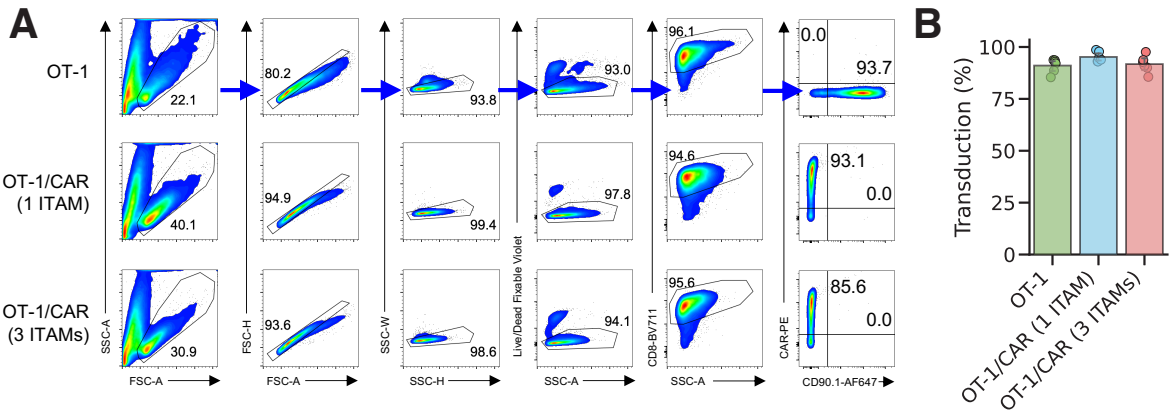

Figure 25: **OT1/CAR-T Construction** (A) Gating strategy for evaluation of OT-1 T cells transduced with the Thy1.1 (CD90.1) reporter vector or the indicated CD19 CAR. (B) Transduction efficacies of different OT-1/CAR T cell manufacturing runs (n = 5 biological replicates).

We packaged empty, 1 ITAM mCD19.28z CAR, and 3 ITAM mCD19.28z CAR plasmids into lentiviral vectors and used them to transduce activated OT-1 cells (Figure 25) to generate "OT-1/CAR" T cells. No sorting was required due to generally high (>85%) transduction efficacies of all three constructs (Figure 25B).

Our first validation step after manufacturing OT-1/CAR T cells was to test how they responded to single ligand stimulations, in order to confirm that mere expression of a CAR (without stimulation) did not significantly impact TCR signaling, and to compare the CAR only signaling of the two different CAR constructs. The steps we took to accomplish these two sub-goals are shown in

Figure 26 below.

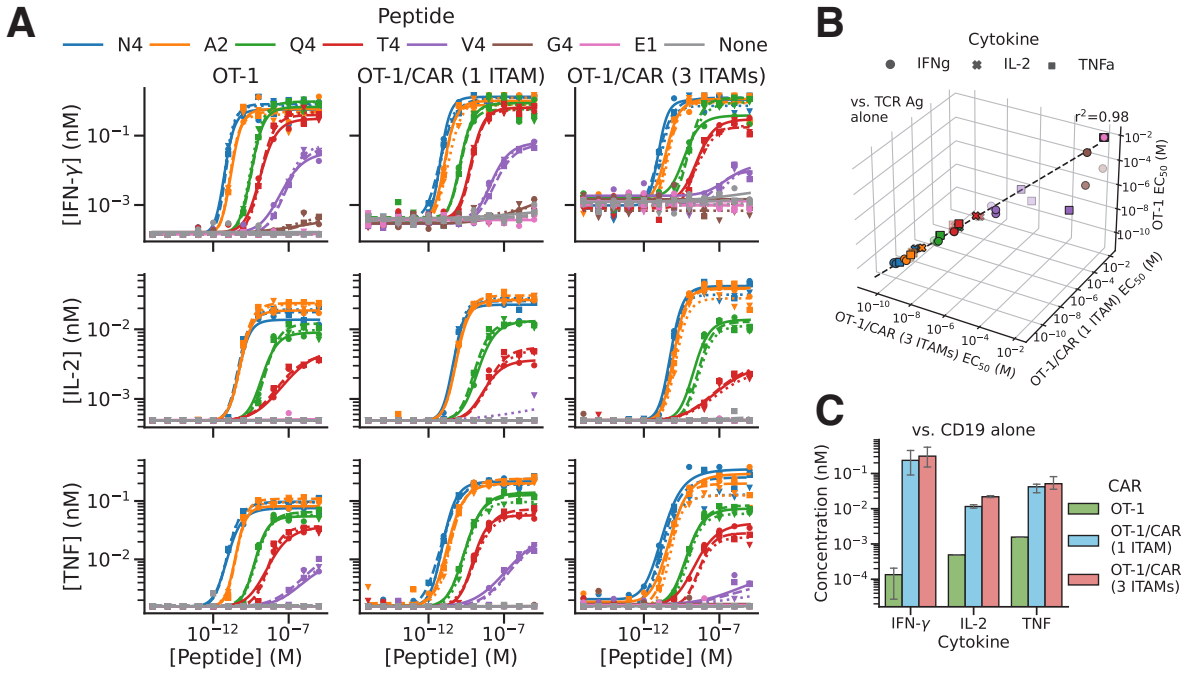

Figure 26: **OT1/CAR-T Single Antigen Validation** (A) Secretion of IFN-g (top), IL-2 (center), and TNF (bottom) by OT-1 (left), OT-1/CAR 1 ITAM (middle), and OT-1/CAR 3 ITAM (right) T cells in response to different concentrations of OT-1 peptide variants (n = 3 biological replicates, 24 h). (B) 3D Correlation of EC50s of peptides reveals similarity in EC50s (peptide qualities) across the three types of T cells. (C) Cytokine production of OT-1/CAR T cells exposed to CAR antigen (mCD19) for 24 h displays striking similarities.

Figure 26A shows dose responses for 24h cytokine secretion of OT-1/CAR T cells stimulated with E2aPBX tumor cells pulsed with different strength SIINFEKL APLs. E2aPBX tumor cells are a murine leukemia cell line that normally express endogenous mCD19. To prevent interference of CAR signaling however, we used a variant of this cell line that its mCD19 gene knocked out, allowing us to compare TCR signaling alone across OT-1/CAR constructs. Besides a noticeable increase in background IFNg secretion as more CAR ITAMs are added into the cells (potentially indicating tonic signaling), the EC50s of each cell type's response to different APLs correlated very well with one another (Figure 26B), indicating that endogenous TCR signaling in OT-1 cells is unaffected by expression of murine CARs. We then stimulated all three cell types with unpulsed mCD19+ E2aPBX tumor cells and again measured cytokine secretion at 24h to compare CAR signaling across constructs. We observed a very minor increase in CAR induced IL-2 production with the

3-ITAM CAR construct compared to the 1-ITAM CAR construct, but the two constructs seemed otherwise induce similar levels of activation in T cells in isolation. The empty vector transduced OT-1 cells could not be stimulated by mCD19+ E2aPBX tumor cells as expected, indicating no significant cross-reactivity between the two ligands and their respective receptor systems.

Our second major validation step of our OT-1/CAR T cells before proceeding to more extensive *in vitro* testing was to conduct dual receptor stimulations of the T cell types by coculturing them with SIINFEKL pulsed mCD19+ (and mCD19- as a negative control) E2aPBX tumor cells. These results are shown in Figure 27 below.

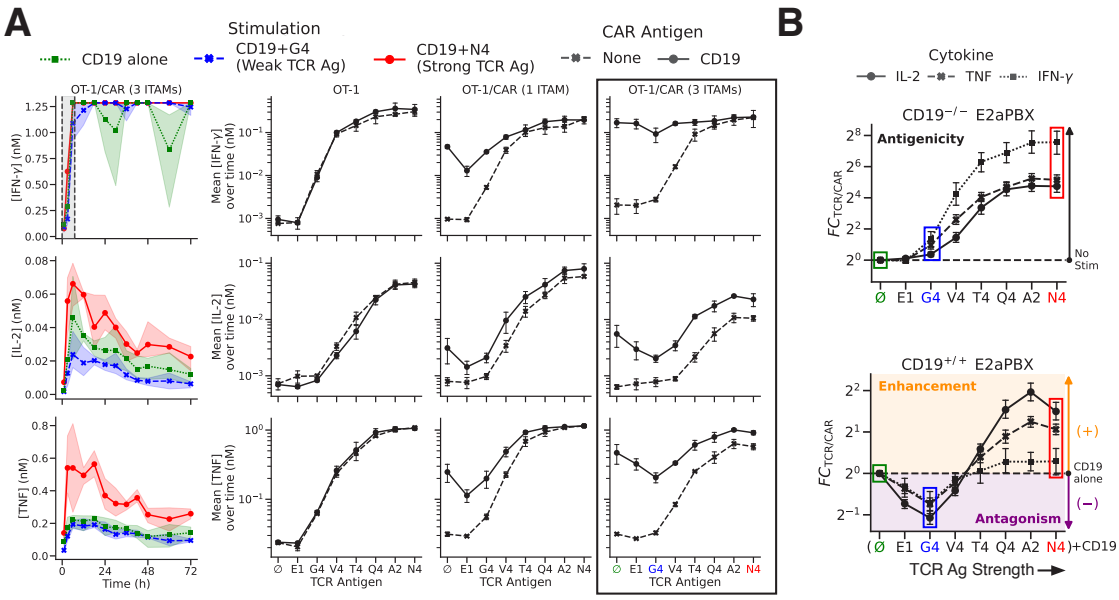

Figure 27: **OT1/CAR-T Dual Antigen Validation** (A) Representative cytokine secretion dynamics (left) and mean secreted cytokine concentrations (right) of OT-1/CAR T cells in response to combinations of TCR and CAR signals of varied strengths (n = 3 biological replicates). Because the IFN-g response was saturated after 6 h of co-culture, only the first three time points (+1, +3, and +6 h, gray area) were utilized to calculate further IFN-g measurements. (B) TCR/CAR crosstalk for dual OT-1/CAR T cells stimulated with CD19 / (top) or CD19+/+ (bottom) E2aPBX cells. y axis represents the fold change (FCTCR/CAR) of responses for a combination of CAR and TCR ligands compared with CAR ligand alone. FCTCR/CARs were measured for IL-2, TNF, and IFN-g production (n = 6 biological replicates).

Figure 27A shows the raw IMMUNOtron measured IFNg, IL-2, and TNF cytokine secretion over time (left) and the mean cytokine concentrations across time measured per TCR antigen (right) of these cocultures. IFNg secretion hit the upper detection limit in our cytokine detection kits very quickly, so we only used timepoints measured before saturation (<=6h, gray region). As expected,

empty vector transduced OT-1 cells as well as CD19KO E2aPBX stimulated OT-1 and OT-1/CAR T cells displayed linear increases in cytokine production as a function of TCR antigen strength. However, when a CAR signal is added into the two OT-1/CAR construct containing cocultures, we can observe a significant increase in the level of cytokine produced by tumor cells unpulsed with TCR antigen. This reflects the effect of CAR stimulation alone. Excitingly, we can see clear evidence of a decrease in T cell activation upon stimulation with weaker TCR antigens, and clear evidence of an increase in T cell activation upon stimulation with stronger TCR antigens, as we had observed previously, across both OT-1/CAR T cell types. We could quantify these changes in overall OT-1/CAR T cell activation induced by adding in a TCR signal by returning to the fold change metric we introduced in the previous section, and modifying it to be a ratio of T cell activation output after dual receptor stimulation to CAR stimulation only induced activation output. This resulting **FC TCR/CAR** metric was computed for the CAR construct with the clearest evidence of TCR induced changes in activation (the 3 ITAM CAR), and plotted in 27B. These data clearly showed that OT-1/CAR T cells were differentially activated by these peptides through TCR stimulation alone (top). In dual receptor stimulation conditions (bottom) we found that TCR signals transitioned from an antagonistic (FC TCR/CAR < 1) to an enhancing (FCTCR/CAR > 1) role as TCR signal strength was increased, and did so in practically the same way across cytokines. In addition, comparing the responses of OT-1/CAR T cells to mCD19- and mCD19+ leukemia cells revealed maximum antagonism upon stimulation with a peptide producing very low (G4) but not zero (E1) TCR activation. Thus, ligands producing TCR signals at the edge of agonism (response), rather than strong ligands, functioned as the best antagonists of CAR function. Altogether, our results conclusively demonstrated that strong TCR stimulation enhances CAR T responses, while weak TCR stimulation antagonizes CAR activity.

3.4.2 High throughput TCR/CAR crosstalk measurements

With our initial observations of TCR/CAR antagonism and enhancement in hand, we could use the full power of the high throughput IMMUNOtron platform to collect TCR/CAR interaction data across a wide range of TCR antigen strengths while simultaneously performing several key immunological perturbations (modulating TCR antigen density, CAR ITAM #, and TCR ITAM

#). The results are shown in Figure 28 below.

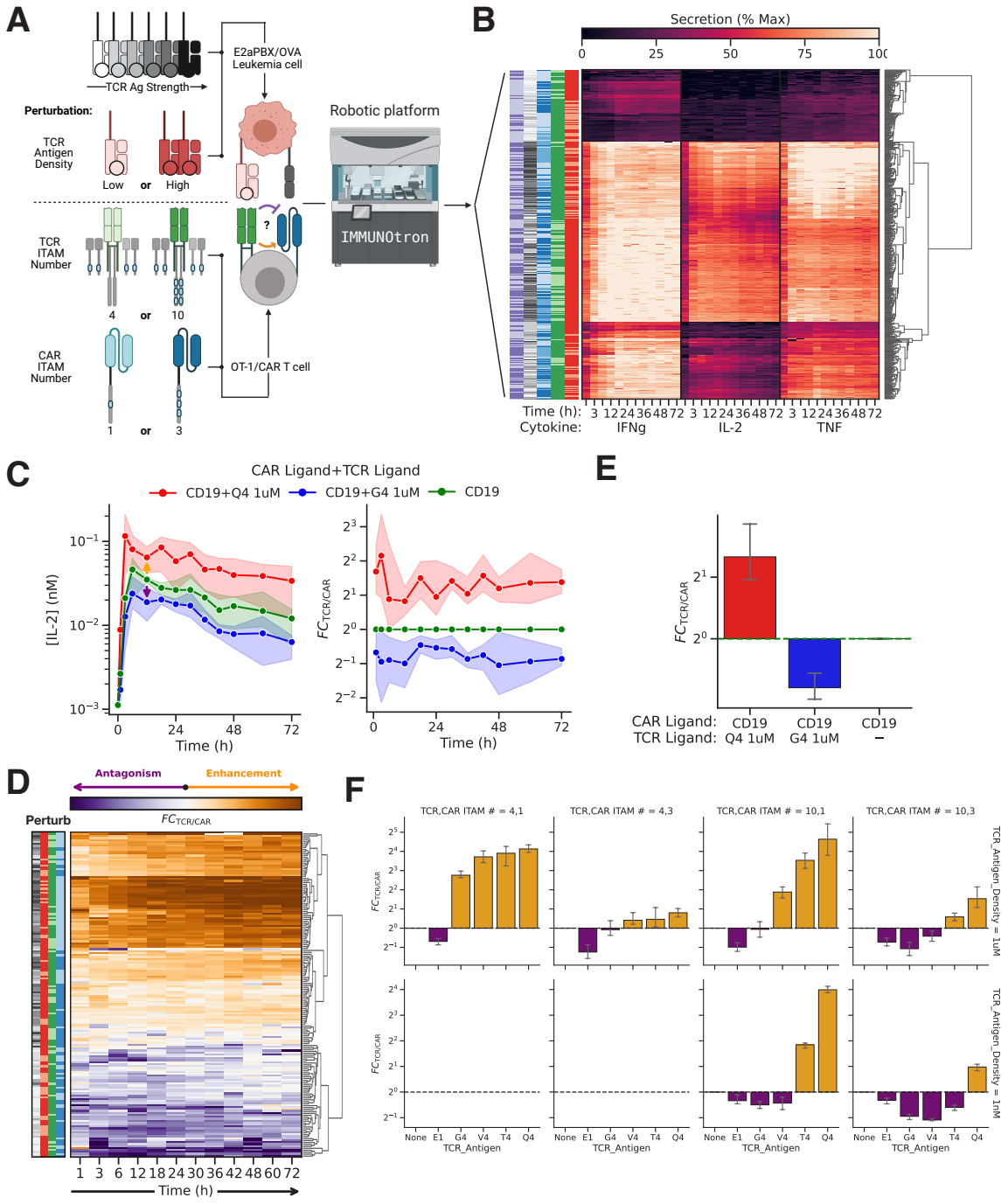

Figure 28: **TCR/CAR interaction ratio calculation procedure** (A) Multiplexed experimental settings to quantify TCR/CAR crosstalk. (B) Full raw TCR/CAR perturbation matrix (20700 datapoints). (C) Example of conversion of raw TCR/CAR cytokine kinetics (left) into TCR/CAR fold changes (right) (D) Full TCR/CAR FC matrix per timepoint (E) Conversion of per timepoint TCR/CAR fold changes into time averaged fold changes (F) All TCR/CAR FC values averaged over time.

We first used the IMMUNOtron to measure cytokine secretion kinetics (Figure 28A) of OT-1/CAR T cells stimulated with a broad range of OT1 TCR peptide strengths and CAR ligand simultaneously, producing the raw cyokine production kinetics data shown in Figure 28B. We then computed fold changes between cytokine outputs of T cells stimulated through both their TCR and CAR vs those stimulated through their CAR alone to determine FC TCR/CAR values per timepoint (Figure 28C). Computing this metric across all perturbation and TCR antigen strength combinations yielded the FC matrix shown in Figure 28D. These values were then averaged across time (Figure 28E) to produce the summary TCR/CAR interaction statistics seen in Figure 28F. Similarly to TCR/TCR interaction ratios, bars below the dashed line indicate the addition of the second (TCR) ligand to the CAR ligand decreased, or antagonized, CAR T cell activation, while ratios above one indicate an increase, or enhancement, of CAR T cell activation. The full matrix again displays a broad range of antagonistic and enhancing outputs depending on the exact ligands combined in TCR/CAR stimulation. The effect of variation along each individual dimension is discussed in detail in the following sections.

3.4.3 Antagonist affinity and density modulated

The general pattern of antagonism and enhancement as a function of antagonist affinity follows a very similar pattern to what was observed in the TCR/TCR case, with very weak TCR antigens often producing marginal levels of antagonism against the CAR, intermediate strength antigens producing the largest degree of antagonism, and strong TCR antigens causing enhancement of the overall signal, as seen in Figure 29 below.

However, the magnitude of antagonism resulting from these TCR/CAR interactions (approximately 2x) is substantially smaller than the 10-100x reduction of signal we commonly observed in the TCR/TCR experiments. This could be due to a variety of reasons, including changes in agonist affinity/density, differences in receptor localization, or less efficient signaling crosstalk between heterogenous receptors. It's important to note that the general pattern of antagonism for the case where we see the most robust antagonism, with 3 CAR ITAMs and 1 µM antagonist density, is most similar to that of the Q4 1 nM agonist condition from the previous TCR/TCR antagonism experiments. This relationship is quantified in Figure 30 below:

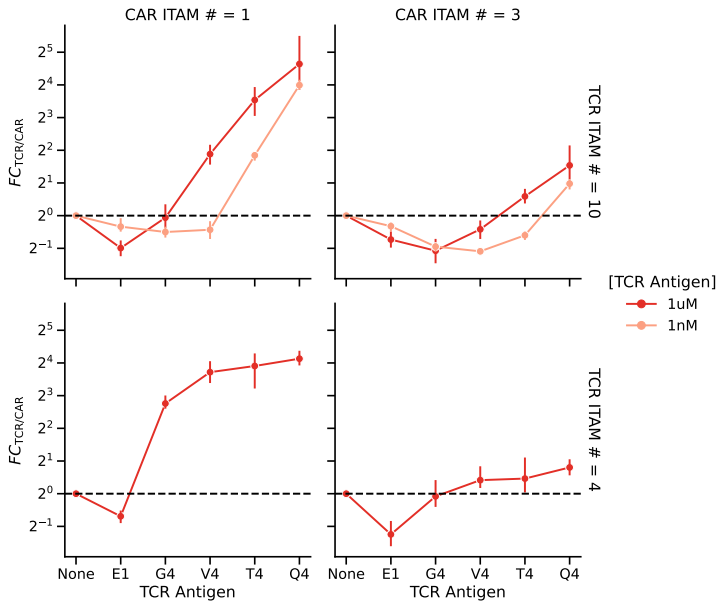

Figure 29: **TCR/CAR crosstalk as a function of TCR antigen (antagonist) density**. Fold change of OT-1/CAR T cell IL-2 production in response to E2APBX leukemia cells presenting CAR antigen alone vs CAR+TCR antigens, plotted to emphasize changes based on TCR antigen affinity. Data is plotted from three biological replicates. Dataset also used in Figure 32.

Figure 30A shows graphs of TCR/TCR fold changes plotted against TCR/CAR fold changes, with the TCR/CAR fold change originating from the 3 CAR ITAM/1 µM TCR antigen density condition that produced the most robust antagonism, and TCR/TCR fold changes varying in their agonist, agonist density, and antagonist density. Certain TCR/TCR conditions clearly do a much better job at recapitulating the magnitude of crosstalk from the TCR/CAR condition (dashed diagonal identity line). Measuring the Lin concordance correlation for each combination of conditions gives us Figure 30B, where the high agonist density Q4 conditions with 1 µM antagonist TCR/TCR data seems to do the best at recapitulating the TCR/CAR data (box). This implies that CAR activation is more similar to a weak agonist like Q4 than a strong one like N4, a concept we had also suggested in [1].

The effect of modulating TCR/CAR antagonist density is similar to what was observed in the TCR/TCR case, where reducing it moves the entire interaction curve to the right, implying stronger antigens can now antagonize the system.

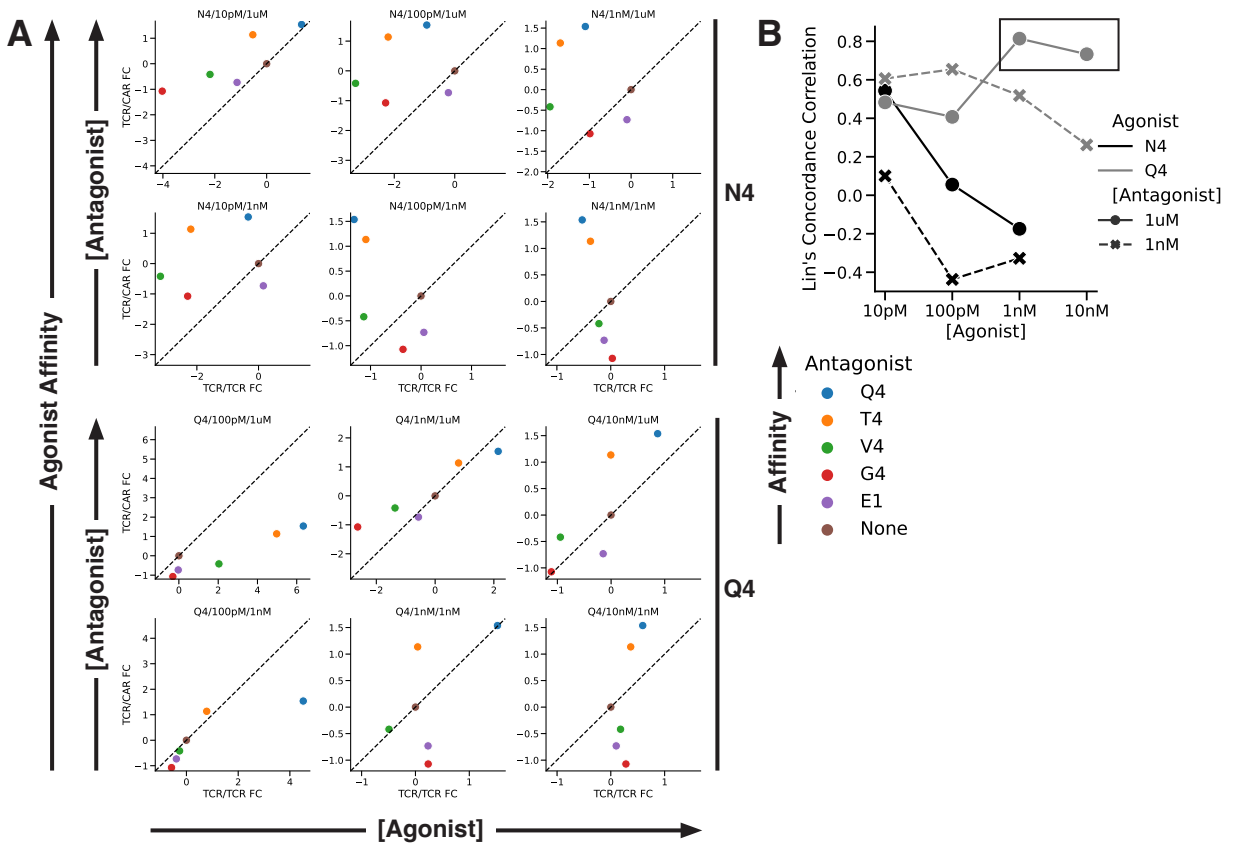

Figure 30: **Identifying TCR/TCR perturbations that most closely resembling TCR/CAR conditions** (A) TCR/TCR fold changes vs TCR/CAR fold changes for different affinity TCR antigens across different combinations of TCR/TCR perturbation; dashed line shows identity (B) Lin concordance correlation values for each TCR/TCR perturbation shows that high density Q4 conditions most closely resemble TCR/CAR conditions

3.4.4 CAR and TCR ITAM number modulated

The use of a CAR in our heterogenous TCR/CAR system afforded us with the opportunity to study the effects of modulating the number of ITAMs on the agonist receptor or antagonist receptor individually, as we could choose whether or not to transduce versions of each receptor with reduced numbers of ITAMs (1 vs 3 for the single CD3ζ domain on the CAR, or 6 vs 10 for the TCR). We begin by examining the effect modulating these individual receptor ITAMs had on the absolute level of cytokine produced in the absence of TCR stimulation, as summarized in Figure 31 below.

Two opposing effects are readily apparent from the above diagram. First, increasing the number of ITAMs on the **unstimulated** receptor seems to have an **inhibitory** role, regardless of stimulation type; see the trending towards significant decrease in IL-2 production upon TCR ITAM number

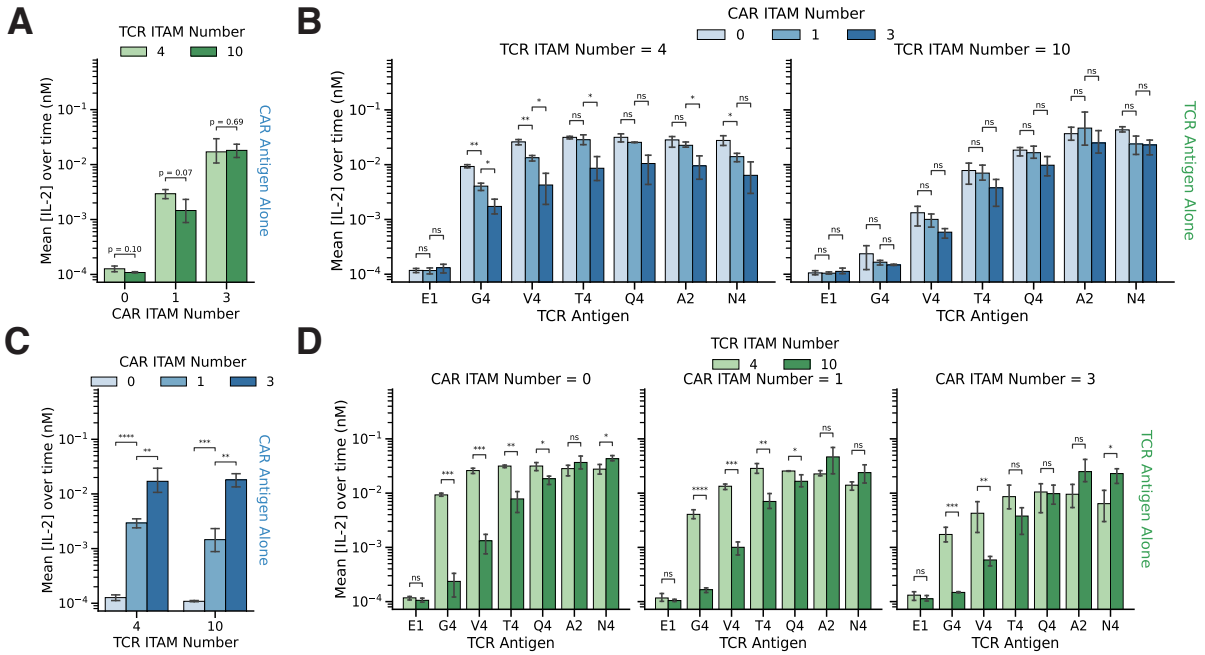

Figure 31: **TCR/CAR Single Antigen stimulation** (A) Comparison of effect of TCR ITAM number modulation when stimulating TCR/CAR system with CAR antigen alone. (B) Comparison of effect of CAR ITAM number modulation when stimulating TCR/CAR system with TCR antigen alone. (C) Comparison of effect of CAR ITAM number modulation when stimulating TCR/CAR system with CAR antigen alone. (D) Comparison of effect of TCR ITAM number modulation when stimulating TCR/CAR system with TCR antigen alone. Statistics in (A-D) were calculated using using two-tailed unpaired Student's t-test. Data in (A-D) are shown as mean ± 95% CI.

increase observed in Figure 31A, where the TCR/CAR T cell is stimulated through its CAR alone, and the significant decreases in IL-2 production as CAR ITAM Number is increased in 31B. Intriguingly, this effect is only apparent in conditions with low numbers of ITAMs overall (across the two receptors); in Figure 31A, only the CAR ITAM number = 1 case shows a decrease in activation, while in Figure 31B, only the TCR ITAM number = 4 case shows any significant decreases in activation. This implies that increases in ITAM number are only inhibitory below a certain "critical mass" of signal. Second, increasing the number of ITAMs on the **stimulated** receptor seems to result in **different effects** depending on stimulation type. With CAR stimulation (Figure 31C) IL-2 production increases as stimulated receptor ITAM number increases, regardless of unstimulated receptor ITAM number. However with TCR stimulation (Figure 31D), IL-2 production decreases as stimulated receptor ITAM number increases, regardless of unstimulated receptor ITAM number. This effect is most apparent at low TCR antigen stimulation strength, as described in [3]. This

seems to imply that there is inhibitory activity associated with TCR ITAMs upon stimulation that is not present upon CAR stimulation. This may partially contribute to why CARs are poor discriminators of antigen strength compared to TCRs [82].

We can now move on to examing the effects of TCR stimulation on CAR activation using the fold change paradigm described previously. The effects of TCR and CAR modulation on TCR/CAR crosstalk are summarized in Figure 32 below.

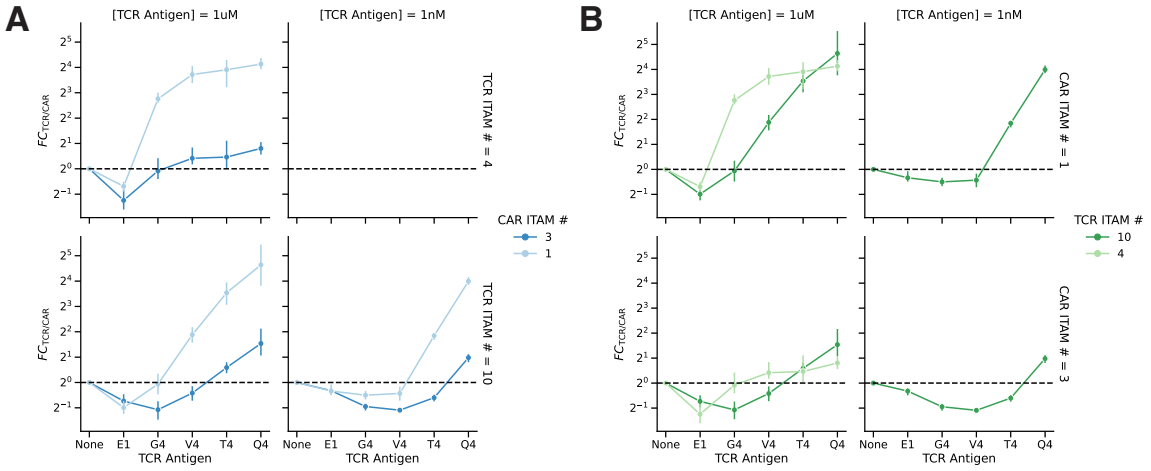

Figure 32: **TCR/CAR crosstalk as a function of ITAM number** Fold change of OT-1/CAR T cell IL-2 production in response to E2APBX leukemia cells presenting CAR antigen alone vs CAR+TCR antigens, plotted to emphasize (A) CAR ITAM number (B) TCR ITAM number. Data is plotted from three biological replicates. Dataset also used in Figure 29.

Increasing ITAM number in either receptor seems to shift the interaction curve to the right, resulting in stronger TCR antigens being able to produce antagonism. While this makes intuitive sense in the TCR ITAM number increase case, as the molecular mechanism driving this difference could be very similar to what was described in the TCR/TCR conditions above, the reason this occurs is less apparent in the CAR ITAM number increase case, and merits further investigation.

It is also readily apparent that while the maximum fold change decreases upon increasing CAR ITAM number, there is no change in the maximum fold change upon increasing TCR ITAM number. This is due to the operational definition of FC R1/R2, where the denominator in the TCR/CAR case is the level of cytokine produced by **CAR stimulation alone**. This changes significantly when CAR ITAM number is increased, but not when TCR ITAM number is increased, resulting in this difference in maximum FC between the two types of receptor ITAM modulation.

3.4.5 Model fitting

To explain the complex pattern of TCR/CAR crosstalk described in the sections above, we used the model created and fit to TCR/TCR interaction data as our foundation. All TCR specific model parameters were reused for the TCR/CAR model, but the basic structure of the model was slightly modified to allow for nonsymmetric receptor interactions. As before, a more detailed procedure for model fitting is given in the source publication [2], but a summary of the procedure is given in Figure 33 below.

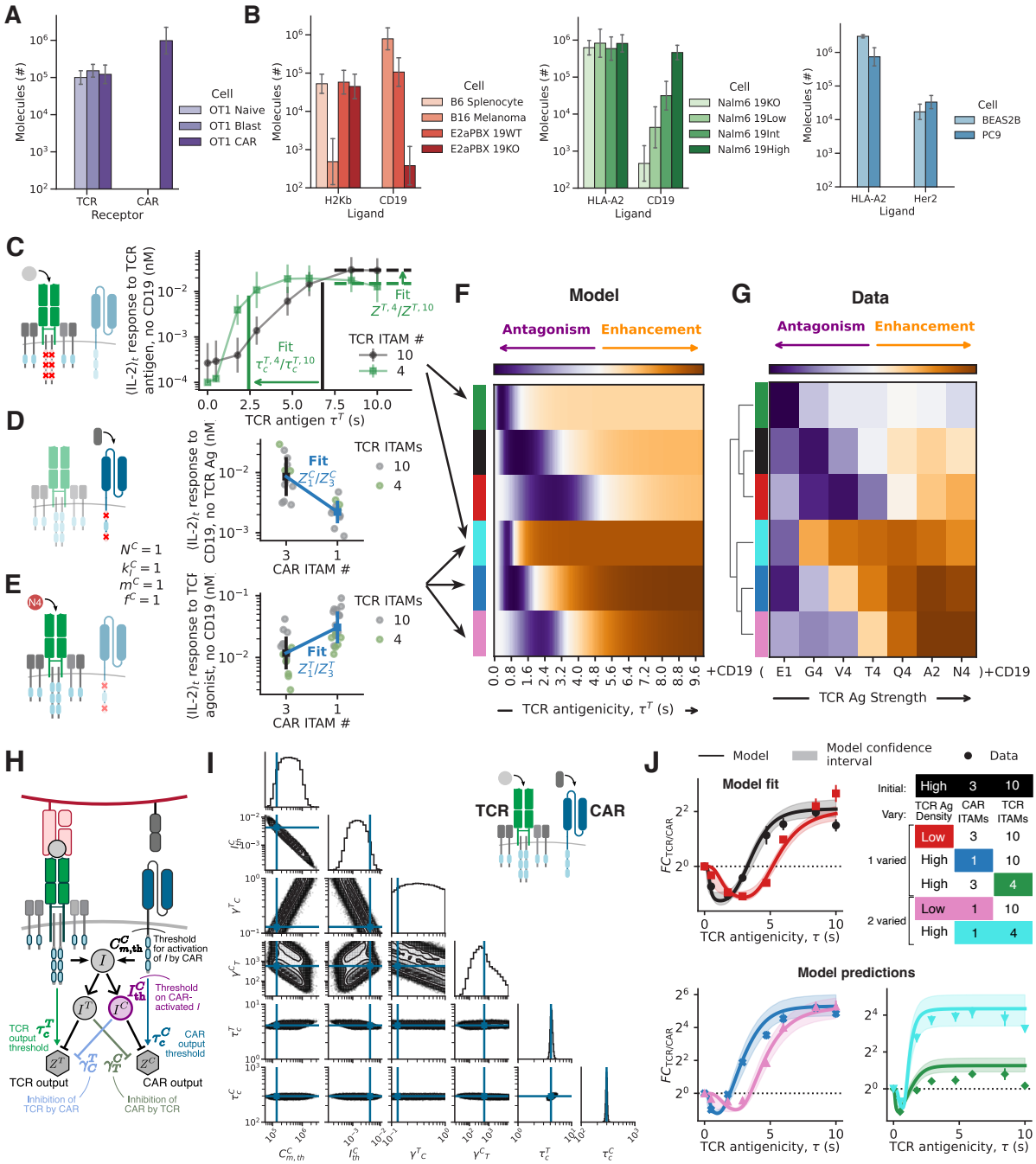

Figure 33: **TCR/CAR Model Fitting Figure** (A) TCR and CAR receptor numbers on the surface of naive, preactivated, and CAR OT-1 T cells. (B) Major histocompatibility complex (MHC) and CAR target antigen numbers on murine antigen-presenting cells (splenocytes) as well as B16 melanoma and E2aPBX leukemic cells (left), human leukemic cells (center), and human lung epithelial (BEAS2B) and adenocarcinoma (PC9) cell lines (right). (C) Correction for 4-ITAM TCR output amplitude and activation threshold, based on experimental IL-2 response to TCR antigens in the absence of CAR antigens. (D) Correction for 1-ITAM CAR output amplitude, based on the responses of 3- vs. 1-ITAM CARs to CD19.

Figure 33: *(continued)* (E) Correction for the effect of 1-ITAM CARs on the TCR output amplitude, based on the response of 1- vs. 3-ITAM CAR T cells to TCR antigens in the absence of CAR antigen. Error bars in (A) and (B) are cell population standard deviations in logarithmic scale. (F) Model predictions of antagonism and enhancement in mixtures of TCR and CAR antigens, for various TCR and CAR constructs and TCR-antigen doses, using the maximal a posteriori parameter estimates and correction factors determined previously on separate data. (G) Experimental data used to fit model. (H) Structure of the model for TCR/CAR crosstalk. Both CARs and TCRs activate a shared inhibitory module, I, reducing the rate of the kinetic proofreading cascade to produce activated TCR (ZT) and CAR (ZC) outputs. (I) Posterior distribution of the revised AKPR model parameters related to CAR and TCR/CAR interactions, sampled by MCMC to fit data for 3-ITAM CARs and 10-ITAM TCRs, for a high dose (1 mM) or low dose (1 nM) of TCR antigen. (J) Best model fit with 95% confidence intervals (top left) accounts for the variable density and quality of TCR and CAR antigens and predicts antagonism for constructs with altered ITAM numbers (bottom). Curve colors correspond to the conditions presented in the panel (top right). Cluster ordering was performed on (F) and applied to (G). Data in (A) and (B) are shown as means ± SD. Error bars in (C)–(E) are SD across time points in two experimental replicates with 2–3 biological replicates each.

Figures 33A and 33B show the flow-cytometry quantified number of receptor and ligand numbers respectively for all T cell and antigen presenting cell types fit in the model. Figures 33C-E show the separate fitting procedure required to fit TCR and CAR ITAM number changes, while Figure 33F-G show the strong recapitulation of TCR/CAR crosstalk by the fitted model. The basic structure of the TCR/CAR interaction model is shown in Figure 33H, and Figure 33I shows the MCMC simulations required to fit the free-floating TCR/CAR interaction parameters. Figure 33J shows the final results of the model fit for both data the model was "trained" on (Figure 33J top) and the results of "predictions" of the model (33A bottom) obtained by manually changing the parameters corresponding to TCR and CAR ITAM number in the model without refitting the experimental data. Excellent agreement between the model and experimental data is observed in essentially all cases, showcasing the rigor of the fit. The one apparent exception is the model's overestimation of the degree of enhancement observed with higher TCR stimulation strengths in the 3 CAR ITAM, 4 TCR ITAM, 1 µM TCR antigen density condition, which implies there may be a nonlinearity in TCR ITAM number the model cannot yet capture.

3.4.6 CD4 T cell TCR/CAR antagonism

Although we had obtained robust evidence of TCR/CAR antagonism across a wide range of immunological conditions in our CD8+ OT-1 system, we had no evidence as of yet as to how this phenomenon would translate to CD4+ T cells, which are usually also transduced with CARs and injected into patients during CAR T cell therapy. We therefore conducted a simple battery of tests (Figure 34) with the SMARTA CD4+ transgenic TCR mice to compare and contrast TCR/CAR antagonism between the two systems, and to determine whether additional parameters in our model would be required to account for differences in signaling between the cell types.

We first constructed SMARTA TCR+ and SMARTA TCR/mCD19 CAR+ T cells using essentially the same manufacturing procedure as when making OT-1/CAR T cells (Figure 34A), resulting in similarly high (>90%) transduction efficiencies (Figure 34B). We then stimulated both types of cells (Figure 34C left) with IA-b MHC-II+ B6 B cells (Figure 34D) that had been pulsed with different affinity LCMV APLs (Figure 34E) overnight (to account for the slower exogenous loading times of MHC-IIs), and collected cytokine secretion timeseries of the resulting cocultures (Figure 34C right). We then computed FC TCR/CARs for each stimulation condition as described earlier, and plotted the results for both TCR+ (Figure 34F top) and TCR/CAR+ (Figure 34F bottom) cells. These data clearly demonstrated that CD4+ T cells could also be significantly influenced by TCR/CAR crosstalk; stimulation of these T cells with weak LCMV antigens (such as P3F) resulted significantly lower levels of IL-2 production than CAR stimulation alone, while stimulation with strong LCMV antigens (such as WT LCMV) significantly enhanced CAR T cell activation. Excitingly, plotting this CD4+ SMARTA FC TCR/CAR data on top of CD8+ OT-1 FC/TCR CAR data as a function of antigen strengths in either system revealed that both T cell types produced very similar similar patterns of TCR/CAR crosstalk as a function of TCR stimulation strength (Figure 34G top), indicating that CD8 and CD4 T cells likely experienced TCR/CAR crosstalk through a very similar mechanism, and that the model would therefore would not need an update to account for both cell types (Figure 34G bottom).

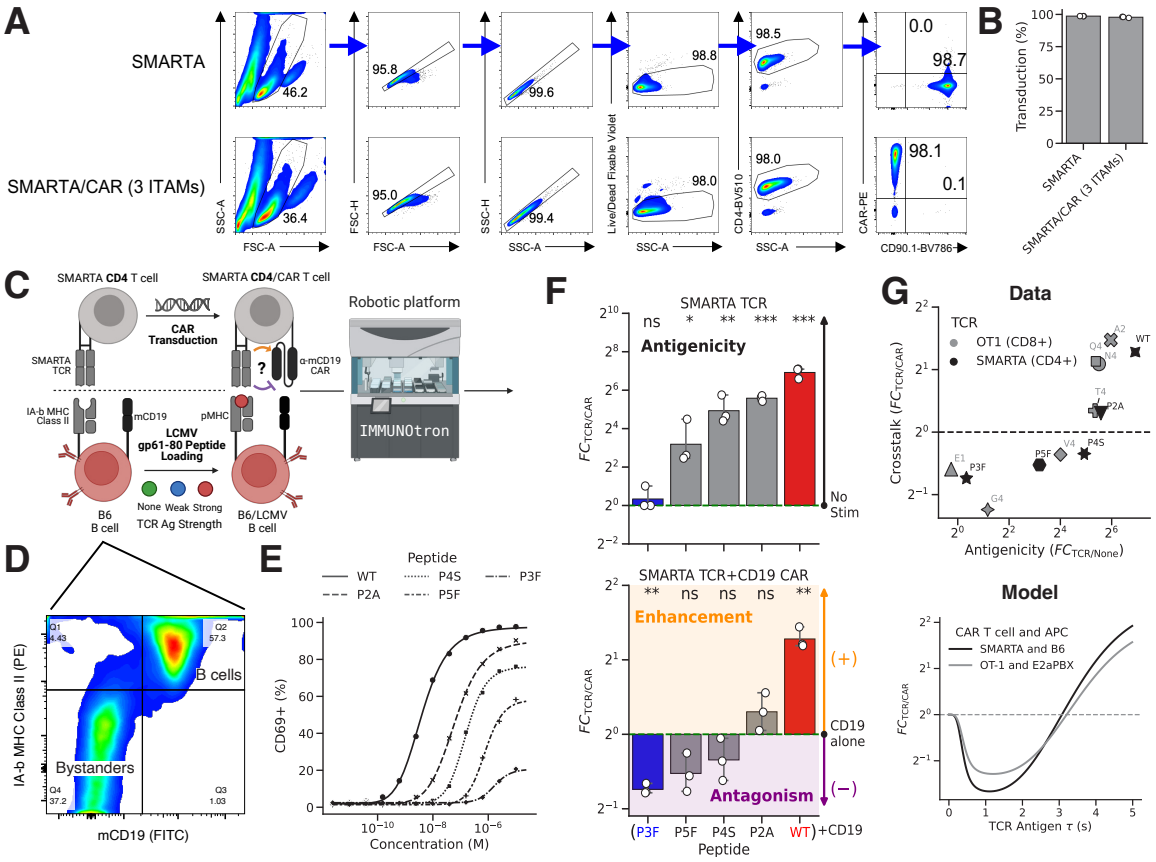

Figure 34: **CD4 T cell TCR/CAR antagonism** (A) Gating strategy for evaluation of SMARTA T cells transduced with the Thy1.1 (CD90.1) reporter vector or the indicated CD19 CAR. (B) Transduction efficacies of different SMARTA/CAR T cell manufacturing runs (n = 3 biological replicates). (C) Experimental scheme to evaluate TCR/CAR crosstalk in CD4+ T cells. Naive SMARTA T cells were transduced with a murine CD19 CAR and then stimulated with CD19+/MHC class II (IA-b)+ B6 splenocytes pulsed with either no additional antigen or one of several gp61-80 peptide variants with differing antigenicities. (D) Flow plot of B6 splenocytes demonstrates that all CD19+ B6 B cells are also I-Ab+. (E) Dose-response curves of gp61-80 peptides covering a range of antigenicities. (F) TCR/CAR crosstalk for SMARTA TCR T cells (top) or dual SMARTA TCR/CD19 CAR T cells (bottom) stimulated with B6 B cells. y axis represents the FC of responses for a combination of CAR and TCR ligands compared with CAR ligand alone, and an FC above 1 indicates that the strength of TCR signal enhances the overall response of the CAR, while an FC below 1 indicates antagonism of the CAR response. The degree of antagonism was evaluated by examining FCs in the production of the cytokine IL-2 (n = 3 biological replicates). (G) Experimental data (top) and model predictions (bottom) and for TCR/CAR crosstalk in CD8+ OT-1 and CD4+ SMARTA systems demonstrate that both T cell types display similar patterns of TCR/CAR crosstalk as a function of TCR-antigen strength. Statistical differences in (F) were calculated using two-tailed unpaired Student's t test. Data in (F) are shown as means ± SD.

3.5 *in vivo* TCR/CAR testing

The success of the model at fitting TCR/TCR and TCR/CAR antagonism data across a wide range of immunological conditions gave us confidence that we could potentially recapitulate our basic *in*

vitro findings *in vivo*.

3.5.1 E2aPBX *in vivo* survival

We started with a simple translation of the E2aPBX tumor+OT-1/mCD19 CAR-T system we had been using to an *in vivo* format, as shown in Figure 35 below.

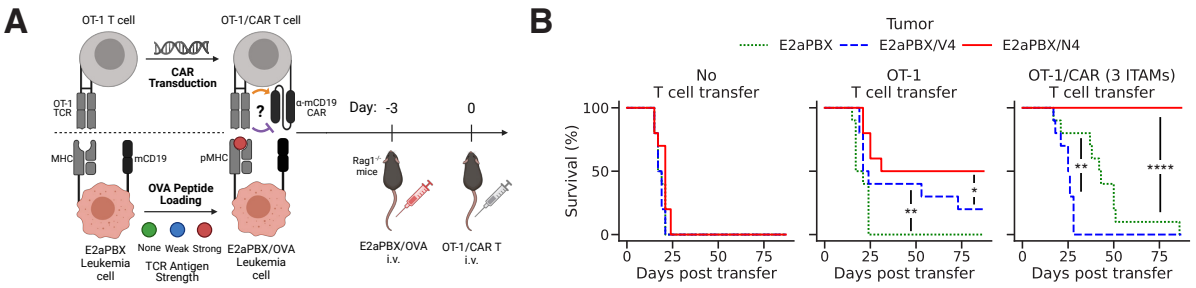

Figure 35: **E2aPBX *in vivo* Survival Figure** (A) Experimental scheme to evaluate effect of TCR/CAR crosstalk *in vivo* (B) Survival curves for mice bearing E2aPBX/OVA cells treated with sham, OT-1, and OT-1/CAR (3 ITAMs) T cells (n = 10 mice/group). Data in (B) are pooled from two independent experiments. Statistics in (B) in were calculated using Kaplan-Meier survival estimates.

By injecting OVA+/CD19+ E2aPBX tumors into RAGKO mice before treatment with various types of immunotherapy, we were able to examine for the first time the impact of different levels of TCR activation on CAR T cell activation *in vivo*. As expected, in the no T cell transfer condition, all three groups of mice died at very similar rates. In the OT1 treatment condition, as the OVA antigen presented on the surface of the E2aPBX tumor cells increased in strength, the survival of mice harboring that tumor also increased, presumably due to greater tumor killing through the OT1 TCR. However, in the OT1/CAR treatment condition, weak TCR stimulation actually resulted in lower survival of the mice than no TCR stimulation (CAR stimulation alone), while strong TCR stimulation dramatically increased mouse survival compared to no TCR stimulation. These findings accurately recapitulated our previous results *in vitro*; in fact the magnitude of effects seen here is much more striking than what we had observed with IL-2 secretion levels *in vitro*, which could be due to the existence of several feedback loops between our *in vitro* readout of choice and final mouse survival that amplify the small *in vitro* effect we observe to the large *in vivo* effects seen here.

3.5.2 B16 *in vivo* survival

As the *in vivo* recapitulation of our *in vitro* data on the effect of TCR stimulation on CAR activation described above was striking, we next sought to examine whether similar effects could be observed in a more challenging but realistic B16 solid tumor melanoma model with low initial levels of TCR antigen. Our basic scheme for testing these effects is shown in Figure 36 below.

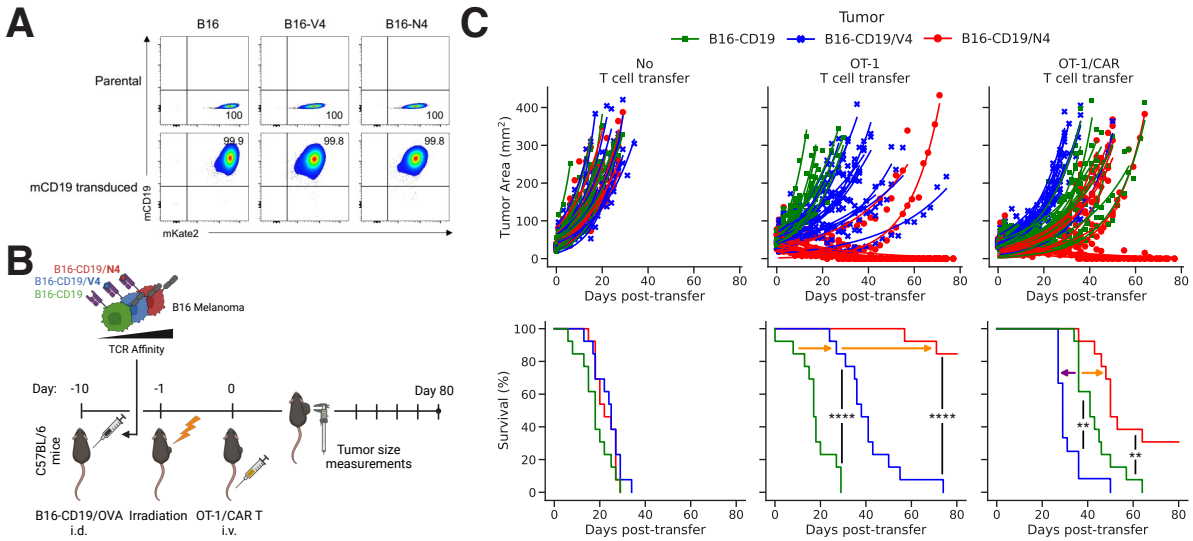

Figure 36: **B16 *in vivo* Survival Figure** (A) Flow plots showing successful transduction of mCD19 into parental B16-OVA cells (B) Experimental scheme to evaluate effect of TCR/CAR crosstalk on survival of mice harboring dual antigen B16-CD19/OVA tumor cells treated with OT-1/CAR T cells. (C) B16-CD19/OVA tumor growth (top) and survival curves (bottom) for sham, OT-1, and OT-1/CAR treated groups (n = 9–13 mice per group). Data are pooled from three independent experiments. Data in (C) are pooled from three independent experiments. Statistics in (C) were calculated using Kaplan-Meier survival estimates.

We can observe that with no T cell transfer, all three groups of mice died at the same rate. With OT-1 T cell transfer, increasing TCR signal strength on the tumor led to increasing survival. Finally with OT-1/CAR transfer, weak TCR signals reduced mouse survival while stronger signals increased mouse survival. Excitingly, all of these results exactly recapitulate what we had observed *in vitro* and *in vivo* using the E2aPBX system previously, despite the drastically different levels of in initial MHC levels between the tumors (Figure 33A).

3.5.3 B16 *in vivo* TILs

The use of the solid tumor model above afforded us with the opportunity to examine how the endogenous TCR influenced CAR T cell activation at a single cell level *in vivo*. Our strategy for doing so is summarized in Figure 37 below.

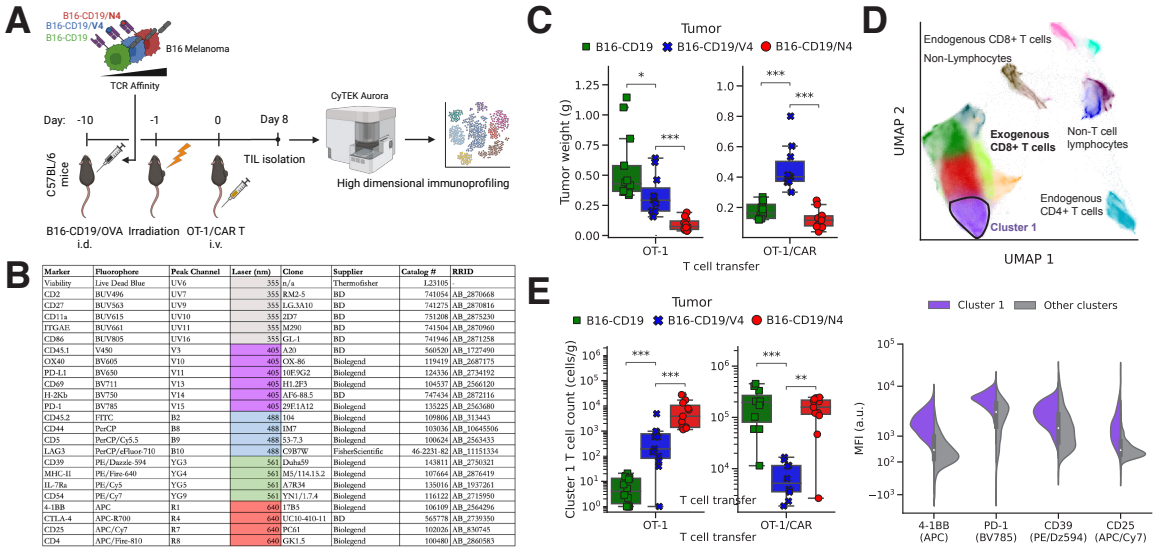

Marker	Fluorophore	Peak Channel	Laser (nm)	Clone	Supplier	Catalog #	RRID
Viability	Live Dead Blue	UV6	355	n/a	Thermofisher	L23105	
CD2	BUV496	UV7	355	RM2-5	BD	741054	AB_2870668
CD27	BUV563	UV9	355	LG.3A10	BD	741275	AB_2870816
CD11a	BUV615	UV10	355	2D7	BD	751208	AB_2875230
ITGAE	BUV661	UV11	355	M290	BD	741504	AB_2870960
CD86	BUV805	UV16	355	GL-1	BD	741946	AB_2871258
CD45.1	V450	V3	405	A20	BD	560520	AB_1727490
OX40	BV605	V10	405	OX-86	Biolegend	119419	AB_2687175
PD-L1	BV650	V11	405	10F.9G2	Biolegend	124336	AB_2734192
CD69	BV711	V13	405	H1.2F3	Biolegend	104537	AB_2566120
H-2Kb	BV750	V14	405	AF6-88.5	BD	747434	AB_2872116
PD-1	BV785	V15	405	29F.1A12	Biolegend	135225	AB_2563680
CD45.2	FITC	B2	488	104	Biolegend	109806	AB_313443
CD44	PerCP	B8	488	IM7	Biolegend	103036	AB_10645506
CD5	PerCP/Cy5.5	B9	488	53-7.3	Biolegend	100624	AB_2563433
LAG3	PerCP/eFluor 710	B10	488	C9B7W	FisherScientific	46-2231-82	AB_11151334
CD39	PE/Dazzle 594	YG3	561	Duha59	Biolegend	143811	AB_2750321
MHC-II	PE/Fire-640	YG4	561	M5/114.15.2	Biolegend	107664	AB_2876419
IL-7Ra	PE/Cy5	YG5	561	A7R34	Biolegend	135016	AB_1937261
CD54	PE/Cy7	YG9	561	YN1/1.7.4	Biolegend	116122	AB_2715950
4-1BB	APC	R1	640	17B5	Biolegend	106109	AB_2564296
CTLA-4	APC-R700	R4	640	UC10-410-11	BD	565778	AB_2739350
CD25	APC/Cy7	R7	640	PC61	Biolegend	102026	AB_830745
CD4	APC/Fire-810	R8	640	GK1.5	Biolegend	100480	AB_2860583

Figure 37: **B16 TILs Figure** (A) Experimental scheme to evaluate effect of TCR/CAR crosstalk on OT-1/CAR TIL phenotype when responding to dual antigen B16-CD19/OVA cells *in vivo*. (B) Spectral flow cytometry panel to measure T cell activation (C) Tumor growth (left) and survival curves (right) for B16/OVA-bearing mice treated by OT-1/CAR T cell transfer (n = 9–13 mice/group). (D) Tumor weights after OT-1/CAR T cell transfer into B16-bearing mice (D8, left). Uniform manifold approximation and projection (UMAP) plot of 3,514,537 tumor- infiltrating leukocytes colored by clusters (center left). Cluster 1 frequency (center right) and its phenotype (right) (n = 10–15 mice/group). Data in (C, E) are pooled from two independent experiments. Statistics in (C, E) were calculated using two-tailed unpaired Student's t-test with Holm-Bonferroni error correction applied.

At a relatively early timepoint after T cell injection (Figure 37A), we sacrificed mice and remove their implanted B16 melanoma, weigh the tumor, and then mince and digest it in order to release the resident tumor infiltrating lymphocytes (TILs). We then stained these TILs with a high dimensional spectral cytometry flow panel focused on rigorously assessing T cell activation state (Figure 37B). This protocol yielded several interesting results.

First, observation of the weights of tumors at time of mouse sacrifice revealed that they also clearly showed the effects of the TCR on CAR activation. In the OT-1 T cell transfer group, increasing TCR antigen strength resulted in lower tumor masses. However in the OT-1 TCR/mCD19

CAR group, the tumor with as weak TCR antigen on its surface had the highest tumor weight, while the tumor with a strong TCR antigen had the lowest tumor weight, recapitulating the same basic trends observed previously with long term survival.

Second, analysis of the TIL population phenotypes (Figure 37D) and frequencies (Figure 37E-left) revealed the existence of an activated exogenous T cell cluster whose frequencies closely corresponded with tumor weights, providing us with a potential single cell correlate for antagonism. The phenotype of this cluster resembled that of a previously published tumor reactive T cell phenotype in human melanoma [83, 84, 85].

The analysis protocol used to identify this cluster is worth highlighting, as it has been useful in other contexts beyond this thesis. A full summary of the protocol is given in Figure 38 below.

After doing basic clean up gating on the TIL samples to remove debris and dead cells (Figure 38A), we concatenated all labeled single cell data together (from two experiments) and passed them through the "Harmony" batch correction pipeline (Figure 38B) [86]. We then clustered the batch corrected single cell data with the package PARC [87] (Figure 38C), yielding 16 clusters across both exogenous and endogenous cell populations with drastically different phenotypes (Figure 38D). Comparing the frequencies of these clusters (Figure 38E) to matched tumor weights (Figure 38F) yielded correlations (Figure 38G), allowing us to identify Cluster 1: the most functionally relevant cluster in our dataset (Figure 38H).

3.5.4 B16 *in vivo* specific killing

Our success at finding a single cell correlate for tumor weight at an early time point prompted us to ask whether the antagonizing and enhancing effects of the TCR on the CAR operated at a local, single cell level in heterogenous tumor populations. To rigorously determine the answer to this important question, we created a protocol to examine specific killing of tumor cells, summarized in Figure 39 below.

We co-injected mice with a 1:1 ratio of melanoma cells expressing the CAR antigen but no TCR antigen and melanoma cells expressing both the CAR antigen and a weak TCR antigen. We then treated the mice with OT-1 or OT-1/CAR T cells and analyzed tumor cell composition 8 days after T cell adoptive transfer (Figure 39A). As expected, the treatment of mice with OT-

1 T cells without a CAR resulted in the preferential elimination of tumor cells expressing both the CAR ligand and the TCR antagonist V4 over tumor cells expressing the CAR ligand alone. By contrast, treatment with OT-1/CAR T cells resulted in significantly higher killing of melanoma cells expressing the CAR ligand alone than the melanoma cells expressing the CAR ligand alongside the TCR antagonist V4 (Figure 39B). These results demonstrate the potential for TCR-mediated antagonism to limit the anti-tumor cytotoxicity of CAR T cells on a granular, cell-by-cell basis, shaping tumor composition and impairing immunotherapeutic efficacy.

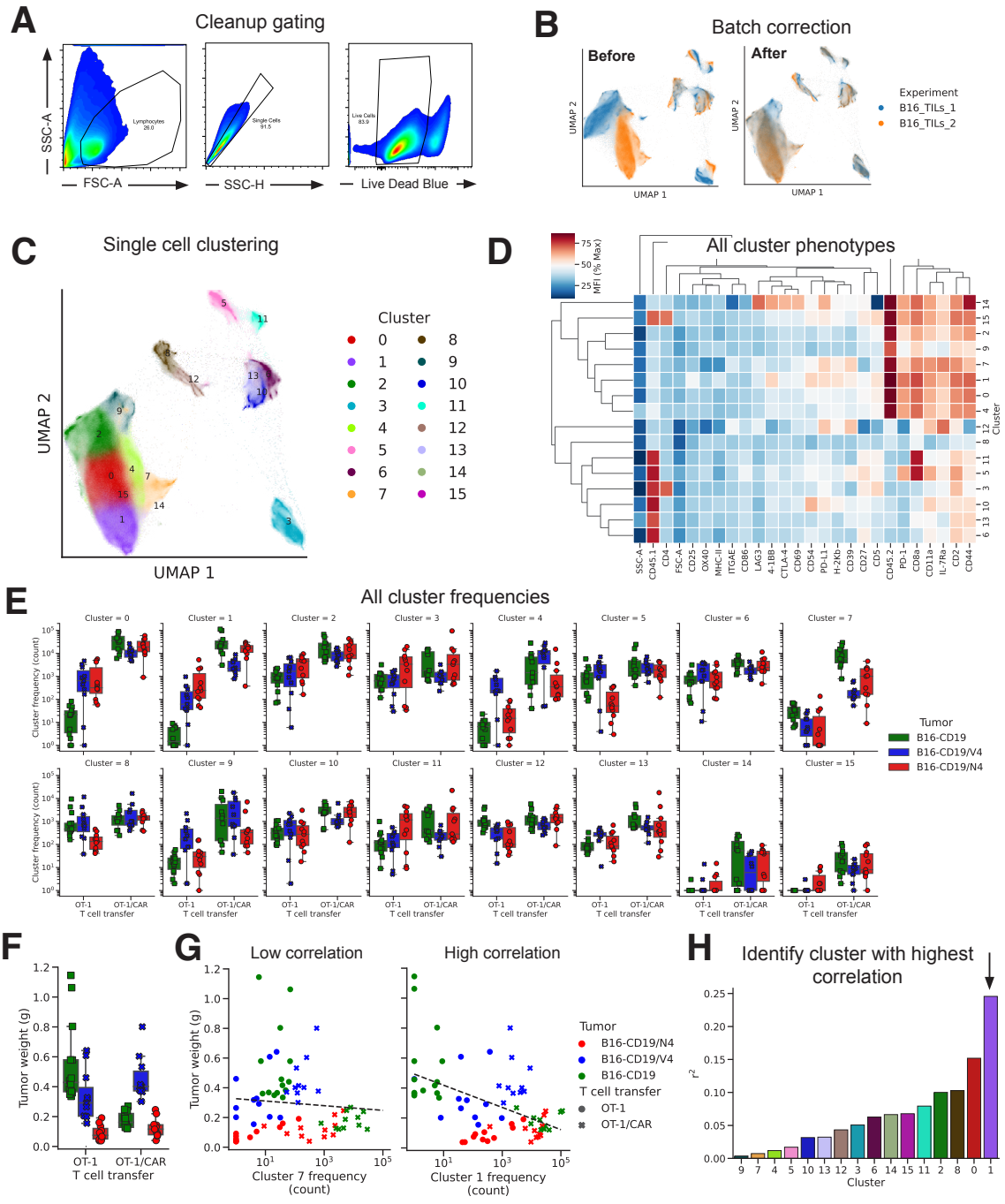

Figure 38: **B16 TILs Figure** (A) All live singlet events from two independent experiments were individually processed through plateypus. (B) Batch correction through the Harmony package was applied to each dataset, which were then merged and (C) clustered with the PARC clustering algorithm at a resolution of 0.6. (D) Phenotypes for all 16 clusters. (E) Cluster frequencies for each of the 16 clusters. (F) Tumor weights for all samples. (G) Representative low (left) and high (right) cluster correlations between tumor weights and cell counts per sample. (H) The frequency of TILs in cluster 1 was identified as having the highest correlation with tumor weight. Data in (B)–(F) are pooled from two independent experiments.

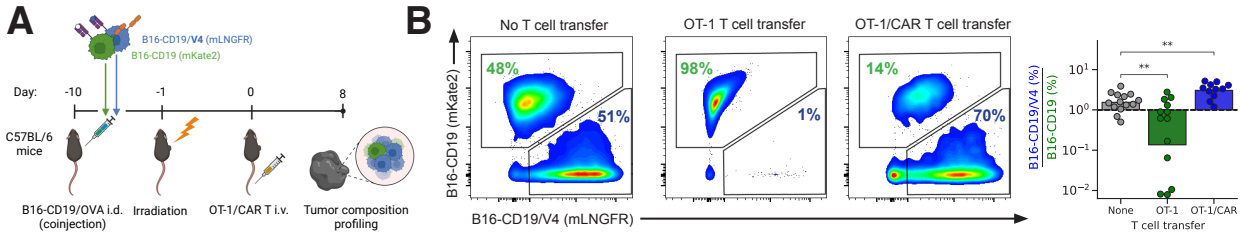

Figure 39: **B16 Specific Killing Figure** (A) Experimental scheme for testing TCR/CAR crosstalk induced effects on tumor killing specificity *in vivo* (B) Representative fluorescence-activated cell sorting (FACS) plots (left), and FCs in cell frequencies (right) for specific killing of B16-CD19 cells over B16-CD19/V4 cells by OT-1/CAR T cells (n = 11–14 mice/group). Data in (B) are pooled from three independent experiments. Statistics in (B) were calculated using two-tailed unpaired Student's t-test with Holm-Bonferroni error correction applied.

4 Which components of the T cell activation signaling cascade are important for inhibitory crosstalk between receptors?

4.1 Introduction

Our results in the previous chapter had convincingly shown that TCR/CAR crosstalk could have a dramatic impact on the overall efficacy of CAR T cell immunotherapy. Our next goal was therefore to understand more about the precise molecular mechanism behind the communication between the two receptors, as learning more about the molecular details could allow us to identify targets to perturb in order to shift TCR/CAR crosstalk in beneficial directions. We were particularly interested in examining how the two receptors interacted spatially in the context of the spatiotemporal junction known between a T cell and the antigen presenting cell, known as the immune synapse [88, 89], as previous work had shown that the two types of receptors produced very differently structured synapses when stimulated individually [90], as displayed in Figure 40 below.

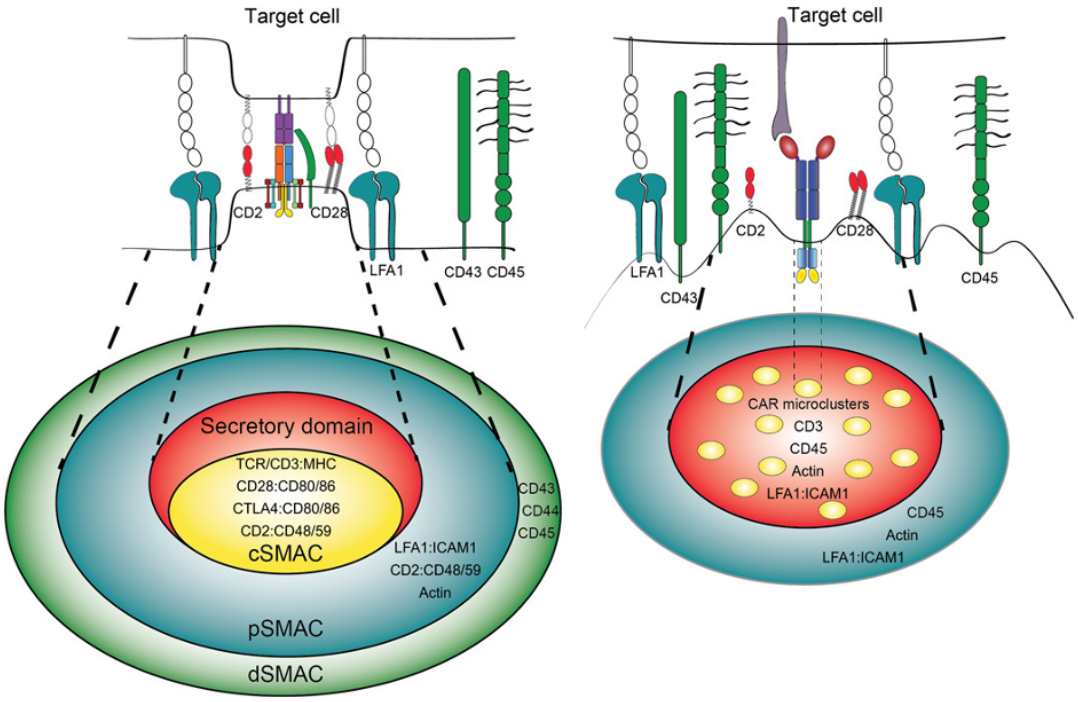

Figure 40: **CAR vs TCR immune synapse, adapted from [90]**

A TCR immune synapse consists of three distinct regions: the central supramolecular activation cluster (cSMAC), which contains the TCRs, costimulatory receptors, and inhibitory receptors that

provide or diminish the initial activation signal, the peripheral supramolecular activation cluster (pSMAC), which contains integrins that help anchor the T cell to the APC during the process of activation, and the distal supramolecular activation cluster (dSMAC), which contains large inhibitory molecules such as CD45 phosphatase, which is initially segregated away from the cSMAC (and therefore TCR-pMHC microclusters) due to its size. Formation of immune synapses can have significant effects on the efficacy of cytotoxic granule delivery (directly related to killing capacity) by a T cell; a lack of an immune synapse can cause T cells to kill targets more poorly than T cells with well-formed synapses [91].

CAR-T cells, by contrast, have been previously shown to form a disorganized immune synapse that is comprised mostly of individual CAR antigen micro clusters intermixed with adhesion molecules such as LFA-1 and signaling molecules such as CD45 [92]. There are several explanations for the disorganized state of CAR-T immune synapses. One hypothesis is that the larger size of CAR scFvs compared to conventional TCRs precludes CD45 molecules from being excluded during initial immune synapse formation, preventing a conventional immune synapse from ever forming [10]. Another hypothesis states that the combined primary and costimulatory signals experienced by a CAR upon antigen stimulation leads to faster traversal through downstream signaling pathways, causing activation to last for too short of a duration to allow for proper immune synapse formation [90]. Interestingly, unlike conventional T cells, the lack of organization of CAR-T immune synapses does not seem to impair granule secretion, and CAR-T cells have been observed to degranulate and detach from their target cell faster than regular TCRs [90]. This surprising disconnect between the granule secretion and immune synapse quality in conventional versus CAR-T cells underscores how critical it is to examine CAR-T cell biology with a perspective unbiased by conventional T cell biology.

4.2 Methods

Generation of NYESO-TCR/CD19-CAR human TCR/CAR T cells: The lentiviral construct expressing a human CD19-targeting CAR is comprised of an anti-CD19 scFv (FMC63) region, a CD8a hinge-transmembrane, a 4-1BB costimulatory signaling domain, and the signaling motif of the ζ-chain (CD19.BB), under the regulation of the EF1a promoter. For confocal imaging,

the green fluorescent protein, mWasabi, was fused downstream of the ζ-chain signaling motif of the CD19.BB CAR construct. Human CD8+ T-cells were stimulated using Dynabeads Human T-expander (ThermoFisher Scientific) with human IL-2 (Proleukin; 40 IU mL^{-1}) in complete AIM-V medium. Activated T-cells were transduced with retroviral or lentiviral supernatants in the presence of protamine sulfate (10 µg mL^{-1}) on day 2 and day 3 by spin-infection (1000 g, 32^oC, 2 hours). Dynabeads and viral supernatants were removed on day 4 and transduced T-cells were transferred into a fresh complete AIM-V medium with human IL-2 (Proleukin; 200 IU mL^{-1}). Transduced T-cells were purified by cell sorting (SONY Biotechnology cell sorter) on day 5 or 6 and then passaged every 2 days in complete AIM-V with IL-2 (200 IU mL^{-1}). TCR, CAR, and TCR/CAR T-cells were frozen at day 14 and then recovered in a complete AIM-V medium with IL-2 (200 IU mL^{-1}) for 24 hours prior to further functional analysis.

SLB based imaging of TCR and CAR co-localization: Supported lipid bilayers (SLB) containing HLAp (30 molec./mm2), CD19 (100 molec./mm2), CD58 (100 molec./mm2), and ICAM-1 (200 molec./mm2) were prepared as previously described. NYESO TCR/ CD19.BBz-mWasabi CAR T-cells were recovered in complete AIM-V medium supplemented with IL-2 (200 IU mL^{-1}) for 24 hours, activated on SLB for 10 min, fixed for 10 min with 4% PFA in PBS + 2 mM MgCl2 and stained with anti-TCRb (clone H57)-Alexa Fluor 647 (1:100 dilution) and WGA CF594 (1:500).

T cell signaling molecule immunoblots: HLA-A*02:01-expressing NALM6 cells were pulsed with NYESO peptides (1 µM) for 2 hours and incubated with human NYESO TCR/ CD19.BBz CAR T-cells at a 10:1 ratio for 2 min. The mixed cells of NALM6 and NYESO TCR/ CD19.BBz were pelleted and immediately frozen down at the end of the incubation. Total proteins were extracted in RIPA lysis buffer supplemented with protease/phosphatase inhibitors (Cell Signaling Technology). Proteins were separated by denaturing gel electrophoresis (SDS-PAGE) and transferred onto PVDF membranes. Membranes were immunoblotted by the sequential stainings with anti-PLC-g1 (D9H10, 5690S) and anti-phospho-PLC-g1 (D6M9S, 14008S, Cell Signaling Technology) rabbit antibodies (1:1,000) at 4^oC overnight and then incubated with an anti-rabbit IgG HRP-linked antibody (7074/7076, Cell Signaling Technology) for 1 h at RT. Antibody staining was

visualized using the Supersignal West Femto maximum sensitivity substrate (Thermo Fisher Scientific) and imaged by ChemiDoc Imaging System (Bio-Rad). For reprobing, blots were incubated in stripping buffer (Thermo Fisher Scientific) for 20 min at RT. Band intensities were quantified using Image Lab software (Bio-Rad). Protein abundance was normalized to total PLC-g1.

4.3 Examining TCR/CAR crosstalk in human cells

4.3.1 Generating human TCR/CAR T cells

In order to quantify the effects of TCR/CAR crosstalk on human cells, we had to opt for a different approach to our experiments with murine cells. We could no longer conduct single CAR transductions into T cells from transgenic organisms that had been genetically modified to only express a single TCR clone to generate TCR/CAR T cells of a known specificity, as the healthy human peripheral blood mononuclear cells we would use as the starting material to engineer TCR/CAR T cells would be polyclonal. Our strategy to get around this issue was to conduct dual transductions of both a CAR and a transgenic TCR. Although the resulting cells would express both an endogenous TCR and the transgenic TCR, we hypothesized that the net effect of any endogenous TCR stimulation across the whole polyclonal population would effectively be zero, allowing us to focus on the effects of the transgenic TCR clone on the CAR.

Our first step was to identify a transgenic TCR and CAR to cotransduce into human T cells. We chose to use a clinically relevant CAR against human CD19 with a 4-1BB costimulatory domain, in order to also examine whether TCR/CAR antagonism would occur with a non-CD28 costimulatory domain. For the transgenic TCR, we focused on a TCR recognizing the NYESO-1 antigen, a tumor associated antigen upregulated in testicular cancer. This TCR had been the subject of numerous studies [26],[5] that had used different series of altered peptide ligands with different affinities for the TCR to examine the discriminatory power of human T cell receptors, making it an ideal candidate for our purposes. To minimize potential endogenous TCR/transgenic TCR mixed α/β chain dimerization, we opted to use a version of this NYESO TCR originally derived from humanized mice in [93]. Our strategy for using these two receptors to create human TCR/CAR T cells is shown in Figure 41 below.

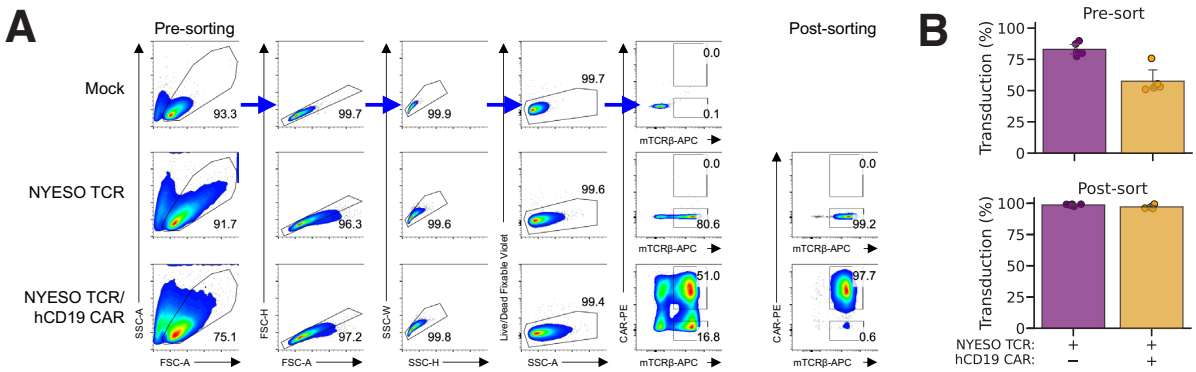

Figure 41: **NYESO/CAR-T Construction** (A) Gating strategy for flow cytometry sorting of double positive NY-ESO TCR/hCD19 CAR (BBz) T cells (left) and purities of sorted cells (right). (B) Percent transduction of T cells expressing the NY-ESO TCR and hCD19 CAR pre- and post-sorting (n = 5 biological replicates). Biological replicates were performed using T cells from different blood donors.

After packaging plasmids encoding DNA for these two receptors into two different lentiviral vectors, we conducted either single or sequential transductions of these two vectors into human PBMCs, then sorted the resulting cells for their single or double positive populations (Figure 41A). Our post sorting efficacy for both TCR+ and TCR/CAR+ cells was >95% (Figure 41B), allowing us to proceed with experimental validation of these cells.

4.3.2 Validating human TCR/CAR T cells

The experimental steps we took to determine whether these human cells also displayed TCR/CAR crosstalk are described in Figure 42 below.

We first used the TCR+ cells we generated to determine the potency of a series of altered peptide ligands originally tested with the human version of the NYESO-1 TCR, in order to confirm that we had a set of antigens with a sufficiently broad range of affinities to examine the full breadth of effects of TCR/CAR crosstalk. The dose responses of these mNYESO TCR+ T cells against a common leukemic tumor called Nalm6 pulsed with these diferent antigens are shown in Figure 42A. The panel of peptides we chose to use did indeed seem to induce a wide range of activation in these T cells, ranging from very strong (9V, endogenous ligand) to nonexistent (4A5P8K), effectively mimicking the range of TCR antigen strengths we had with our murine OT1/CAR system. We then used this series of peptides to conduct dual receptor stimulations by stimulating

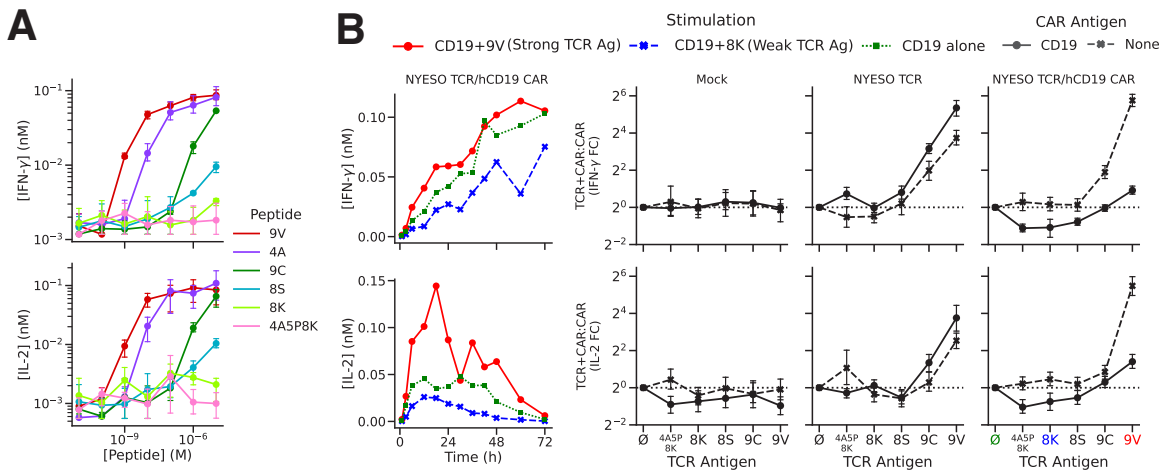

Figure 42: **NYESO/CAR-T Validation** (A) Dose responses of NY-ESO TCR/hCD19 CAR T cells to six NY-ESO peptide variants for the 24-h secretion of IFN-g (top) and IL-2 (bottom) secretion (n = 4 biological replicates). (B) Representative dynamics (left) and FCs (right) in cytokine secretion for NY-ESO and NY-ESO TCR/hCD19 CAR T cells in response to combinations of TCR and CAR signals of varied strengths (n = 4 biological replicates). Data are shown as means ± 95% CI. Biological replicates were performed using T cells from different blood donors.

TCR/CAR+ T cells with hCD19+ Nalm6 cells left unpulsed or pulsed with a high dose of different NYESO APLs (Figure 42B). Computing the FC TCR/CAR for each combination of APL + CAR stimulation as described previously allowed us to observe similar patterns of TCR/CAR crosstalk as what we had seen in the murine OT1/CAR system, where weak antigens reduced (antagonized) CAR activation and strong antigens increased (enhanced) CAR activation. As expected, the effect of TCR stimulation was abrogated when CAR stimulation was removed, either by not transducing the receptor or by using Nalm6 CD19KO cells that lacked a CAR antigen.

4.4 Elucidating mechanism of TCR/CAR crosstalk

4.4.1 Quantifying TCR/CAR co-localization

Observing both TCR/CAR antagonism and enhancement in the NYESO TCR/hCD19 CAR system outlined above confirmed that TCR/CAR crosstalk could be studied in human T cells through a dual transduction procedure. Our next goal was to try to use this system to help uncover the molecular mechanisms of TCR/CAR antagonism. Our strategy for doing so is described in Figure 43.

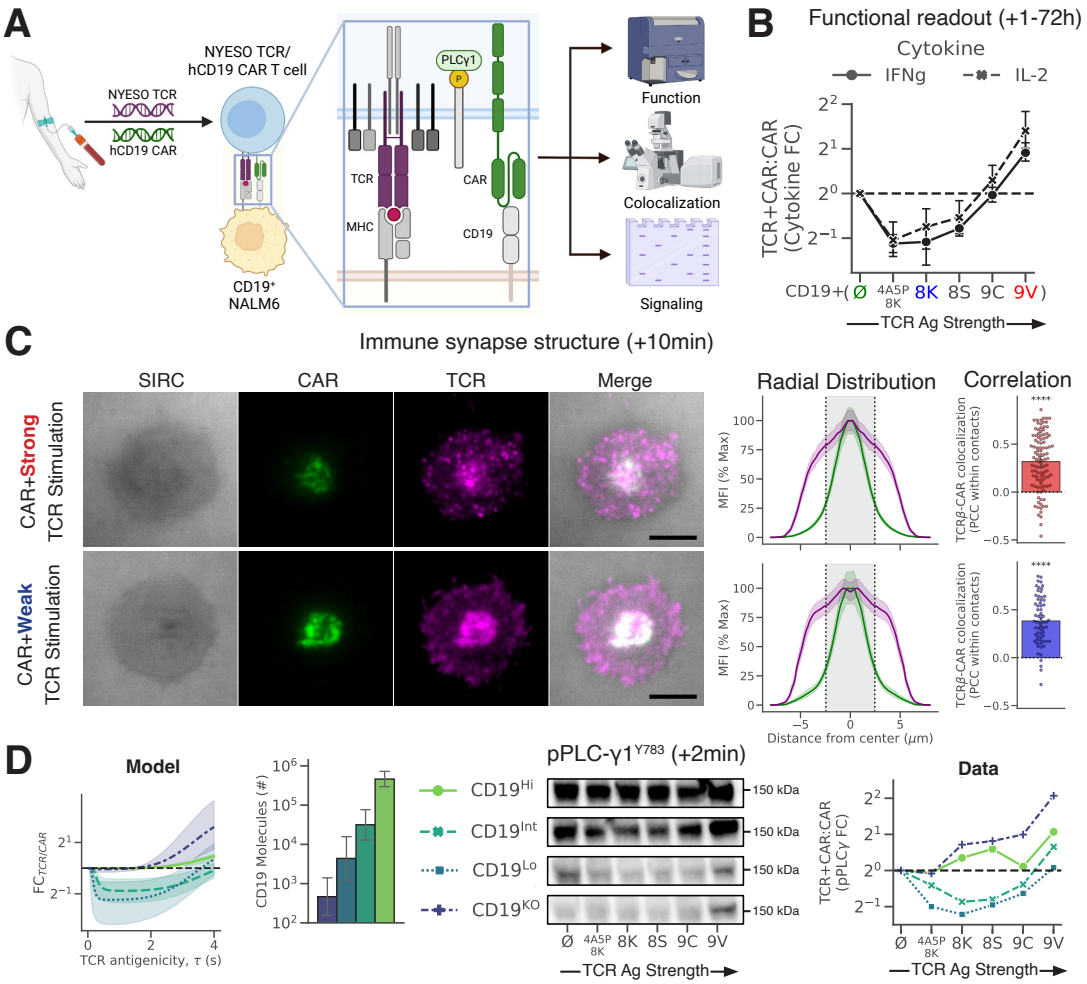

Figure 43: **NYESO/CAR-T Mechanism** (A) Schematic of the generation of dual NY-ESO TCR/CD19 CAR T cells and interactions with targets on leukemic cells. (B) Overall TCR/CAR crosstalk quantification across IFN-g and IL-2 functional outputs demonstrates the functional significance of TCR/CAR antagonism in the human NY-ESO TCR/CD19 CAR system (n = 4 biological replicates). (C) Representative total internal reflectance (TIRF) microscopy images (left) and radial distributions (center) showing the accumulation of TCRs and CARs in the center of the immune synapse when co-engaged with their respective ligands (n = 2 independent experiments, with 64–108 cells per stimulation). Pixel-by-pixel correlation of receptors in TIRF images revealing a moderate level of CAR and TCR colocalization (right). Gray region represents the location of the CAR mask used during correlations. (D) Four HLA-A*02:01+ NALM6 leukemia cell lines with different CD19 densities (center left) and NY-ESO peptides were used to stimulate NY-ESO TCR/CD19 CAR T cells for 2 min. Representative immunoblots (center right) and quantification (right) of phosphorylated PLC-g1 in T cells activated via their TCR and CAR with different peptide variants (strengths indicated) and CD19 levels, respectively. Experimental measurements are consistent with mathematical model predictions (left). Data are representative of two independent experiments. Data in (B) and (C) are shown as means ± 95% CI. Data in (A) are shown as means ± SD. Biological replicates were performed using T cells from different blood donors.

By harnessing the dual transduction protocol, we could insert a fluorescently labeled version of the CAR along with the TCR in order to facilitate tracking of both receptors through microscopy and other signaling assays (Figure 43A). For these experiments, we used the same panel of peptides as in the previous validation assay, with the 8K and 9V peptides serving as the archetypal weak and strong TCR stimulations respectively (Figure 43B). In Figure 43C we used TIRF microscopy to examine how the two receptors interacted spatially in the immune synapse during dual receptor stimulation. After preparing a supported lipid bilayer with hCD19, ICAM-1, CD58, and either a weak pMHC or strong pMHC, we seeded NYESO TCR/hCD19 CAR T cells onto the SLBs, fixed cells after 10 minutes, and then examined the resulting T cell interactions with the SLBs. Individual images (Figure 43C left) seemed to suggest that the CAR localized very specifically to the center of the immune synapse during stimulation. The TCR remained more diffuse, but still exhibited a significant increase in density towards the center of the synapse. These receptor distributions are displayed using the radial distributions shown in Figure 43C center, and the Pearson correlation coefficient for the TCR and CAR signal within portion of the synapse occupied by the CAR (gray region in Figure 43C center) was quantified for both stimulation types in Figure 43C right. There was a distinct lack of difference between the structures and PCCs of the immune synapses stimulated with different strength TCR antigens during joint TCR/CAR stimulations, indicating that the mechanism for TCR/CAR antagonism was unlikely to be due to differences in synapse organization efficiency. The moderate positive PCCs between the TCR and CAR for both weak and strong TCR stimulation instead supported our hypothesis that the two receptors were likely in close enough spatial proximity during any degree of joint TCR/CAR stimulation for promiscuous inhibitory molecules to move between the receptors.

4.4.2 Effect of TCR/CAR crosstalk on early signaling events

If a proximal TCR signaling inhibitor was indeed responsible for mediating TCR/CAR antagonism, we would expect antagonism to be observable fairly early on in the T cell receptor signaling cascade. We therefore chose to examine the effects of TCR/CAR crosstalk on the phosphorylation of Phospholipase C γ (PLCγ), a key early signaling molecule in the T cell receptor cascade (Figure 43D) [94, 95]. To maximize our chances of observing differences in activation in this very proximal

TCR activation event, we chose to stimulate our TCR/CAR T cells with modified Nalm6 tumor cells that expressed progressively lower levels of hCD19, the CAR ligand, in order to slow down overall T cell activation rates. Decreasing CAR ligand (agonist) levels while keeping TCR ligand (antagonist) levels constant was also predicted by the model to increase the effect TCR stimulation would have on overall activation (Figure 43D left). We therefore conducted western blots to measure phosphorylated PLCγ levels in T cells stimulated with four different levels of CD19 and six different strength TCR ligands two minutes after stimulation (Figure 43D center). Excitingly we observed clear evidence of a reduction in pPLCγ levels during stimulation with weaker TCR antigens, an effect that was especially apparent in the series of stimulations with CD19 low Nalm6 cells, as predicted by the model. Figure 43D right shows the TCR/CAR FC levels for these pPLCγ levels normalized by total PLCγ levels for each stimulation. These curves heavily resembled those of previous experiments for much further downstream markers of T cell activation such as cytokine production, strongly supporting our hypothesis of TCR/CAR antagonism being mediated by a proximal signaling inhibitor.

5 How can we improve the design of immunotherapies to account for crosstalk between immune receptors?

5.1 Introduction

Our experiences with TCR/CAR crosstalk convinced us that the effects were worth attempting to account for when designing new generations of immunotherapy beyond conventional cell therapies, whose limitations are shown in Figure 44 below.

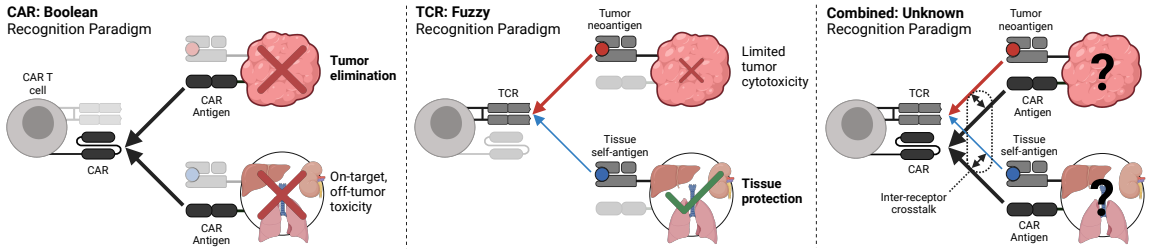

Figure 44: **Comparison of conventional forms of cell based cancer immunotherapy**

CAR T cells can be used against highly expressed surface antigens, leading to robust tumor killing, but have difficulties distinguishing between targets on healthy tissue vs tumors, often leading to off-target toxicity that can limit which antigens are amenable to this form of immunotherapy (Figure 44 left). Meanwhile, TCR T cells can be used against any presented antigen, including antigens derived from intracellular proteins which allows them to target tumor restricted antigens and therefore circumvent off-target toxicity. However, most tumor neoantigens are fairly weak compared to viral antigens, often leading to incomplete tumor killing (Figure 44 center). Could we use our newfound knowledge of how these two types of receptors interact (Figure 44 right) to engineer a more precise form of immunotherapy? Our basic strategy for doing so, creating an **A**ntagonism **E**nforced **B**raking **S**ystem (AEBS) for T cells, is summarized in Figure 45 below.

The utility of the AEBS relies on the fact that the tumor neoantigens targeted by many TCR T cells originate from a healthy protein. In fact in certain cases, an oncogenic driver mutation in a single protein coding gene alone is sufficient to convert a previously healthy cell into a cancerous cell (Figure 45A top). Therefore, these types of neoantigens are *restricted* to tumor cells, while their unmutated self antigen counterparts are *restricted* to tissue cells. By screening through TCR clones

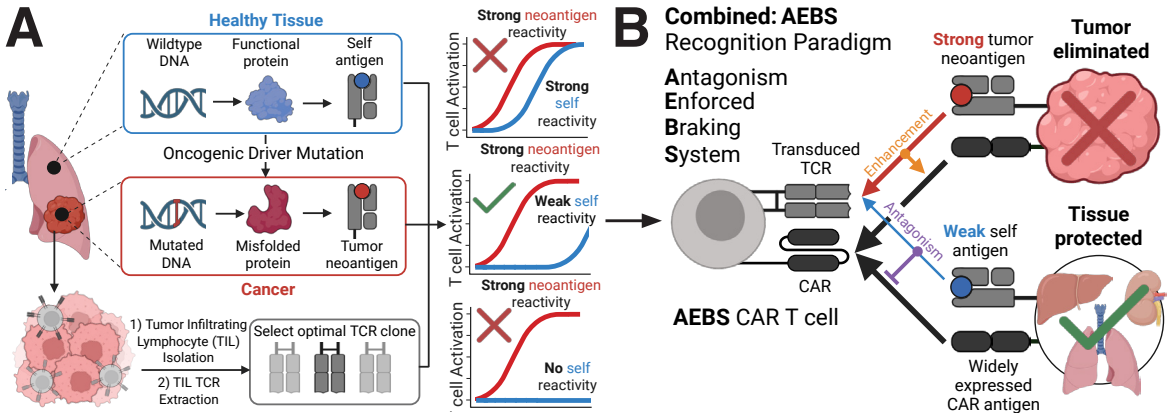

Figure 45: **Strategy for improving immunotherapeutic specificity using crosstalk** (A) Schematic for identifying TCRs with potential for beneficial crosstalk with CAR T therapies (B) Explanation of Antagonism Enforced Braking System (AEBS) concept

isolated from tumor infiltrating lymphocytes (Figure 45A bottom), selecting a clone that displays **strong** binding against a tumor neoantigen and **weak** (but nonzero) reactivity against their self antigen counterpart (Figure 45A right), and pairing it with a CAR against a ubiquitously expressed CAR target protein, we could potentially harness TCR/CAR crosstalk to inhibit CAR activation against tissue (due to antagonism resulting from weak self-antigen recognition by the co-transduced TCR) and *simultaneously* enhance CAR activation against tumor (due to enhancement resulting from strong tumor neoantigen recogition by the co-transduced TCR) (Figure 45B). The following sections in this chapter detail our efforts to use this protocol to design and validate this innovative immunotherapy design.

5.2 Methods

Generation of human HHAT-TCR/HER2-CAR or p53-TCR/HER2-CAR T cells: The lentiviral construct expressing the human HHAT^{L8F}/WT peptide-specific TCR (generously provided by Dr. B. Baker, University of Notre Dame) consists of the α-chain and β-chain of the TCR (TIL302), the Furin-P2A sequence, and the mouse Thy1.1 reporter gene under the regulation of the EF1a promoter. The lentiviral human HER2-targeting CAR comprises the anti-HER2 scFv (4D5) domain, the 28 or 4-1BB costimulatory domain, and ζ-chain (HER2.28 or HER2.BB) domains. Anti-HER2 CAR encoding genes were inserted upstream of the TIL302-Thy1.1-encoding

regions and connected with a Furin-P2A sequence to generate the monomeric AEBS CAR construct. Lentivirus expressing these HHAT TCR, CD19 CAR, and HER2 CAR transgenes were generated by transfecting HEK293T cells with the 3rd generation packaging plasmid (pMDLg/pRRE, pRSV-Rev and pMD2.G from Addgene) together with the TCR- or CAR-encoding transfer plasmid using lipofectamine 3000 (ThermoFisher Scientific). Retrovirus expressing p53 TCR (P4196-AV6/BV11) and p53 TCR (P4196-AV5/BV6) transgenes were generated by transfecting HEK293-GP cells with the RD114 envelope plasmid together with the TCR-encoding transfer plasmid using lipofectamine 30000. Viral supernatants were harvested 48 and 72 hours after transfection and used for transduction of primary T-cells. Human CD8+ T-cells were stimulated using Dynabeads Human T-expander (ThermoFisher Scientific) with human IL-2 (Proleukin; 40 IU mL^{-1}) in complete AIM-V medium. Activated T-cells were transduced with retroviral or lentiviral supernatants in the presence of protamine sulfate (10 µg mL^{-1}) on day 2 and day 3 by spin-infection (1000 g, 32^oC, 2 hours). For the transduction of p53 TCR (P4196-AV6/BV11) or p53 TCR (P4196-AV5/BV6) with HER2 CARs, the retroviral supernatant and/or lentiviral concentrated virus were coated on the retronectin-treated cell-culture plates on day 2 by high speed spin (2000 g, 32^oC, 2 hours) and the activated T-cells were transferred on the virus coated plates. Dynabeads and viral supernatants were removed on day 4 and transduced T-cells were transferred into a fresh complete AIM-V medium with human IL-2 (Proleukin; 200 IU mL^{-1}). Transduced T-cells were purified by cell sorting (SONY Biotechnology cell sorter) on day 5 or 6 and then passaged every 2 days in complete AIM-V with IL-2 (200 IU mL^{-1}). TCR, CAR, and TCR/CAR T-cells were frozen at day 14 and then recovered in a complete AIM-V medium with IL-2 (200 IU mL^{-1}) for 24 hours prior to further functional analysis. For HHAT TCR T-cells used for HHAT peptide library screening, the transduced T-cells were bulk-sorted by anti-Thy1.1 magnetic beads as following transduction with HHAT TCR-Thy1.1 lentiviral vectors.

p53 antigen presenting cell line immunoblots: The AU565, TYK-nu, AGS, Malme-3M, BEAS-2B-A0201, and BEAS-2B-A0206 cell lines were pelleted and immediately frozen down after the harvest. Total proteins were extracted in RIPA lysis buffer supplemented with protease/phosphatase inhibitors (Cell Signaling Technology). Proteins were separated by denaturing

gel electrophoresis (SDS-PAGE) and transferred onto PVDF membranes. Membranes were immunoblotted with anti-p53 (R175H mutant, HL1129, MA5-46935, Thermo Fisher Scientific) rabbit antibody (1:500), anti-p53 (DO-1, 18032, Cell Signaling Technology) mouse antibody (1:1,000) and anti-β actin (AC15, AM4302, Thermo Fisher Scientific) mouse antibody (1:20,000) at 4^oC overnight and then incubated with an anti-rabbit or anti-mouse IgG HRP-linked antibody (7074/7076, Cell Signaling Technology) for 1 h at RT. Antibody staining was visualized using the Supersignal West Femto maximum sensitivity substrate (Thermo Fisher Scientific) and imaged by ChemiDoc Imaging System (Bio-Rad).

Dose-response assays T-cell and tumor cocultures were prepared as follows. E2aPBX or NALM6 leukemia cells were pulsed with peptide at the indicated concentrations for 2 h at 37^oC, washed once, mixed with murine or human TCR/CAR T-cells in complete RPMI medium (200 µl final volume), and spun at 500g for 10 s to form contacts. Samples were incubated at 37^oC for 24 hours. Supernatants of samples were removed and transferred to a separate plate for BD Cytokine Bead Array (CBA) analysis following manufacturer protocols. The remaining cells were stained with anti-CD25 and anti-4-1BB antibodies at 4^oC for 20 min, washed, and subsequently analyzed by flow cytometry.

***in vitro* on-target/off-tumor cytotoxic assay:** The *in vitro* on-target/off-tumor cytotoxic assays of the HHAT TCR/HER2 CAR platform were performed by co-culturing GFP+ PC9 with/without 10 µM $HHAT^{L8F}$ peptides, 10 µM $HHAT^{WT}$ peptides, or 10 µM of a combination of $HHAT^{L8F}$ and $HHAT^{WT}$ peptides; or GFP+ BEAS-2B-A0206 cells with/without 10 µM $HHAT^{WT}$ peptides (1×10^4) with T-cells (2.5×10^4) in complete AIM-V medium. The *in vitro* on-target/off-tumor cytotoxic assays of the p53 TCR/HER2 CAR AEBS CAR were performed by co-culturing GFP+ cells (AU565, 2.5×10^4; TYK-nu, 5×10^3; AGS, 2.5×10^4; Malme-3M, 2.5×10^4; BEAS-2B-A0201, 1×10^4; BEAS-2B-A0206, 1×10^4) with T-cells (2.5×10^4 for AU565; 5×10^4 for TYK-nu; 1×10^4 for AGS; 5×10^3 for Malme-3M; 1×10^4 for BEAS-2B-A0201 and BEAS-2B-0206) in complete RPMI medium. Plates were imaged every 2 hours using an S3 Incucyte live-cell analysis instrument (Sartorius, Göttingen, Germany). The cytotoxic activity of CAR T-cells was

evaluated by quantifying the Total Integrated Green Fluorescence Intensity (PC9, AGS, BEAS-2B-A0201, BEAS-2B-A0206) or total area of the cells (AU565, TYK-nu, Malme-3M) over time using Incucyte software. At the end of the Incucyte assay, supernatants were harvested and their cytokine content was evaluated using a Human Flex Cytokine Bead Array kit (BD Biosciences).

***in vivo* model of on-target/off-tumor toxicity:** *in vivo* on-target/off-tumor cytotoxic assays were performed by adoptive transfer of engineered T-cells following PC9 and BEAS-2B engraftment. To test the *in vivo* on-target/off-tumor cytotoxicity of mock, HHAT TCR, HER2 CAR, and AEBS CAR T-cells, $HHAT^{L8F}$ -expressing PC9 cells (0.5 $\times$ 106) were intradermally injected into a flank of the NSG mice. $HHAT^{WT}$-expressing HLA-A*02:06+GFP+ BEAS-2B cells (2 $\times$ 106) were intravenously injected into the PC9-bearing NSG mice via tail vein 3 days after the PC9 inoculation. Either mock, HHAT TCR, HER2 CAR, and AEBS CAR T-cells (5 $\times$ 106) were intravenously injected into PC9 and BEAS-2B bearing NSG mice 4 days after BEAS-2B transfer. PC9 tumor sizes and body weights were measured every 3 - 4 days using a digital caliper and a scale over time. BEAS-2B burden in the thoracic cavity in PC9/BEAS-2B bearing mice was evaluated by bioluminescent imaging using the Xenogen IVIS Lumina (Caliper Life Sciences or Perkin- Elmer) before T-cell transfer as a baseline and post-T-cell transfer every 3 - 4 days. The PC9/BEAS-2B-bearing mice were intraperitoneally injected with 3 mg of D-luciferin (Caliper Life Sciences), imaged with 1 min exposure 4 min after the peritoneal luciferin injection, and bioluminescent images were analyzed as the total radiance for mice by radianceQuantifier (https://github.com/soorajachar/radianceQuantifier). All PC9/BEAS2-B-bearing mice were randomized prior to T-cell transfer. Animals were closely monitored for signs of graft-versus-host disease (GvHD) and other toxicity as evidenced by loss of fur, diarrhea, or conjunctivitis as well as for the high tumor burden. Animals were euthanized at a predetermined study endpoint or by an endpoint for xenogeneic GvHD following IACUC guidelines.

5.3 Theoretical basis and rationale for AEBS strategy

Before undertaking this approach however, we wanted to estimate both how difficult constructing this type of system would be and how much of a need there was to improve CAR T cell specificity.

Our efforts at answering these two important questions are detailed in the sections below.

5.3.1 Estimating the probability of a neoantigen specific TCR being antagonized by its self-antigen counterpart

A critical prerequisite for building our AEBS system is to find a TCR with the correct level of both self and neoantigen reactivity. Our strategy for estimating the frequencies of these types of TCRs made heavy use of our mathematical model of TCR/CAR crosstalk, and is described in Figure 46 below.

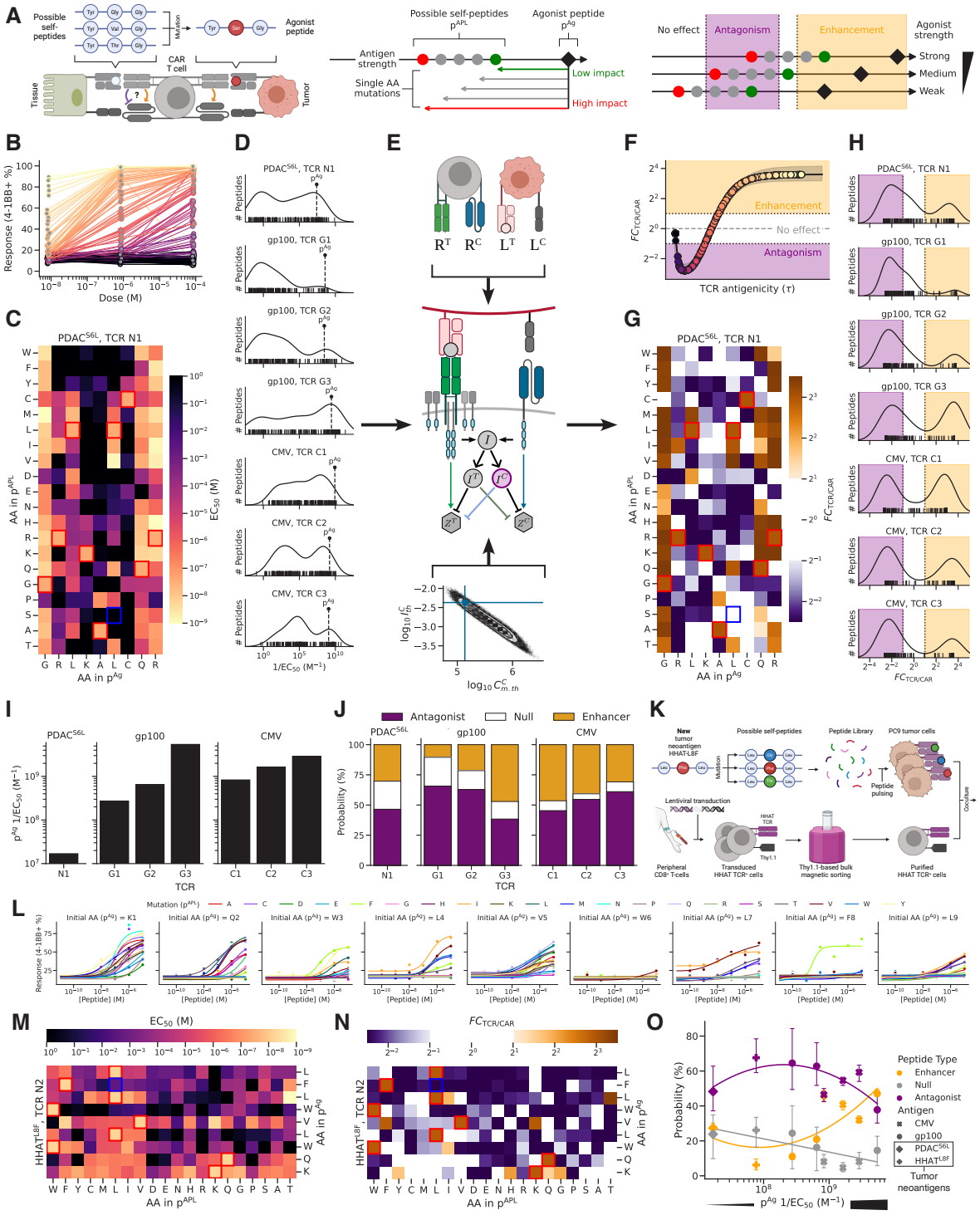

Figure 46: **Probability of self antagonism** (A) Theoretical scheme to evaluate the proportion of tumor neoantigens possessing an antagonistic self-counterpart. (B) Dose-response curves for 7 TCRs responding to 1,204 peptides comprising agonist antigen (pAg) and altered peptide ligands (pAPL). Dataset derived from [96]. (C) Representative EC50s for all single amino acid mutations of a cancer neoantigen. (D) Distributions of EC50s across all 7 TCRs. Dashed lines represent the EC50 for pAg used to clone the corresponding TCR.

Figure 46: *(continued)* (E) Pipeline to predict antagonism: ligand/receptor data (top) and parameters previously determined by MCMC (bottom) were passed to the model (middle) to estimate the magnitude of TCR/CAR crosstalk. (F) FC TCR/CAR as a function of TCR antigenicity (1/EC50s) for antigens analyzed in (C). (G) Representative predicted FC TCR/CAR for all single amino acid mutations of the neoantigen activating TCR N1. (H) Distributions of FC TCR/CAR across all 7 TCRs. (I) EC50s for pAg for each TCR. (J) Percentage of pAPL predicted to antagonize, enhance, or not affect CAR activation for each pAg/TCR pair. (K) Experimental scheme for estimating the impact of HHAT L8F-specific TCR engaged with HHAT pAPL on CAR signaling. (L–N) Dose-response curves (L), representative EC50s (M), and FC TCR/CAR (N) as a function of TCR antigenicity (1/EC50) for all 171 pAPL of the HHAT L8F neoantigen. (O) Average percentages of pAPL predicted to antagonize, enhance, or not affect CAR T cell activation.

We began by estimating, for a given TCR agonist (pAg), the prevalence of antagonists among altered peptide ligands (pAPL) generated by single amino acid mutations of pAg. This is particularly significant if pAg is a tumor neoantigen, i.e., a mutated self-antigen, because its set of pAPL would likely contain its potential self-counterpart (Figure 46A, left and center). We hypothesized that moderately strong agonists would have the highest chance of being derived from self-counterparts that are antagonistic to begin with (Figure 46A, right). To test this, we used a comprehensive mutagenesis dataset of three distinct human antigens associated with seven TCR clones [96]. We input the measured antigen strengths (EC50) for all TCR-antigen combinations (Figures 46B-D) into our mathematical model (Figure 46E) to derive predictions for FC TCR/CAR (Figures 46F and 46G). We then binned pAPL into three categories based on their predicted FC TCR/CAR: (1) antagonists (FC < 0.5), (2) null peptides ($0.5 <$ FC < 2), and (3) enhancers (FC > 2) (Figure 46H) and ordered TCRs by their agonist antigen EC50 (Figure 46I). We found that between 40% and 80% of pAPL across all three antigens are potentially antagonistic, with pAg agonists of intermediate strength producing the highest percentage of pAPL antagonists (Figure 46J). To further strengthen our analysis, we generated antigenicity data from a new tumor neoantigen derived from hedgehog acyltransferase (HHAT) and its specific TCR (Figure 46K). We measured the antigenicities (EC50s) for this HHAT pAg and its pAPL (Figures 46L and 46M) and passed them through our mathematical model to predict their corresponding FC TCR/CAR (Figure 46N). Accordingly, each antigen could be classified as an antagonist, null, or enhancer for CAR activation, and their probabilities to belong to each antigen class were largely consistent with the general trends observed with the literature-derived data (Figure 46O). In practice, our analyses suggested that TCRs with

high affinities to neoantigens and weak but non-zero affinities to their self-counterparts are frequently encountered when screening for neoantigen-specific TCRs, suggesting that the screening procedure for identifying "AEBS ready" TCRs would not be excessively difficult.

5.3.2 How often do issues of specificity affect logic-gated CAR T cells?

While our above analysis seemed to indicate that our prospects of finding the viable TCRs to implement our AEBS strategy were relatively high, it was also important to address the other side of the AEBS strategy: how difficult would it be to identify a CAR targets that would benefit from our AEBS approach to reducing off-target toxicity? To try to get a qualitative answer to this question, we turned to examining TCGA's matched tumor/tissue sample data, shown in Figure 47 below.

We selected 24 proteins currently known to be targets of CAR T cell clinical trials, and plotted their matched tissue vs tumor expression levels across the three cancer types in the database with greater than 100 patients. It is immediately apparent that the vast majority of CAR targets are expressed at roughly equal levels in the tumors and tissues of patients. Only a select few antigens namely CA9 and CD70, show significant overexpression in tumors compared to tissues across many patients, and CD70 only shows this differential in kidney tissue/tumors. There therefore clearly existed a need to improve specificity in common CAR targets. Our next step was to evaluate which among two common "logic gate" strategies to improving immunotherapeutic specificity, AND gates vs NOT gates, would be more effective given the patterns of expression shown above, as our AEBS strategy for improving specificity would work primarily through a NOT gate (TCR/CAR antagonism) based approach. Our computational protocol for comparing these two types of CAR design are described in Figure 48 below.

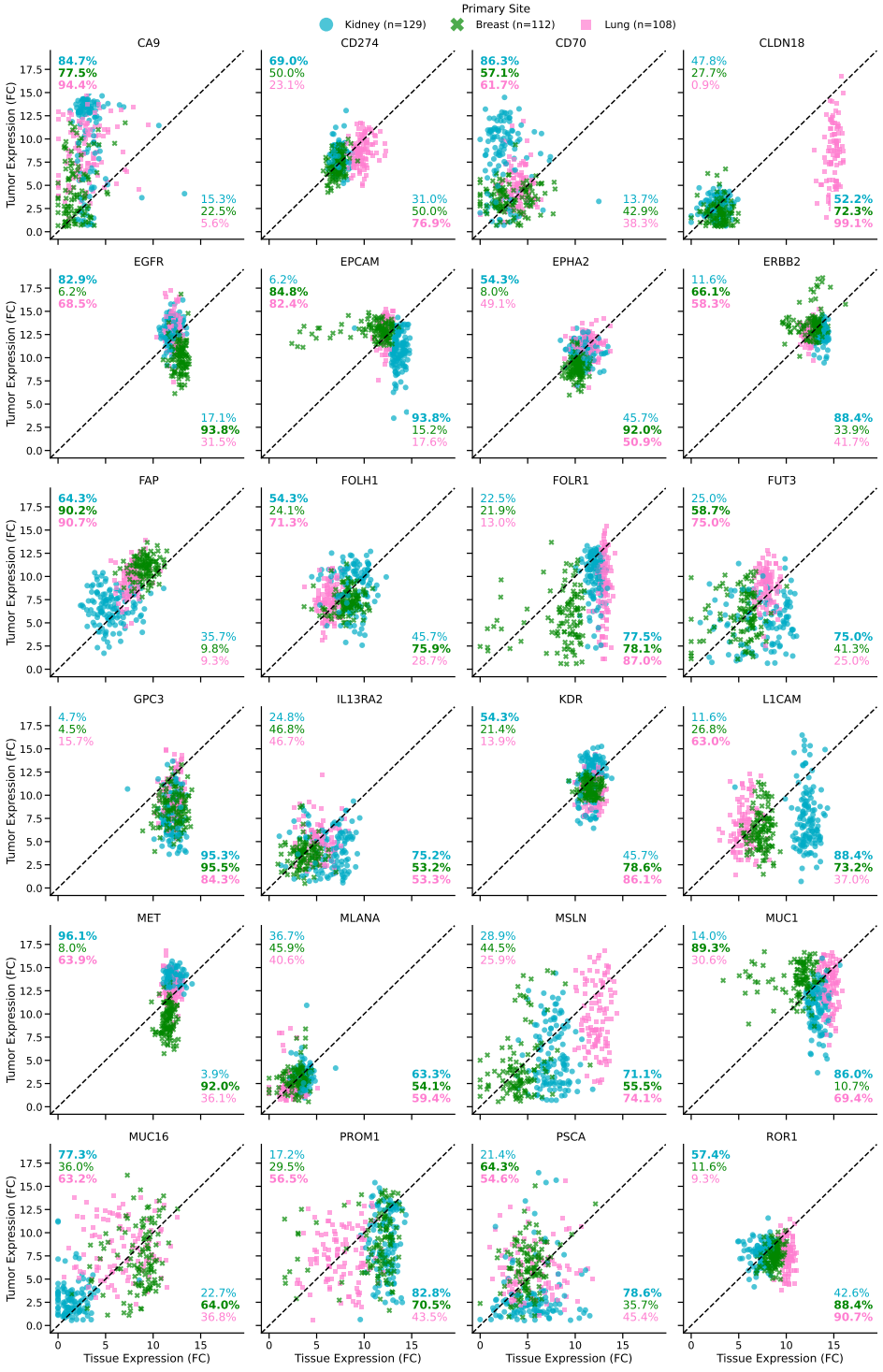

Figure 47: **Raw TCGA expression data for 24 CAR antigens across matched tumor/tissue samples.** Diagonal line represents equal tumor/tissue expression. Percentages in corners represent fraction of patients for a given cancer and antigen with tumor expression of the target antigen greater than tissue expression (top left) or tissue expression of the antigen greater than tumor expression (bottom right)

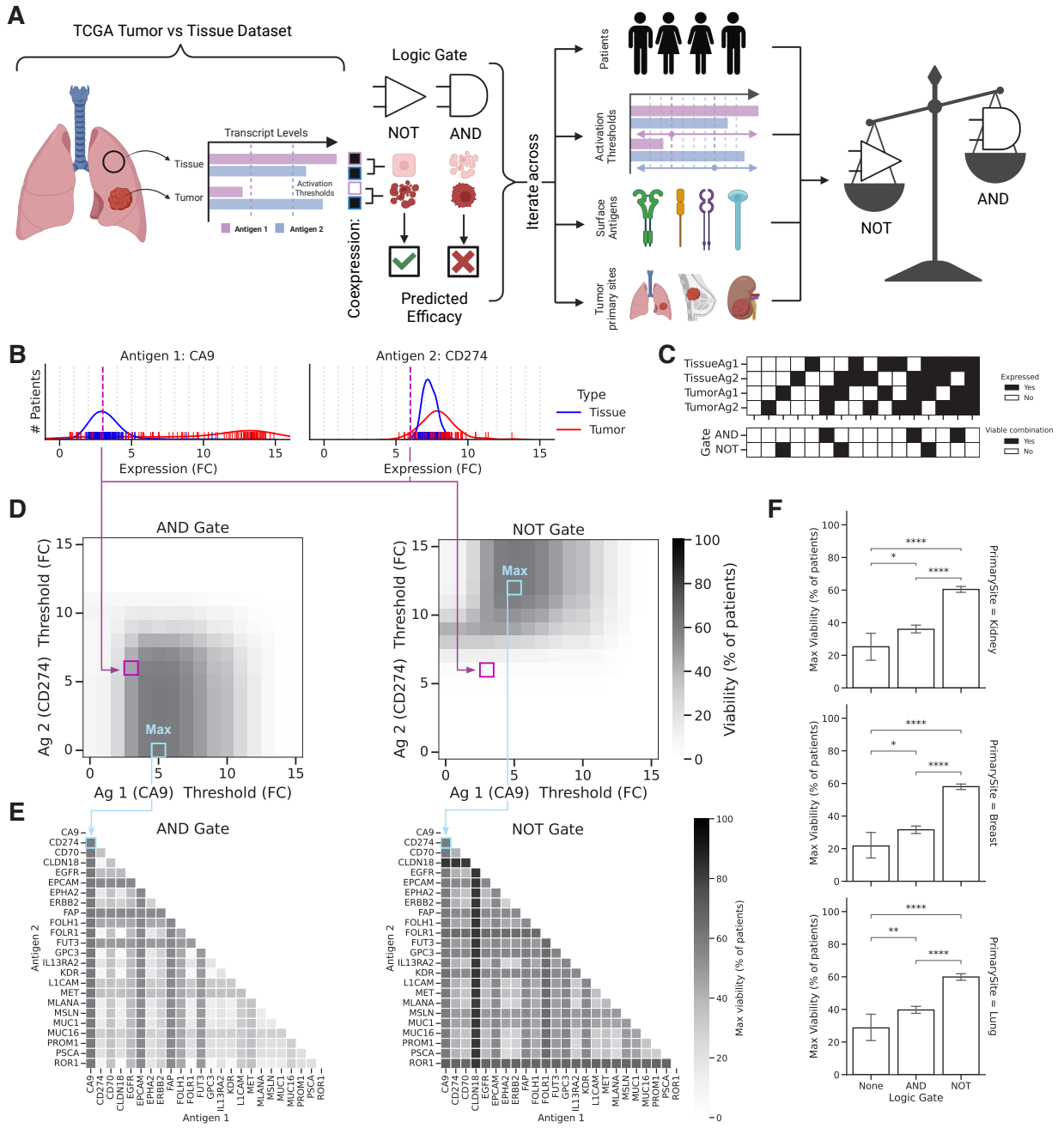

Figure 48: **Strategy for improving immunotherapeutic specificity using crosstalk** (A) Schematic of the computational pipeline to compare theoretical utilities of NOT vs AND logic gates in preventing on-target/off-tumor toxicity in patients with matched tissue/tumor antigen expression data from lung (n = 108), breast (n = 112), and kidney (n = 129) cancers. (B) Twenty antigen expression thresholds were defined independently for each antigen; target cells with antigen expressions to the right of a given threshold were assumed to be high enough to sufficiently activate CAR T cells. (C) Combinations of tumor and tissue activation patterns across two potential logic gate candidate antigens were translated into logic gate viability; T cell activation on healthy tissue or lack of T cell activation on a tumor were modeled as causing a theoretical treatment "failure".

Figure 48: *(continued)* (D) Percentage of patients with successful predicted treatments (therapeutic viability) for both AND (left) and NOT (right) logic gates at all pairwise combinations of antigen expression thresholds for the CA9 and CD274 antigens. Purple boxes indicate therapeutic viability at a representative combination of antigen expression thresholds. Light blue boxes represent maximum therapeutic viability for the given antigen pair across all expression thresholds. (E) Maximum predicted therapeutic viabilities for each pairwise antigen combination for AND (left) and NOT (right) logic gates. (F) Average maximum predicted patient success rates across all antigen pairs for kidney (top), breast (middle) and lung (bottom) cancers predict that NOT gates outperform AND gates. Data in (F) are shown as means ± 95% CI.

Figure 48A shows an outline of our comparison strategy. We first independently defined twenty antigen expression thresholds for each of the twenty four CAR target antigens described above (Figure 48B); target cells with antigen expressions to the right of a given threshold were assumed to be high enough to sufficiently activate CAR T cells. Figure 48C shows how combinations of tumor and tissue activation patterns across two potential logic gate candidate antigens were translated into logic gate viability; T cell activation on healthy tissue or lack of T cell activation on a tumor were modeled as causing a theoretical treatment "failure". Figure 48D displays the percentage of patients with successful predicted treatments (therapeutic viability) for both AND (left) and NOT (right) logic gates at all pairwise combinations of antigen expression thresholds for the CA9 and CD274 antigens. Purple boxes indicate therapeutic viability at a representative combination of antigen expression thresholds. Light blue boxes represent maximum therapeutic viability for the given antigen pair across all expression thresholds. Figure 48E depicts maximum predicted therapeutic viabilities for each pairwise antigen combination for AND (left) and NOT (right) logic gates. Figure 48F displays how average maximum predicted patient success rates across all antigen pairs for kidney (top), breast (middle) and lung (bottom) cancers all predict that NOT gates outperform AND gates, further substantiating our the strategy of using the inhibitory (NOT gate like) signal generated by TCR/CAR antagonism in an AEBS system to improve immunotherapeutic specificity.

5.4 Validating the AEBS strategy

5.4.1 Identifying and characterizing an AEBS ready TCR

Through the computational analyses described above, we had clearly demonstrated the viability of finding both an "AEBS ready" TCR and a CAR that could benefit from the fuzzy logic an AEBS TCR could provide. Our next step was to validate the AEBS design experimentally, which required us to first identify a TCR clone that had the correct level of self-antigen and tumor neoantigen reactivity to produce beneficial TCR/CAR crosstalk. After a careful literature search, we found a HLA-A0206 restricted TCR against L8F neoantigenic mutation of the hedgehog acyltransferase protein that seemed to fit the criteria we were looking for, as shown in Figure 49 below.

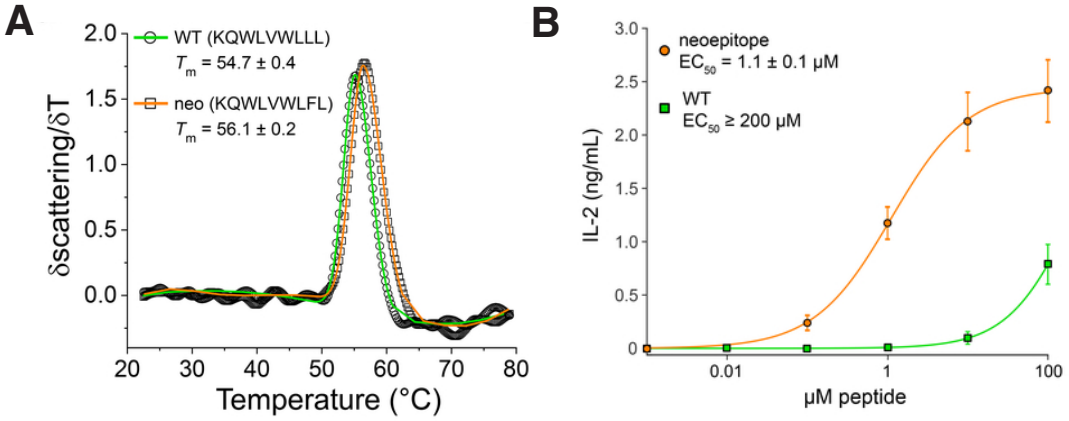

Figure 49: **HHAT AEBS selection, reproduced from [7]** (A) The thermal stabilities of the HHATL75 neoepitope and WT peptide–HLA-A*02:06 complexes are nearly identical and reflective of high-affinity peptide binding. T_m values are indicated in the inset and are the averages and standard deviations of six independent measurements. Representative scattering data are in black with only every 12th data point shown for clarity. Fits to the data are shown in orange (neoepitope) or green (WT). (B) The neoepitope is at least 200-fold more stimulatory than the WT peptide as assessed by cytokine release in coculture experiments. Data points and error bars are averages and standard deviations from three biological replicates in two independent experiments. EC50 values and, for the neoepitope, fitting error from simultaneous analysis of all data are shown. The EC50 for the WT peptide is a lower estimate.

Figure 49 displays the thermal stability of WT/neoantigen + MHC complexes. Their close similarity indicates that the two antigens bind equally well to their MHC. This is a critical feature for a AEBS compatible epitope, as dissimilar peptide/MHC stability could lead to low efficiency TCR/CAR crosstalk. Figure 49B shows that while the functional EC50s of the two epitopes are quite different, with the neoantigen eliciting much higher T cell activation, the self-antigen does

also produce a small level of T cell activation at the very highest peptide dose, exactly the type of weak self reactivity we were looking for.

Our next step in producing a prototype AEBS system was to identify a CAR against a ubiquitously expressed surface target to control with our HHAT specific TCR. We chose to use the HER2 CAR previously implicated in a clinical trial-halting adverse event caused by off-target toxicity against healthy lung tissue [97]. We then obtained the HHAT TCR and HER2.BBz CAR sequences and used them to construct prototype AEBS CAR T cells (Figure 50).

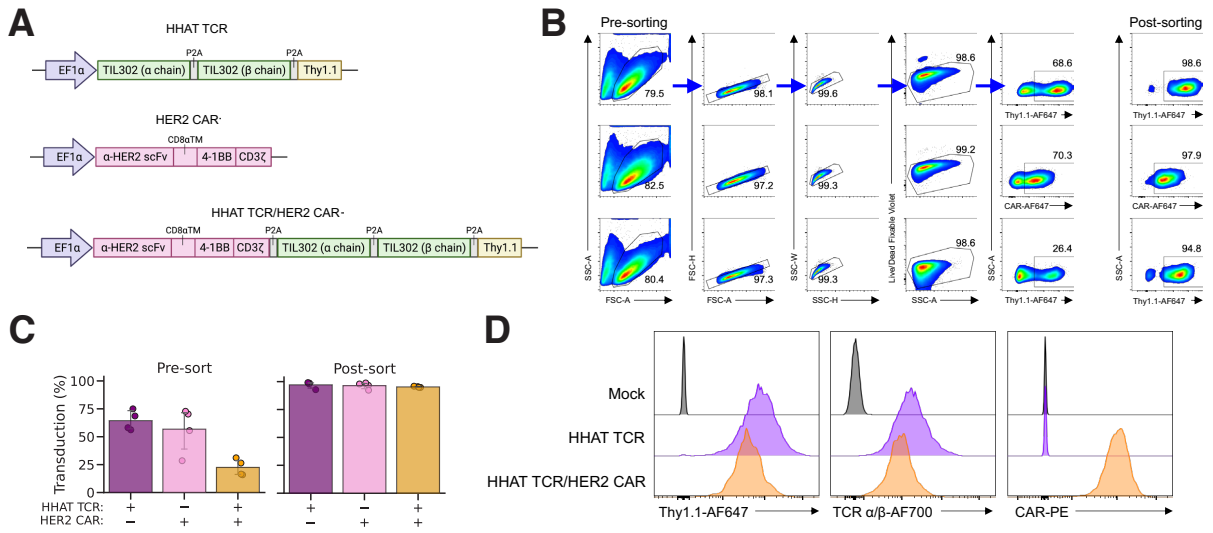

Figure 50: **HHAT AEBS construction** (A) Lentiviral vector designs for the expression of HHAT TCR T, HER2 CAR T, and HHAT/HER2 constructs and reporters CAR T (AEBS) cell production. (B) Gating strategy for the sorting of cells transduced with each vector introduced in (A) and representative plots of the final sorted cell products. (C) Pre- and post-sort transduction efficacies of the HHAT TCR T, HER2 CAR T, and HHAT TCR/HER2 CAR T cells. (D) Expression levels of Thy1.1, HHAT TCR, and HER2 CAR receptors in TCRb chain-deficient Jurkat (J.RT3-T3.5) cells.

We first cloned both the HHAT TCR (also called TIL302) α/β chains and HER2.BBz CAR sequences into single vectors under control of the Ef1a promoter, either in isolation (Figure 50A top/center) or in conjunction separated by a P2A sequence (Figure 50A bottom). We also appended Thy1.1 selection tags onto the ends of the TCR+ sequences to allow for efficient purification after transduction (the CAR was skipped because we already a CAR purifying antibody available). We then transduced human PBMCs with all three types of vector and sorted them with either with a Thy1.1 antibody (TCR and TCR/CAR transduced cells) or a Protein L antibody (CAR transduced

cells) (Figure 50B). This resulted in excellent post-sort purity (50C), and receptor expression levels (50D).

5.4.2 Testing AEBS CAR T cells *in vitro*

With our T cells generated, we could now proceed to validate our AEBS hypothesis. We started with a simple *in vitro* test of TCR/CAR crosstalk in these cells, described in Figure 51 below.

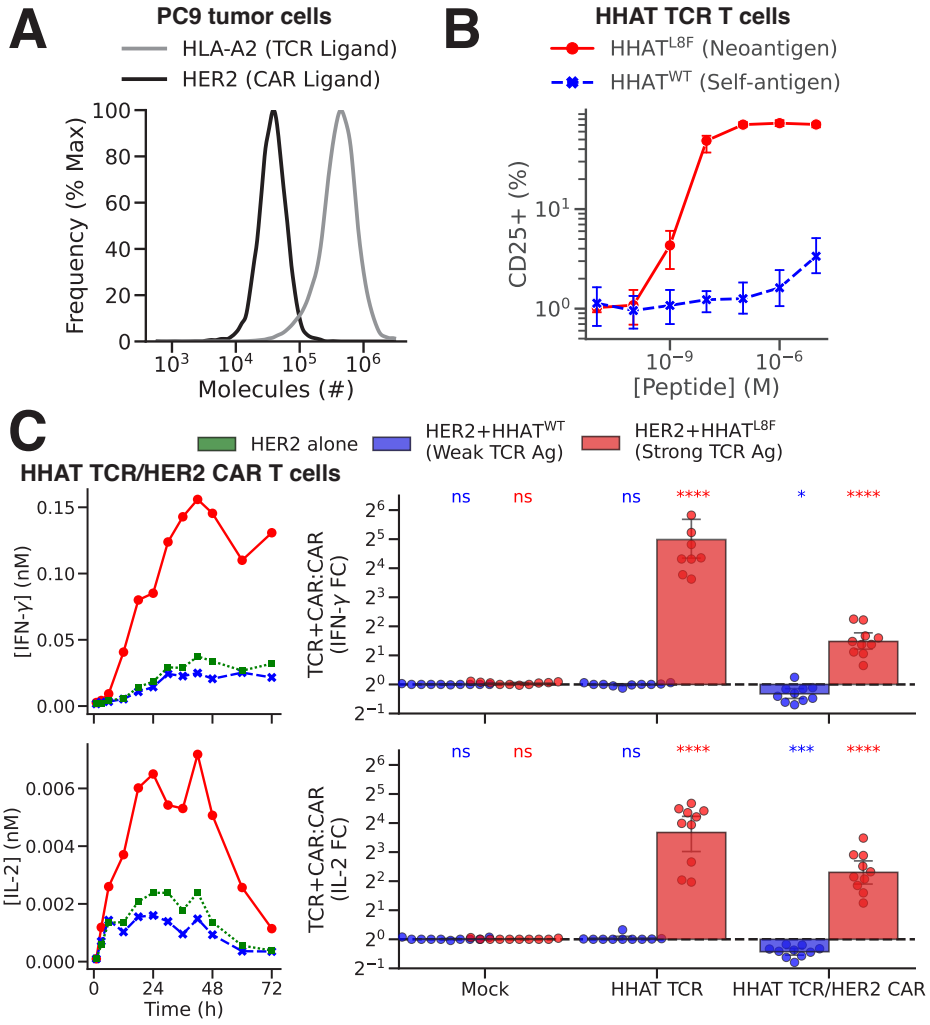

Figure 51: **HHAT AEBS validation** (A) Flow plots showing MHC and CAR ligand levels for PC9 tumor cells (B) Dose response curves of HHAT TCR T cells cocultured with PC9 tumor cells pulsed with self and neoantigenic versions of HHAT antigen (C) Representative cytokine secretion dynamics (left) and FCs in cytokine levels (right) of HHAT and HHAT/HER2 T cells in response to combinations of TCR and CAR signals of varied strengths (n = 10 biological replicates).

The antigen presenting cell we used for these tests was the HER2+/HLA-A0206+ lung adeno-

carcinoma PC9 cells, whose TCR and CAR ligand levels are given in Figure 51A. The levels of HLA in this cell type were much higher than its HER2 ligand levels, which represent the ideal case for antagonism (TCR ligand outnumbering CAR ligand). In addition, when the self-antigen HHAT-WT and the neoantigen HHAT-L8F were pulsed onto these cells at various concentrations and the peptide-laden APCs were coincubated with HHAT TCR+ cells, the resulting T cell activation dose response curves (measured by 24h CD25 levels) displayed the same low self-reactivity, high neoantigen-reactivity behavior we had originally seen in the literature (Figure 51B). We therefore proceeded to test TCR/CAR crosstalk *in vitro* by pulsing PC9 cells with high doses of either the self-antigen or tumor neoantigen, coculturing them with Mock, HHAT TCR+, and HHAT TCR/HER2 CAR+ T cells, then measured IFNg and IL-2 secretion kinetics using the IMMUNOtron (51C left). The data shows small but statistically significant decreases in both IFNg and IL-2 secretion resulting from TCR/CAR+ cocultures with PC9/HHAT-WT cells compared to their cocultures with unpulsed PC9 cells, as well as much larger increases in IFNg/IL-2 production resulting from TCR/CAR+ cocultures with PC9/HHAT-L8F cells compared to unpulsed PC9 cell cocultures (51C right), providing us with the first indication of the validity of the AEBS approach to improving immunotherapeutic specificity.

Emboldened by our initial success at validating the AEBS concept, we moved onto a more rigorous series of *in vitro* tests of the potential of AEBS therapy, shown in Figure 52 below.

In this battery of tests, we opted to use tissue and tumor cells to present the self-antigen and tumor neoantigen respectively, in order to make our test settings more clinically relevant. The tumor cells were the same PC9 lung adenocarcinoma cells we used previously, but the tissue cells were new BEAS-2B immortalized lung epithelial cells that we transduced to express HLA-A0201. The levels of TCR and CAR ligand (HLA-A2 and HER2 respectively) were quite similar between the two cell lines (Figure 33B right), with the tissue cell line expressing slightly higher HLA-A2 and slightly lower HER2 levels. We also reintroduced HER2 CAR+ T cells into these tests, giving us four T cell types (Figure 52A top) and four APC types (HHAT-WT/HHAT-L8F pulsed/unpulsed) (Figure 52A bottom) to survey for TCR/CAR crosstalk. Finally, we decided to examine both the cytotoxicity and cytokine production in this set of tests (Figure 52A center), and opted to use a kit that covered a larger set of cytokines than our initial validation tests. Based on the

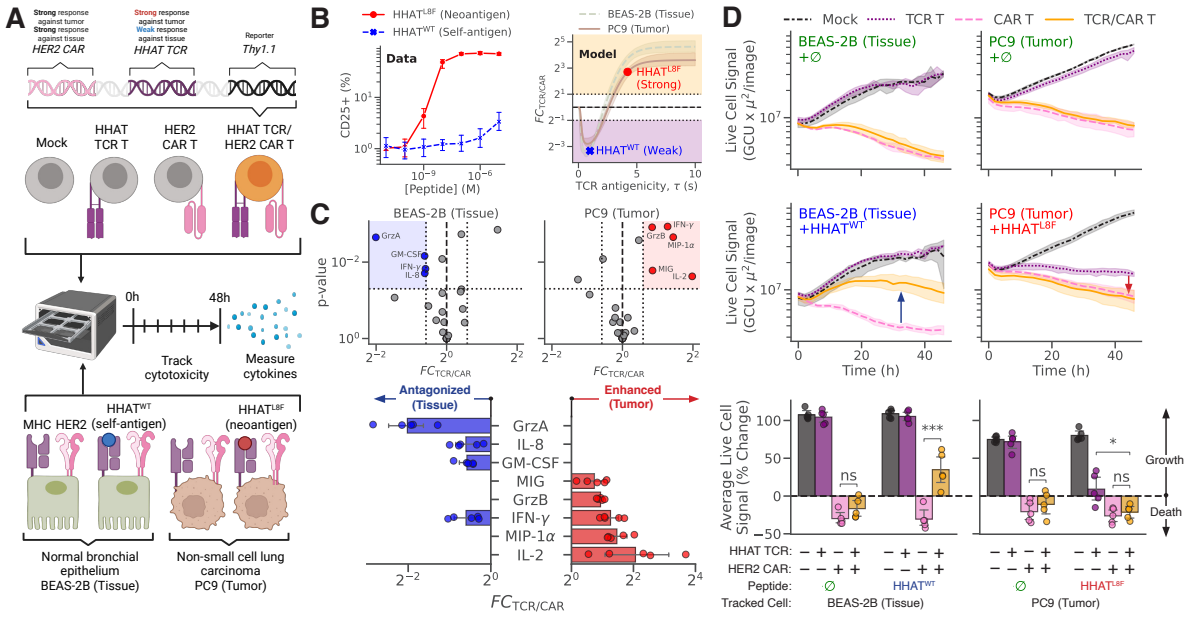

Figure 52: **HHAT AEBS *in vitro*** (A) Design of dual TCR/CAR T cells comprised of an anti-HHAT TCR and an anti-HER2 CAR (top) and experimental design (bottom). (B) Dose-response curves for HHAT TCR activation by self- (HHATWT) and neo- (HHATL8F) antigens (left, n = 3) and model predictions for TCR/CAR crosstalk (right). (C) Volcano plots (top) and FCs (bottom) of effector molecule secretion triggered by HER2 activation with/without HHATWT/HHATL8F TCR stimulation (n = 5). (D) Cell growth curves (top) and average growth over time (bottom) for target cells. Cytotoxicity of dual TCR/CAR T cells against healthy tissue compared with CAR T cells (upward arrow) and against tumors compared with TCR T cells (downward arrow, n = 5). Statistical differences in (C) were calculated using unpaired one-tailed Student's t-test. Statistical differences in (D) were calculated using an unpaired two-tailed Student's t-test. Data in (B, C, D) are shown as mean ± SD.

previously described dose response data in Figure 52B left, and the measured ligand numbers per APC type from Figure 33B right, our model predicted that we HHAT-WT pulsed BEAS-2B cells would produce significant antagonism, while HHAT-L8F pulsed PC9 cells would produce significant enhancement, of CAR T activation (Figure 52B right).

Our expanded cytokine quantification kit could measure the secretion of 27 different molecules. To identify cytokines that underwent significant changes in secretion upon different levels of TCR stimulation, we decided to construct volcano plots that measured the fold change of each cytokine's secretion in TCR/CAR+ cells cocultured with peptide pulsed vs unplused APCs on the x axis for each cell type, and set cutoffs of $2^{-0.5}$ and $2^{+0.5}$ for the antagonizing and enhancing fold change limits, as well as a p-value significance cutoff of 0.05 (after Holm-Bonferroni correction) (Figure 52C

top). This analysis returned four significantly antagonized molecules upon BEAS-2B/HHAT-WT stimulation and five significantly enhanced molecules upon PC9/HHAT-L8F stimulation (Figure 52C bottom). Two of the molecules, IFNg and IL-2, had been previously observed to be enhanced and antagonized in the smaller cytokine panel used in Figure 51 above, but the other seven molecules were new. The most striking observation was that Granzyme A levels underwent a dramatic (almost four fold) reduction in secretion upon weak TCR stimulation. Intriguingly, this cytokine was not enhanced after strong TCR stimulation, although its closely related and more well studied counterpart, Granzyme B, was.

This modulation of secreted granzyme levels after TCR stimulation increased our confidence TCR/CAR crosstalk would have an especially significant impact on direct cell killing. We therefore turned to directly examining the effects of differing levels of TCR stimulation on the cytotoxicity of CAR T cells through an incucyte assay, which measures the overall fluorescence of target cells in a well over a time course (in our case 48h). As only live cells produce enough intracellular green fluorescent protein (GFP) to be visible on the incucyte, the overall GFP fluorescence level in a well can be used to directly quantify the level of live target cell present in that well. Both our tumor and tissue target cells had been engineered to produce intracellular GFP, and were therefore amenable to use in this assay. Figure 52D middle demonstrates that when exposed to antigen pulsed target cells, AEBS CAR T cells exhibit a significant decrease in HHAT-WT expressing tissue cell killing compared to conventional CAR T cells, while simultaneously exhibiting a significant increase in HHAT-L8F neoantigen expressing tumor cell killing compared to TCR T cells alone (Figure 52D bottom left and bottom right respectively). These effects are not observed when the target cells are not pulsed with antigen (Figure 52D top); in those cases the CAR+ and TCR/CAR+ cells behave identically, proving that these effects are entirely TCR stimulation mediated. Of note, the effect size of antagonism on T cell cytoxicity is much larger than its previously observed effect on cytokine secretion, potentially due to the very significant decreases in Granzyme A production upon weak TCR stimulation described previously.

5.4.3 Accounting for heterozygous neoantigen mutations

The positive results we obtained with the rigorous battery of *in vitro* tests described above prompted us to embark on a series of experiments to test how well AEBS therapy could translate to true clinical settings. One important consideration for clinical translation we wanted to evaluate was how AEBS therapy would fare in tumors that were heterozygous for their neoantigen. Figure 53 below summarizes our approach.

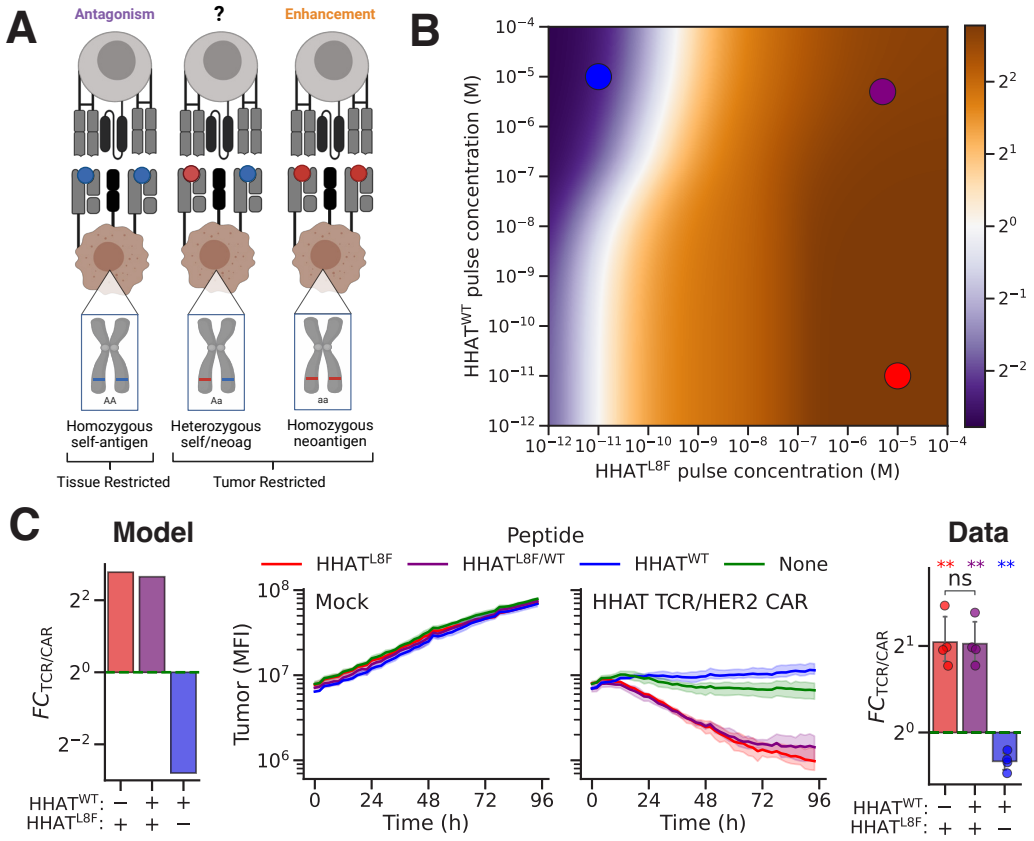

Figure 53: **Heterozygous neoantigens *in vitro*** (A) Heterozygous presentation of a self-antigen and a mutated neoantigen results in tumor cells that can simultaneously present both agonist and antagonist TCR ligands. (B) Model derived TCR/CAR fold change landscape as a function of neoantigen and self antigen densities (C) Model of the fold-change (FCTCR/CAR) of CAR activation with vs. without TCR activation (left). Experimental evaluation of activation by self/mutated antigen was assessed by measuring the killing of HER2+ tumor cells pulsed with HHATL8F, HHATWT, or a 1:1 mixture of both (right). The data confirmed the theoretical predictions from our model. HHATL8F/HHATWT heterozygous (1:1) tumors enhanced CAR activation to the same level as homozygous HHATL8F tumors, while HHATWT-homozygous cells (e.g., self-tissues) antagonized CAR activation. Data in (C) are shown as means ± 95% CI. Biological replicates were performed using T cells from different blood donors.

In heterozygous mutations of a tumor neoantigen, both the self-antigen and tumor neoantigen would be presented simultaneously, at roughly equal levels, on the surface of the target cell (Figure 53A). Because even a heterozygous mutation in a key tumor suppressor gene is often enough to initiate the cell's journey towards malignancy, and can often result in significant changes away from a "healthy cell" phenotype, we chose to only use PC9 tumor cells as the targets of this set of experiments. To gain an intuition as to how heterozygosity may affect TCR/CAR crosstalk, we first turned to our model, which we modified to be able to handle three types of antigen (two TCR ligands, one CAR ligand) simulatenously. We generated a landscape of the type and degree of TCR/CAR crosstalk expected across many combinations of HHAT-WT self antigen vs HHAT-L8F tumor neoantigen expression (Figure 53B), and examined the model's prediction for TCR/CAR crosstalk at three different scenarios: pure self-antigen homozygosity (blue), pure neoantigen-antigen homozygosity (red), and self/neoantigen heterozygosity (purple). Reassuringly, the model predicted that the TCR/CAR crosstalk would be practically unaffected by a heterozygous mutation in the tumor neoantigen. The 2 fold reduction in the level of a strong TCR ligand in neoantigen heterozygotes was not enough to decrease the level of enhancement observed, and the 1:1 mixture of enhancing neoantigen vs antagonizing self-antigen ligands present on the cell surface in these heterozygotes was also not nearly enough to produce antagonism (Figure 53C left). We tested this prediction by pulsing PC9 cells with a mixture of HHAT-WT and HHAT-L8F self and neoantigens to simulate heterozygosity before coculture with Mock or HHAT TCR/HER2 CAR AEBS T cells, then using an incucyte assay to quantify tumor cell killing (53C center). We saw no statistically signficant difference in tumor cell killing in the mixed neo/self antigen pulse condition compared to the pure neoantigen pulse condition (53C right), while observing significant antagonism of killing in the pure self antigen pulse condition, validating the model's predictions. These results indicate that neoantigen heterozygosity in tumors is not likely to cause issues in AEBS functionality.

5.4.4 Testing AEBS CAR T cells *in vivo*

The second set of tests we wanted to initiate to test the true clinical potential of AEBS therapy was to translate our *in vitro* experiments from Figure 52 into an *in vivo* form. To do so in a rigorous

fashion, we designed a new animal model for measuring on-target and off-target toxicity using human tissue and human tumor cells simultaneously. A basic outline of our protocol is described in Figure 54 below.

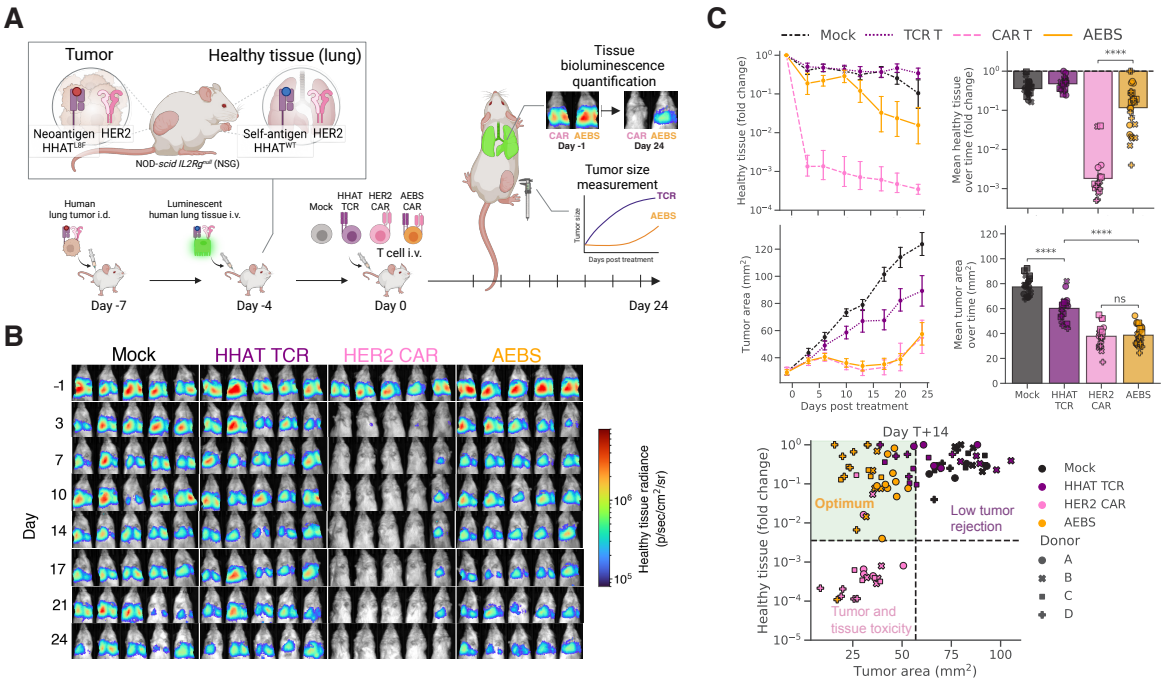

Figure 54: **HHAT AEBS *in vivo*** (A) *in vivo* humanized mouse model to simultaneously evaluate anti-tumor efficacy and OTOT activity of mock, TCR, CAR, and AEBS T cells. (B) Bioluminescent images of human lung tissue cell survival following T cell transfer. (C) Dynamics and time average of healthy tissue persistence and tumor growth (top). Profiles of tumor vs. healthy tissue are plotted at day 14 (bottom; n = 20–29 mice/group). Statistical differences in (C) were calculated using an unpaired two-tailed Student's t-test. Data in (C) are shown as mean ± SD.

Figure 54A displays the complex series of steps involved in creating this novel animal model. We first genetically engineer the PC9 tumor cell line and BEAS-2B tissue cell line to constitutively express the HHAT-L8F tumor neoantigen and HHAT-WT self antigen on their respective surfaces. We also engineer the luciferase enzyme into these BEAS-2B cells in order to allow for bioluminescence based measurements of tissue cell viability. We then conduct an intradermal injection of the HHAT-L8F expressing PC9 lung tumor into the flank of NSG mice, which have been bred to lack key components of their adaptive and innate immune system in order to prevent immune rejection of human tissue. Three days after introducing the tumor into the animals, we conduct an intravenous injection of the HHAT-WT/luciferase expressing BEAS-2B lung tissue. After injection,

these cells are flushed into the lungs of the animals, where they engraft themselves on top of healthy mouse lung tissue and can persist for up to 40 days without significant cell death in the absence of external treatment. Four days after tissue introduction, we treat the mice with an intravenous injection of either Mock, HHAT TCR+, HER2 CAR+, and HHAT TCR+/HER2 CAR+ AEBS T cells. Our innovative dual site approach allows us to quantify the degree of tumor vs healthy tissue killing upon after these immunotherapeutic treatments simultaneously, by using instruments such as the IVIS to measure the bioluminescence of the healthy human lung tissue over time while also using calipers to measure the physical size of the lung tumor on the flank of the mice over time. We measure both the tumor size and tissue bioluminescence in these mice twice a week for 24 days after treatment.

Figure 54B shows the raw data of the tissue quantification arm of the experiment, while Figure 54C top/center shows the quantified tissue and tumor data for the experiment. Strikingly, conventional HER2 CAR treatment almost completely wipes out healthy lung tissue present in the mice just three days after treatment; resulting in a >1000 fold reduction in healthy tissue cell levels over time compared to the day prior to treatment. Excitingly however, AEBS CAR T cells exhibit significantly (almost 100 fold) less off-target toxicity of these tissue cells compared to conventional CAR T cells, demonstrating the promise of using TCR mediated antagonism to control off-target toxicity in CAR T cells. In addition, as in the *in vitro* version of these experiments, AEBS CAR T cells exhbit improved tumor killing compared to conventional TCR T cells, though they again exhibit similar levels of tumor killing as conventional CAR T cells. The combination of these two advantages means that AEBS CAR T cells seem to represent an "optimal middle ground" between TCR T and CAR T cell immunotherapy, simultaneously exhibiting less off-target toxicity than CAR T cells and more on-tumor toxicity than TCR T cells (Figure 54C bottom).

5.5 Engineering a more clinically applicable AEBS CAR T cell

Despite our success testing the general idea of an AEBS CAR T cell *in vitro* and *in vivo* using HHAT TCR/HER2 CAR AEBS T cell + PC9/BEAS-2B target cell system, this approach suffers from several key limitations that would hamper its translation into the clinic, outlined in Figure 55 below.

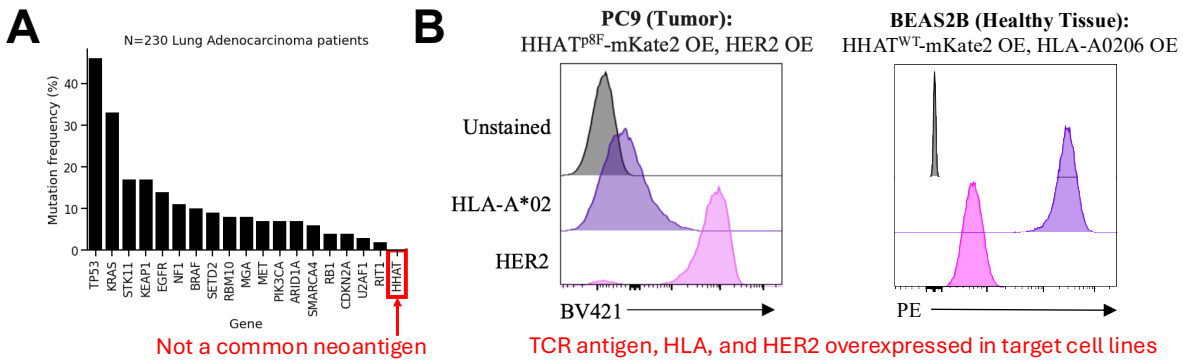

Figure 55: **HHAT AEBS limitations** (A) Mutation frequencies for all mutated genes found in multiple patients in [98] (B) Flow antigen expression levels for TCR and CAR antigens in cell lines used for *in vivo* HHAT AEBS experiment

Figure 55A displays the first prominent limitation of our system, which is that the HHAT L8F neoantigen is not found often in cancer patients, as it is not an oncogenic driver mutation, and the HLA the neoantigen is restricted to, HLA-A0206, is also not the most common HLA haplotype in the USA [99]. For example, in lung adenocarcinoma, the disease indication where HER2 CAR T cells had shown significant off-target toxicity previously [97], not a single patient in a reasonably large cohort [98] had a mutation in their HHAT gene, which indicates that it would be difficult to use an HHAT TCR-based AEBS to rescue HER2 CAR treatment of lung cancers in the clinic. Figure 55B illustrates the second limitation of the previous section's *in vivo* experiments in particular, which is that to make them work, we had to artificially express multiple CAR and TCR targets in our tumor and tissue cells of choice. While this is common practice in basic science papers, a rigorous test of the clinical viability of AEBS CAR T cells would require us to use target cell lines expressing endogenous levels of ligand.

5.5.1 Identifying and characterizing a clinically relevant AEBS ready TCR

We therefore decided to switch our TCR target to an antigen derived from a more commonly mutated protein in tumors. Our target selection strategy is outlined in Figure 56 below.

We started by examining a paper that had created a list of most commonly mutated genes in the TCGA [100] (Figure 56A). The tumor supressor gene TP53 was by far the most commonly mutated protein in this census, so our next step was to examine the frequencies of hotspot mutations of this

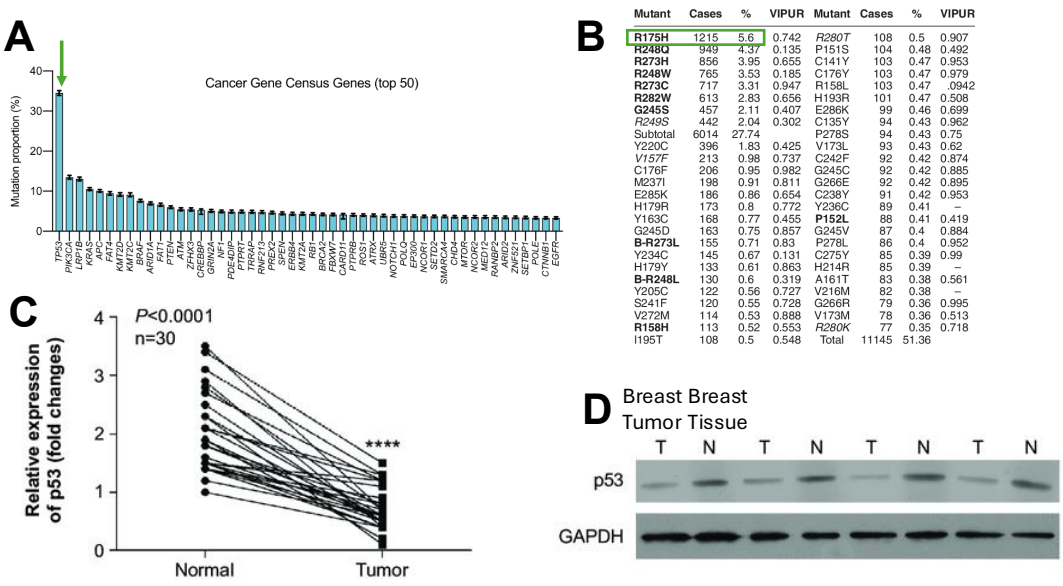

Mutant	Cases	%	VIPUR	Mutant	Cases	%	VIPUR
R175H	1215	5.6	0.742	*R280T*	108	0.5	0.907
R248Q	949	4.37	0.135	P151S	104	0.48	0.492
R273H	856	3.95	0.655	C141Y	103	0.47	0.953
R248W	765	3.53	0.185	C176Y	103	0.47	0.979
R273C	717	3.31	0.947	R158L	103	0.47	.0942
R282W	613	2.83	0.656	H193R	101	0.47	0.508
G245S	457	2.11	0.407	E286K	99	0.46	0.699
R249S	442	2.04	0.302	C135Y	94	0.43	0.962
Subtotal	6014	27.74		P278S	94	0.43	0.75
Y220C	396	1.83	0.425	V173L	93	0.43	0.62
V157F	213	0.98	0.737	C242F	92	0.42	0.874
C176F	206	0.95	0.982	G245C	92	0.42	0.885
M237I	198	0.91	0.811	G266E	92	0.42	0.895
E285K	186	0.86	0.654	C238Y	91	0.42	0.953
H179R	173	0.8	0.772	Y236C	89	0.41	–
Y163C	168	0.77	0.455	**P152L**	88	0.41	0.419
G245D	163	0.75	0.857	G245V	87	0.4	0.884
B-R273L	155	0.71	0.83	P278L	86	0.4	0.952
Y234C	145	0.67	0.131	C275Y	85	0.39	0.99
H179Y	133	0.61	0.863	H214R	85	0.39	–
B-R248L	130	0.6	0.319	A161T	83	0.38	0.561
Y205C	122	0.56	0.727	V216M	82	0.38	–
S241F	120	0.55	0.728	G266R	79	0.36	0.995
V272M	114	0.53	0.888	V173M	78	0.36	0.513
R158H	113	0.52	0.553	*R280K*	77	0.35	0.718
I195T	108	0.5	0.548	Total	11145	51.36	

Figure 56: **P53 AEBS rationale** (A) Pan cancer gene mutation frequency, adapted from [100] (B) P53 hotspot gene mutation frequency, adapted from [101] (C) Quantified and (D) raw matched tissue vs tumor WT P53 expression, adapted from [102]

gene, described in Figure 56B and [101]. R175H was the most commonly mutated hotspot mutation in this census, though it was followed closely behind by several other mutations. This antigen is also presented on HLA-A0201, which is by far the most common HLA haplotype in North America [99], and WT P53 is commonly present at much higher densities in tissue than in tumors, such as in the 30 breast cancer patients shown in Figure 56C and D.

We therefore sought to identify a P53-R175H specific TCR to use to create an AEBS CAR T cell with direct therapeutic potential. We contacted Dr. James Yang's laboratory in the National Cancer Institute's surgery branch and obtained a list of P53 R175H specific TCR clones isolated by his lab over the last several years. In this list, two candidates stood out from their dose responses as potentially matching the "strong tumor neoantigen reactivity, weak self reactivity" criterion we had previously outlined as being essential for an ideal AEBS TCR candidate in Figure 45: the AV6/BV11 and AV5/BV6 clones isolated from patient 4196A's TILs (originally identified in [103]). To evaluate which TCR clone would be a better fit for our purposes, we obtained retroviral vectors encoding the DNA sequences of those two clones, transduced them into healthy human PBMCs, then used these TCR T cells to conduct our own dose response assays against the P53-

R175H neoantigenic peptide and P53-WT self peptide pulsed onto a cell with relatively low levels of endogenous P53 expression (Nalm6), preventing an excessive background activation signal from developing. The results are shown in Figure 57 below.

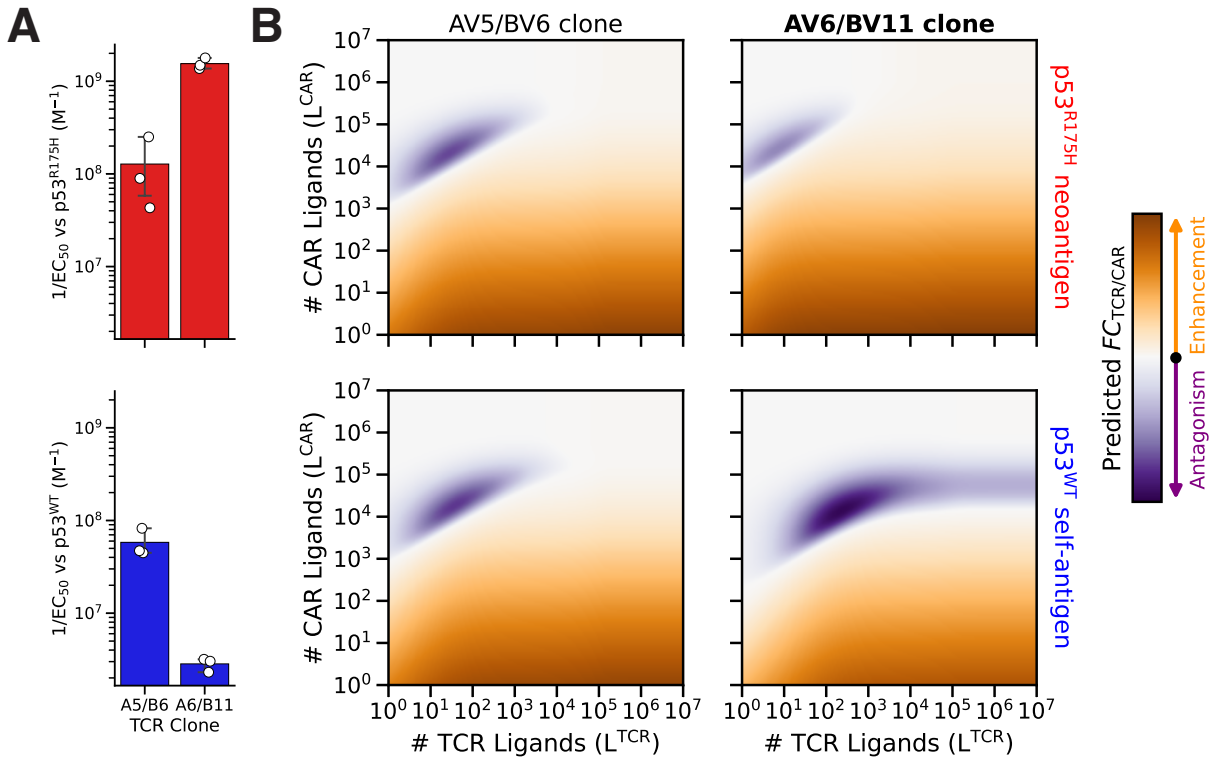

Figure 57: **p53 AEBS TCR Clone Comparison**

Figure 57A displays the EC50s for both TCR clones against WT and neoantigen peptides. The AV6/BV11 clone showed both higher reactivity against the tumor neoantigen and lower reactivity against the self-antigen than the AV5/BV6 clone, leading us to select this TCR for use in all further experiments to test the P53 AEBS system. The difference between the clones is especially stark when our model is used to generate a TCR/CAR crosstalk landscapes (model predictions for the degree and type of TCR/CAR crosstalk for different combinations of TCR and CAR ligand number) for both clones against both types of antigen (Figure 57B). While the AV5/BV6 clone shows essentially the same landscape for both the neoantigen and self-antigen, the AV6/BV11 clone we selected shows dramatically higher levels of antagonism against the self antigen than the neoantigen.

5.5.2 Measuring antigen levels on P53 AEBS target cell lines

With a potential P53-R175H specific TCR clone with beneficial TCR/CAR crosstalk properties in hand, we then turned to the task of identifying cell lines to use for our validation assays. We wanted to avoid having to express any antigens constitutively in the cells to keep our experimental settings as clinically relevant as possible. We therefore purchased and grew out a battery of cell lines expressing either P53-R175H or P53-WT with drastically different levels of endogenous CAR and TCR ligand (as measured by mass cytometry using the depmap tool described in [104]) in order to maximize our chances of observing TCR/CAR crosstalk in at least one of the target cell types. The characteristics of our cell line panel are described in Figure 58 below.

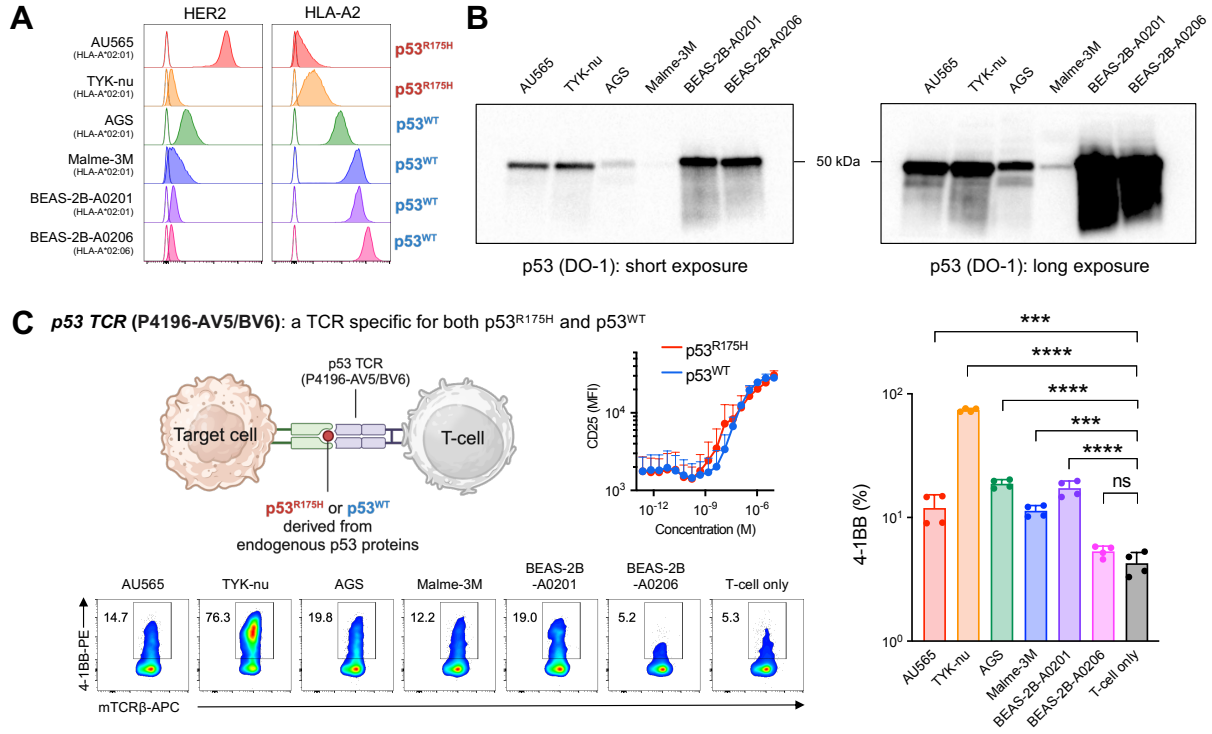

Figure 58: **p53 target cell lines** (A) Expression of HER2 and HLA-A2 on target cells. FMO (fluorescence minus one) control: unfilled; staining samples: filled. (B) p53 protein expression in target cells by immunoblotting. Both a short and a long exposure image are presented. (C) Detection of p53 antigens on-target cells with the P4196-AV5/BV6 TCR, which is equally specific for p53R175H and p53WT. Schematic of experimental design and EC50 for p53R175H and p53WT (top left). 4-1BB expression on 4196A TCR T cells by the co-cultured with these target cells (n = 4 biological replicates; top, bottom, and right). Statistical differences in (C) were calculated using a one-way ANOVA with Tukey's multiple comparison tests. Data in (C) are shown as means ± SD.

We first re-measured TCR and CAR ligand levels using flow cytometry in order to be able to compare them in a single experimental setting (Figure 58A). HLA-A2 levels ranged from very low (AU565) to very high (BEAS-2B), but CAR ligand levels were more uniformly low (with the exception of the AU565 cell line, which expressed very high levels of HER2). Next, we measured total levels of P53 protein in whole cell lysates prepared from each cell line. (Figure 58B). Upon long exposure, we could clearly see some P53 protein expressed intracellularly in all cell lines of interest. However in order to gauge how much of this total protein was actually presented on the surface of our cell lines, the more relevant parameter for assessing potential TCR activation against each cell line, we had to opt for a more unconventional approach (Figure 58C). Our key insight was to use the previously discarded P53 clone AV5/BV6, which recognized WT and R175H P53 antigens at nearly equal levels, as a "presented P53 antigen sensor". By comparing the activation induced by each target cell line in T cells transduced with this TCR, we could obtain a rough proxy for levels of either P53 antigen presented the surface of each cell. Figure 58C right shows the final results; all cell lines except BEAS-2B/A0206 show at least some increase in activation (in terms of 24h post co-culture 4-1BB+ frequency) compared to a T cell only control, with TYK-nu cells displaying the highest increase. The fact that BEAS-2B/A0206 did not display an increase in activation was especially promising, as this cell line was meant to serve as a negative control for antigen presentation (as it had been transduced with a mismatched HLA-A0206 allele for the HLA-A0201 restricted P53 antigens we were interested in).

5.5.3 Testing p53-TCR/HER2-CAR AEBS strategy across cell lines

The combination of observing at least some expression of CAR antigen, HLA, and presented TCR antigen on all cell lines (except for the negative TCR ag control BEAS-2B/A0206 cell line) prompted us to proceed with testing all six cell lines for TCR/CAR antagonism. We began by constructing P53 TCR/HER2 CAR AEBS T cells, a process described in Figure 59 below.

In this manufacturing process, we returned to the dual vector transduction approach in order to skip the wait time associated with cloning new monocistrionic TCR/CAR vectors. We manufactured six types of T cells in total; Mock transduced cells, p53 TCR transduced cells, HER2.28z and HER2.BBz CAR transduced cells, p53 TCR/HER2.28z AEBS CAR T cells, and

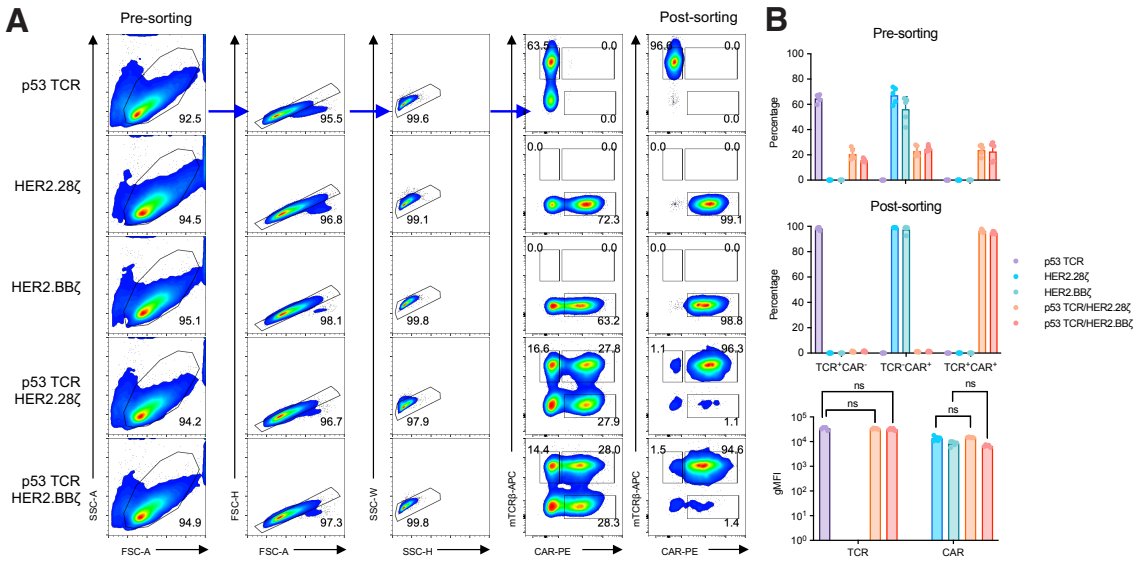

Figure 59: **p53 AEBS construction** (A) Gating strategy for sorting T cells transduced with viral vectors of either p53 TCR or HER2 CAR, both p53 TCR and HER2 CAR. (B) Percentage (top) of TCR+, CAR+, or TCR+CAR+ cells on pre- or post-sorting. Level (bottom) of TCR and CAR across all T cell lines (n = 5 biological replicates). Statistical differences in (B) were calculated using a one-way ANOVA with Tukey's multiple comparison tests. Data in (B) are shown as means ± SD.

p53 TCR/HER2.BBz CAR T cells. One significant difference compared to previous dual transduction approaches is that the plasmid for the P53 TCR was encapsulated in a retroviral vector, while the HER2 CAR used the same lentiviral vector we had used earlier. Besides minor tweaks to the protocol to accommodate this difference in viral delivery vehicle, the manufacturing and expansion process was otherwise very similar to what has been described previously. Interestingly, we were again able to use a generic mouse TCR β antibody to sort TCR+ cells (in addition to Protein L-biotin + PE-streptavidin antibodies to sort CAR+ cells) (Figure 59A) due to the same "murinization" process employed with the NYESO receptor we had used previously. Post sort purities were quite high across all cell populations (Figure 59B top/center), and levels of TCR and CAR expression were very similar across sorted populations (Figure 59B bottom), implying that TCR expression does not impact CAR expression and vice versa.

With both target cell lines and T cells in hand, we were able to begin setting up a large series of cytotoxicity assays to validate this more clinically relevant form of an AEBS CAR T cell, as described in Figure 60 below.

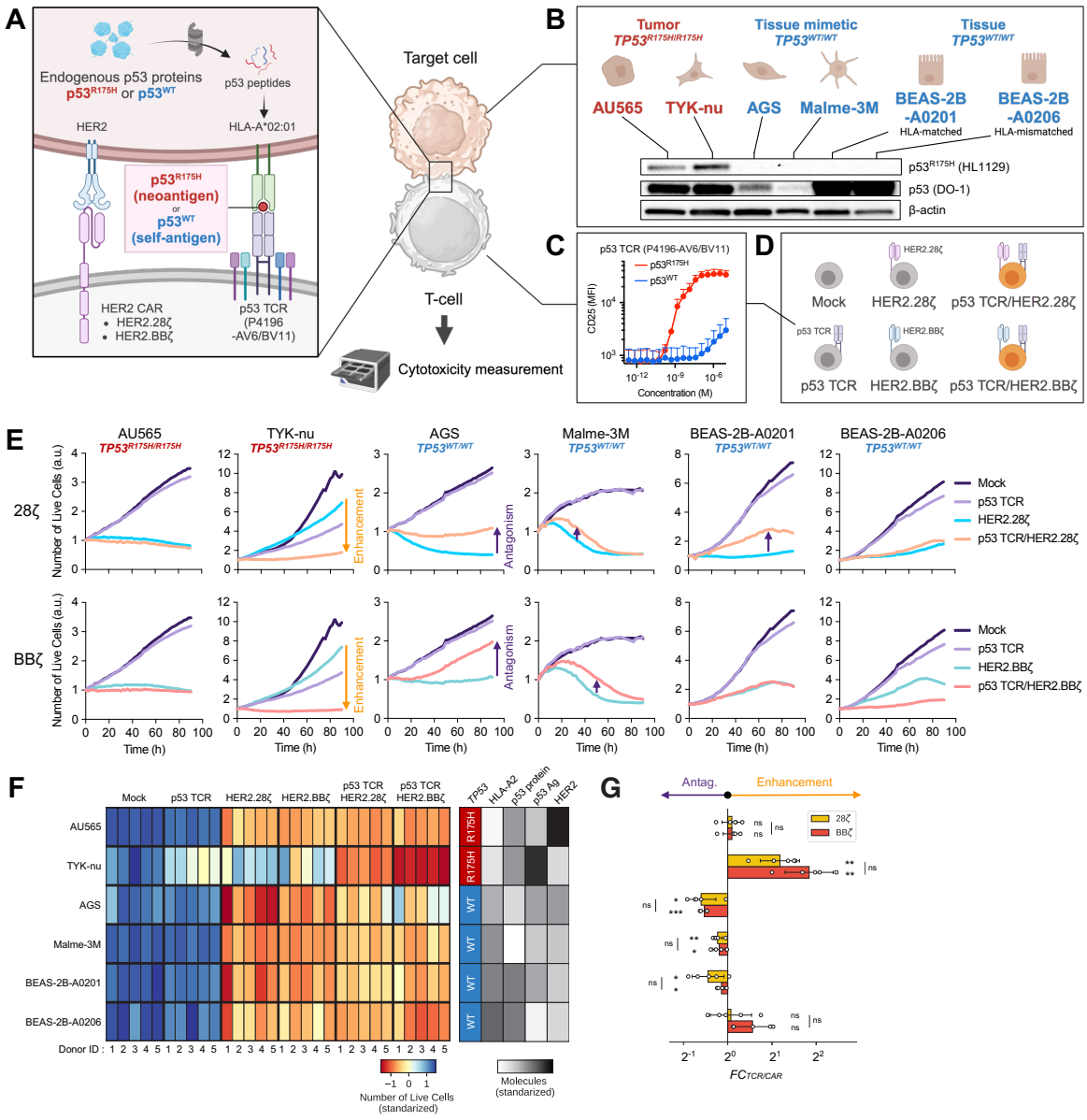

Figure 60: **p53 AEBS *in vitro*** (A) AEBS system combining an anti-HER2 CAR and an anti-p53 TCR. (B) Panel of target human cells. HER2+ target tumor cells, tissue mimetic, and tissue cells (top). Immunoblot analyses of endogenous mutant p53R175H and p53WT levels (bottom). (C) Dose-response curves of anti-p53 TCR against tumor cells presenting neo- (p53R175H) vs. self- (p53WT) antigens (n = 4). (D) Schematic of single and dual receptor T cells. (E) Representative cell growth curves of six target cell lines following co-culture with TCR, CAR, and TCR/CAR T cells. Mock and TCR T cell data were duplicated across both rows of each panel. (F) Heatmaps showing standardized killing activities for each T cell construct and target cell line (left) as a function of the respective p53, HLA-A, and HER2 abundances (right). (G) FC TCR/CAR for 28z- and BBz-based AEBS CAR constructs (n = 5). Data in (E, F, G) are pooled from four sets of experiments. Statistics in (G) were calculated using two-tailed paired Student's t-test as TCR/CAR vs. CAR. Data in (C, F) are shown as mean ± SD.

Figure 60A displays the high level overview of our approach, while Figure 60B shows the total P53 and R175H P53 present in each target cell line used in the study. Figure 60C displays the dose response curve of the P53 TCR we ended up selecting for these experiments; the weak self reactivity +strong neoantigen reactivity of this TCR is readily apparent here. Figure 60D shows a summary of the T cell types generated for these experiments.

Figure 60E shows the results of these parallel incucyte assays against every combination of target cell type and T cell type we had available. While each cell type seems to display a fairly diverse range of cytotoxicities, we can observe clear evidence of both antagonizing and enhancing behavior at endogenous ligand levels with the AGS and TYK-nu cell lines in particular. In addition, we can see truly synergistic interactions between the TCR and the CAR in TYK-nu's case, as the AEBS CAR cell kills the tumors better than any either monotherapy alone.

Cytotoxicity results across donors are visualized in the heatmap in Figure 60F, and the FC TCR/CARs for each cell line across CAR costim domains (calculated by dividing the AEBS T cytotoxicity by the CAR T cytotoxicity for a given costim domain+target cell line+donor) is summarized in the bar graph in Figure 60G; significances are computed relative to no change (FC=1). Except for AU565, where the TCR seems to have no apparent effect on the activation of the CAR, all other cell lines seem to show statistically significant enhancement (if P53 R175H is presented on the target cell) or antagonism (if P53 WT is presented on the target cell line), with the exception of BEAS2B-A0206, which has a mismatched HLA for binding the P53 antigens of interest and therefore was expected to not be affected by TCR stimulation. There also were no significant differences in FC TCR/CAR between costimulatory domains in any of the target cell lines.

5.5.4 Reconciling cell line to cell line variability

Our final task was to understand what could be driving variations in FC TCR/CAR across target cell lines, as without a mechanism that accounted for this type of dramatic variability, it would be difficult to predict how a given patient could respond to a clinical application of AEBS CAR T cell treatment. Our attempts at reconciling this variability are described in Figure 61 below.

We first attempted to plot different measured characteristics of target cell lines against their

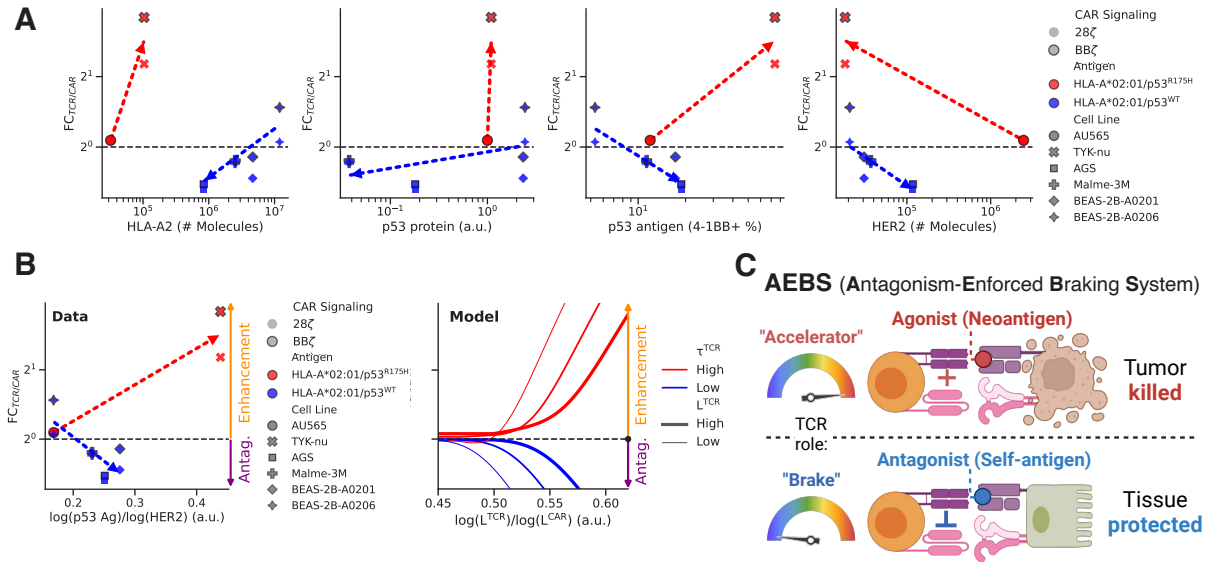

Figure 61: **Understanding drivers of p53 AEBS variability across cell lines** (A) TCR/CAR FC vs. readout level correlations for HLA-A2 density, total p53 density, P4196-AV5/BV6 activation, and HER2 density across all target tumor and T cell lines. (B) FC TCR/CAR as a function of the ratios of TCR to CAR ligand densities across target cell lines for TCR ligand density:CAR ligand density metric (left). Corresponding model output curves (right) demonstrating the bidirectional influence of TCRs on CARs. (C) General concept of AEBS.

TCR/CAR FC values (Figure 61A). HLA-A2 levels, total P53 levels, and HER2 levels all did quite poorly at explaining the difference in FC TCR/CAR across cell lines. Plotting FC TCR/CAR against presented p53 antigen levels seemed to produce a graph that more accurately explained the variation across cell lines per antigen type, but not universally. However, when we normalized CAR ligand levels by TCR ligand levels on the surface of target cells (essentially computing the "agonist:antagonist ratio" in a similar way to prior publications such as [56]) and plotted these values against the FC TCR/CAR observed with each cell line both using experimental values (Figure 61B left) and model predictions (Figure 61B right), we were able to explain essentially all variability in TCR/CAR crosstalk between cell lines. Cell lines with far more agonist (CAR) ligands than antagonist (TCR) ligands could not be affected by TCR/CAR crosstalk, but increasing this ratio allowed for greater levels of crosstalk to be observed (either inhibitory for P53 WT expressing cell lines or enhancing for P53 R175H expressing cell lines). This rescaling revealed the bidirectional nature of TCR/CAR crosstalk across cell lines, strongly validating the overall concept of "TCR-controlled fuzzy logic" fundamental to the AEBS platform (Figure 61C).

6 Discussion

6.1 Summary of results

Gaining a quantitative understanding of signal integration in T cells has become a particularly important area of research in recent years, due to the advent of increasingly complex methods of programming diverse types of T cell behavior in different contexts. The work presented in this thesis represents a significant advance in this field on multiple levels. **Chapter 2** describes the design and operation of the fully functional IMMUNOtron robotic platform, control software, and associated data analysis pipeline to collect, process, and analyze high throughput measurements of T cell activation. **Chapter 3** displays how this platform can be applied to uncover unique quantitative insights into TCR/CAR crosstalk in mouse CAR T cells, such as that weak TCR signaling can inhibit CAR T cell activation, and how collecting such quantitative data can allow for the development of highly predictive biological models of immune function. This chapter also shows how these results and the associated model predictions were robust enough to be recapitulated in rigorous *in vivo* experiments, despite small *in vitro* effects, helping demonstrate the value of the IMMUNOtron platform. **Chapter 4** describes how these results can be translated into human CAR T cells, and provides hints towards discovering the exact molecular mechanism behind TCR/CAR crosstalk. **Chapter 5** harnesses the insight gained into the exact nature of TCR/CAR inter-receptor communication to engineer a novel form of cancer immunotherapy named **A**ntagonism **E**nforced **B**raking **s**ystem (AEBS) CAR T cells that exhibit less off-target toxicity and greater on-tumor toxicity than conventional immunotherapies. In doing so, it also provides a roadmap for future studies to engineer complex logic into T cells with minimal numbers of additional receptors.

6.2 Advancing high throughput immunology

Immune responses have been referred to as a highly complex "liquid brain" of individual cells and their corresponding interactions [105]. The development of next generation automation tools such as the IMMUNOtron described in **Chapter 2** lets us produce enough data to use more advanced analysis techniques, like machine learning, to take an unbiased approach to gleaning the fundamental and "simple" organizing principles underlying the immune system. However,

to fully take advantage of the power of machine learning, even more data, beyond what can be generated using bulk cell measurements, needs to be collected. We have expended considerable effort reprogramming the IMMUNOtron to move beyond bulk cell measurement of immune cell function (such as the cytokines utilized in this work) and towards single cell data, and are just beginning to see tangible results, as shown in Figure 62 below.

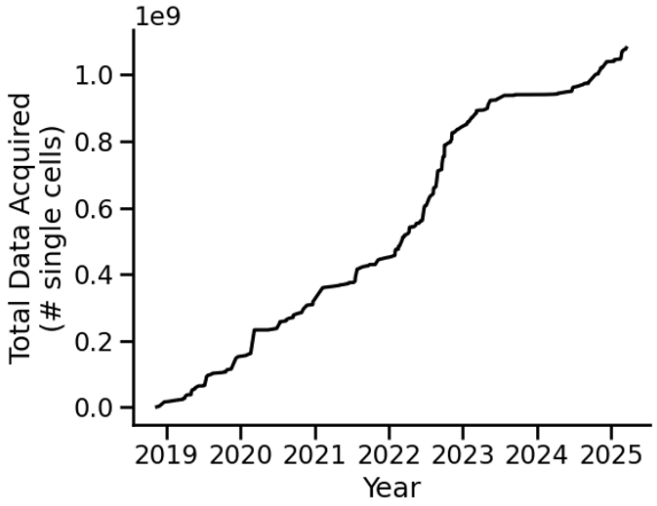

Figure 62: **IMMUNOtron single cell data generation over time**

In addition, a key improvement of robotic platforms such as the IMMUNOtron is the addition of a kinetic component to the frequently static way in which we view immune responses. By simplifying the timepoint collection process through its intuitive and flexible programming interface, the IMMUNOtron enables us to study of how immune responses evolve over time, providing us with much more complete picture on immune cell behavior. This has led the platform to have a tremendous impact across a diverse range of applications, ranging from oncology-focused clinical trials [106] to COVID-19 [107]. A simple example of why studying immune response over time is valuable is shown in Figure 63 below.

Figure 63A shows the value of kinetic data in an artificial system, where measuring IL-2 secretion over time allows us to calculate a much more robust measure of the level of T cell activation at different strength antigens than using any individual timepoint, due to the differing rates of IL-2 consumption between the antigens. Figure 63B displays the value of kinetic data in a translational context, as TCR-T cells derived from two potential candidates for immunotherapy produce IL-

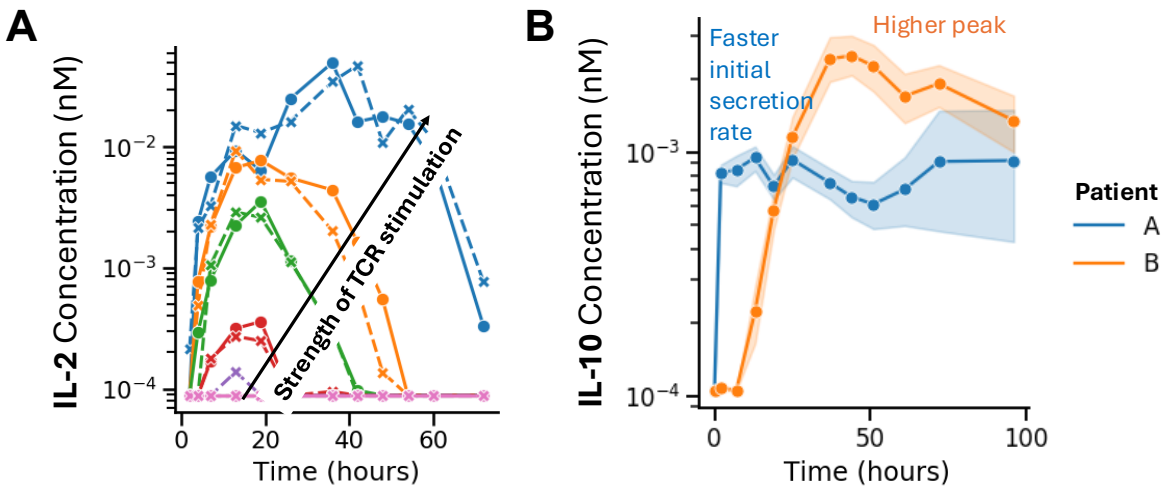

Figure 63: **Value of collecting data on the immune response over time** (A) IMMUNOtron collected measurements of IL-2 secretion over time of OT-1 T cells cocultured with B6 splenocytes pulsed with different affinity SIINFEKL APLs (B) IMMUNOtron collected measurements of IL-10 secretion over time of two different sets of patient derived NYESO TCR+ T cells cocultured with NYESO antigen positive SK-MEL-37 tumor cells

10 responses that differ drastically in their dynamics when responding to a tumor. A simple endpoint measurement of cytokine production would fail to capture the variability inherent in these immunotherapeutic responses.

Our hope is that future researchers will be able to leverage the unique features of the IMMUNOtron to untangle the heterogeneity of the dynamics of the immune response at a single cell level, in order to gain unique insight into the fundamental principles underlying the immune system. We present an example of this type of IMMUNOtron assisted analysis in the following section.

6.3 Unifying principles of antagonism

In this work, the large volume of TCR/TCR and TCR/CAR data we used the IMMUNOtron to obtain in **Chapter 3** was fully described by a single basic model structure, which is a simpler form of the more complex AKPR structure first developed in [34]. A key prediction of the original AKPR model is that the best antagonists are partial agonists. Does that prediction hold true in our recent datasets? To answer that question, we conducted a comprehensive analysis of how single receptor TCR and CAR stimulation data related to joint receptor stimulation data, detailed in Figure 64 below.

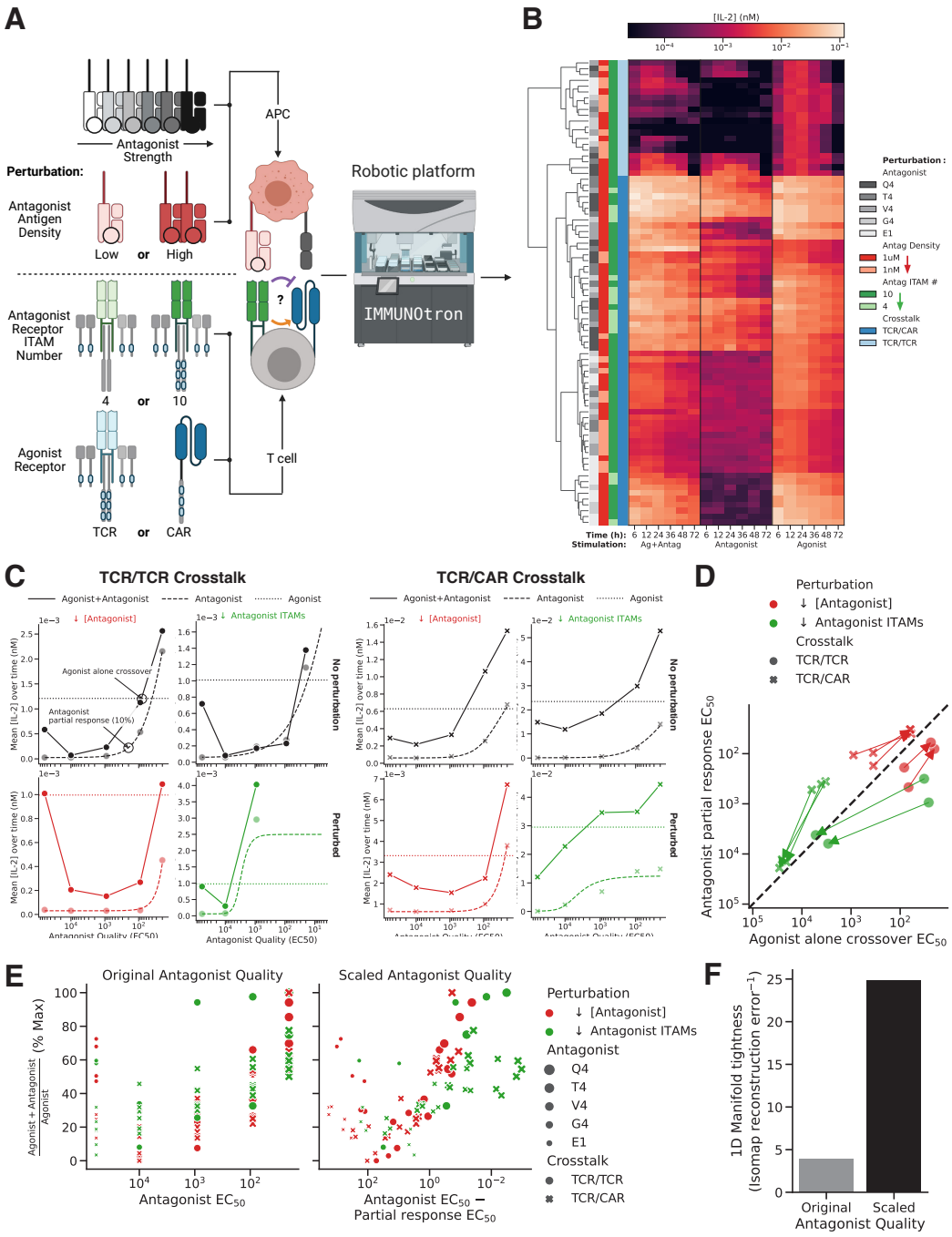

Figure 64: **Unified Antagonism.** (A) Schematic of molecular perturbations for CAR T cells applied and analyzed with robotic platform (B) Dataset of all cell activation measurements collected in response to dual TCR/CAR ligand stimulation (C) Combined, antagonist only, and agonist only response curves for various molecular perturbations. (D) Correlation between agonist alone crossover and partial response point. "Agonist crossover EC50": quality of antigen where the agonist response was equal to the "agonist+antagonist" response.

Figure 64: *(continued)* "Antagonist partial response EC50": quality of antigen on the antagonist curve where a minimal (10% above baseline) response was first achieved. (E) Unscaled and scaled versions of antagonist quality plotted against agonist/antagonist ratios. (F) Inverse isomap reconstruction error, which measures the tightness of the 1D manifold with scaled and unscaled antagonist qualities.

We first concatenated cytokine secretion data from cultures of mouse OT-1 T cells and OT-1 anti-CD19 CAR T cells, upon activation with a set of altered peptide ligands as well as CD19, both individually and in conjunction. We also added data from these T cells in different molecular configurations: by modulating antagonist ligand density or by changing the number of ITAMs on the antagonist receptor (TCR), as detailed in Fig. 64A. This resulted in a large matrix of data quantitatively documenting the activation of T cells in response to single or dual ligand stimulations, across a wide range of antigen qualities (Fig. 64B). We then proceeded to plot the agonist, antagonist, and agonist+antagonist curves against one another for each molecular perturbation (Fig. 64C) and observed that any shift in the "antagonist alone" curve were reflected by shifts in the corresponding "agonist+antagonist" curve. To formalize this observation, we recorded two metrics summarizing key features of all three curves: the "agonist crossover EC50" and the "antagonist partial response EC50" (Fig. 64D); these two quantities correlated well with each other. Moreover, scaling the antigen quality of antagonists (Fig. 64E, left) by the "antagonist partial response EC50", resulted in more unified curve of "agonist+antagonist" responses (Fig. 64E, right) with a higher 1D tightness (Fig. 64F). These correlations suggest that perturbing the response strength to "antagonists alone" is reflected in the "agonist+antagonist" response, and therefore further reinforces the prediction that the most antagonizing ligands are those closest to "the threshold needed for full signaling" [34]. Future theoretical work should aim to reproduce this unifying theory and uncover the exact molecular mechanisms driving its validity.

6.4 Limitations of AEBS CAR T cells

Despite the efficacy of the AEBS strategy we developed to improve immunotherapy in **Chapter 5**, there still remains significant room for improvement in the system, which may be required to drive the therapy forward towards clinical applications. One key limitation is described in Figure

65 below.

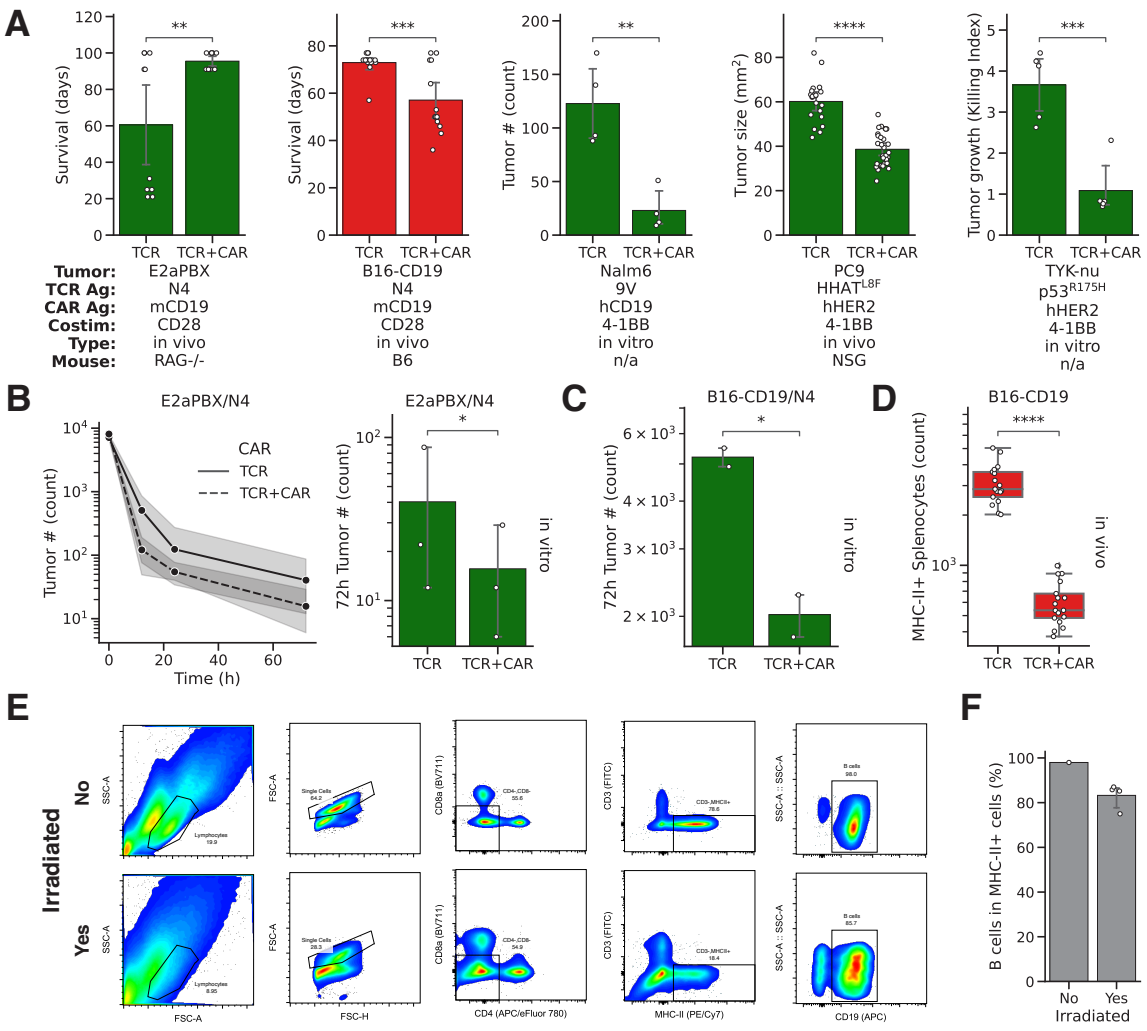

Figure 65: **Homing Limitation** (A) Comparison of anti-tumor cytotoxicity between TCR-only and TCR/CAR T-cells across different experimental models. In four out of five *in vitro* or *in vivo* models, TCR/CAR T-cells outperformed TCR-only cells, with TCR-only cells showing superior performance only in the B16-CD19 model (shown in red). (B) Time kinetics (left) and 72h summary (right) of tumor cell numbers over time in an *in vitro* test of E2aPBX/N4 tumor killing. (C) 72h summary of tumor cell numbers in an *in vitro* test of B16-CD19/N4 tumor killing. (D) CD45.1+/CD4-/CD8-/MHC-II+ splenocyte numbers decline drastically in all TCR+CAR treated conditions, potentially due to on-target/off-tumor toxicity. (E) Gating strategy for phenotyping splenocytes in unirradiated (top) and irradiated (bottom) B6 mice at day 9. (F) CD19+ B cell frequency in CD4-/CD8-/MHC-II+ cells.

Figure 65A demonstrates that while strong TCR+CAR stimulation outperforms strong TCR stimulation alone in four of the five tumor models tested, in both *in vitro* and *in vivo* settings and across multiple CAR antigens and costimulatory domains, it fails to do so in the B16-CD19

+ OT-1 TCR/CD19 CAR T-cell system *in vivo*. Notably though, E2aPBX tumors *in vivo*, which were also treated with OT-1 TCR/CD19 CAR T-cells, do follow the general expected trend of strong TCR+CAR stimulation being superior to strong TCR stimulation alone, implying that the basis for the discrepancy does not stem from an inherent issue with OT-1/CAR T-cells. We therefore turned to *in vitro* models of both tumor types to better elucidate the reasons underlying the lower performance of OT-1/CAR T-cells against B16-CD19 tumors *in vivo*. Intriguingly, we found that *in vitro*, both E2aPBX cells (Figure 65B) and B16-CD19 cells (Figure 65C) are killed more effectively by T-cells experiencing strong TCR+CAR stimulation than those that experience strong TCR stimulation alone. This observation suggested this issue was specific to the B16-CD19 tumor in the context of a B6 mouse model. Previous studies have implicated endogenous B cells as a critical factor in impeding B16 tumor growth in B6 mice [108], so we hypothesized that on-target/off-tumor toxicity by OT-1/CAR T-cells against endogenous CD19+ B cells may be limiting mouse survival. Indeed, the Rag1-/- mouse model used for the E2aPBX studies exhibited stronger TCR+CAR killing relative to TCR or CAR killing, but lacked a targetable B cell population, potentially explaining the basis for the discrepancies between the two tumor types. We therefore examined the splenocyte compartment at D+8 after T-cell injection in the B16-CD19 model (D+9 after irradiation) and observed a marked decrease in MHC-II+ cells after OT-1/CAR T-cell treatment compared to OT-1 T-cell treatment (Figure 65D). Independent experiments confirmed that the majority of these MHC-II+ splenocytes were CD19+ B-cells (Figure 65E,F), validating our hypothesis. Thus, the data suggest that, specifically in this *in vivo* B16-CD19 model, OT-1/CAR treatment reduced endogenous B-cell frequencies, resulting in lower anti-tumor activity of OT-1/CAR T-cells compared to OT-1 TCR-only T-cells. While a "true" AEBS therapy that is antagonized by a ubiquitously expressed self antigen should in theory be able to circumvent this limitation, the above findings underscore the importance of conducting rigorous *in vivo* testing in syngeneic mouse models to confirm that this type of off-target homing does not occur.

In addition to this homing constraint, AEBS therapy can also display significant donor to donor variability, as shown in Figure 66 below.

Figure 66 shows that all four donors of transferred T-cells, healthy BEAS-2B tissue was more negatively impacted by the transfer of HER2 CAR T-cells than by AEBS T-cells. However, while

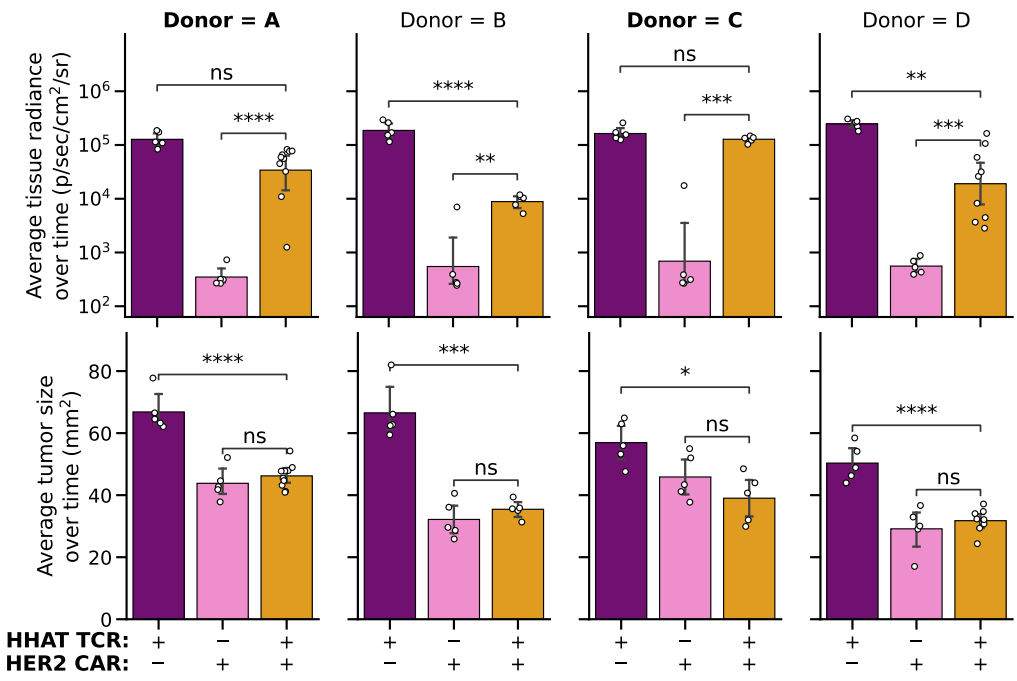

Figure 66: **Variability Limitation** Average healthy tissue (BEAS-2B) abundance evaluated by bioluminescent imaging (top), and average tumor size over time (bottom) in mice treated with engineered T-cells from four individual donors shows significant correlated donor to donor variability.

the OTOT toxicity of AEBS T-cells was equivalent to that of HHAT TCR T-cells for two donors, in the other two donors, OTOT toxicity was higher in AEBS-T cells. Intriguingly, these donor to donor variations seemed to correlate with the general potency of the CAR against the tumor. The donors where TCR-T and AEBS-T treatment exhibited equally low levels of off-target toxicity (Donors A and C, Figure 66 top) also had the lower on-target tumor killing with their CAR+ T cells (Donors A and C, Figure 66 bottom) than the donors where TCR-T cells exhibited lower off-target toxicity than AEBS-T cells (Donors B and D, Figure 66). These results imply that careful tuning of the level of CAR T efficacy may be required in order to maximize the safety benefit of AEBS-T cells; an extremely potent CAR may be difficult to constrain through TCR/CAR antagonism alone.

The quantitative model of TCR/CAR interaction created in **Chapter 3** could potentially be harnessed to accomplish the initial steps of this type of tuning *in silico*. Figure 67 below shows an example of how the model can be used to predict the effect of using CARs with different affinities on TCR/CAR crosstalk.

Figure 67A displays how modulating the affinity of the CAR vs the TCR used in an AEBS

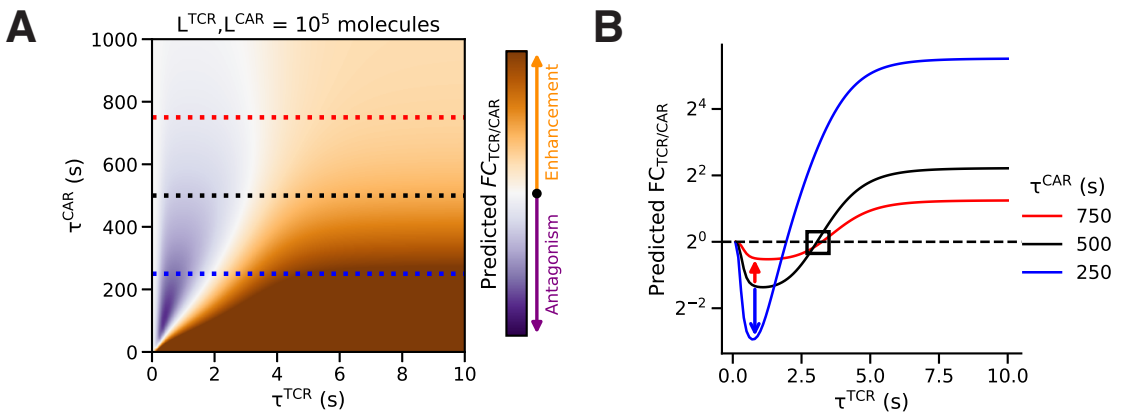

Figure 67: ***in silico* modeling of CAR affinity modulation.** (A) We tested our model with large numbers of both ligands (10^5 molecules) and found that antagonism/enhancement of CAR signaling was possible in a large swath of affinities of the CAR and TCR (as modulated by changing τ_{CAR} and τ_{TCR}).(B) The amplitude of the cross-talk and the exact choice of the TCR antigen to maximally antagonize CAR signaling requires some fine tuning.

system impacts overall level of TCR/CAR crosstalk. In Figure 67B, we clearly see that the impact of increasing scFv affinity (e.g. increasing half-life τ for the CAR+CAR ligand complex above the original 500s) in our current model has a negative impact on the magnitude of TCR/CAR crosstalk at a given level of TCR affinity. On the other hand, decreasing scFv affinity (implying a shorter half-life for the CAR+CAR ligand complex) decreased the range of TCR affinities that cause antagonism while simultaneously increasing the level of antagonism. This type of fine tuning of CAR affinity could in the future be employed to maximize the level of TCR/CAR antagonism observed against healthy tissue across patients.

However, even within a single donor, AEBS therapy offers significant, but incomplete, inhibition of the CAR when exposed to physiological levels of antagonist on healthy tissue, as shown in Figure 68 below.

Figure 68A shows how for a given donor, AEBS-T therapy outperforms both CAR-T and TCR-T therapy at killing a tumor expressing mutant P53, potentially due to the low levels of each target ligand (Figure 68B). When this same donor's T cells are cocultured with cells expressing the wildtype P53, TCR/CAR antagonism is unable to completely return the level of killing of this celltype to the baseline level seen with conventional TCR-T treatment (Figure 68C), though these AEBS-T cells still exhibit dramatically reduced off-target toxicity than conventional CAR-T

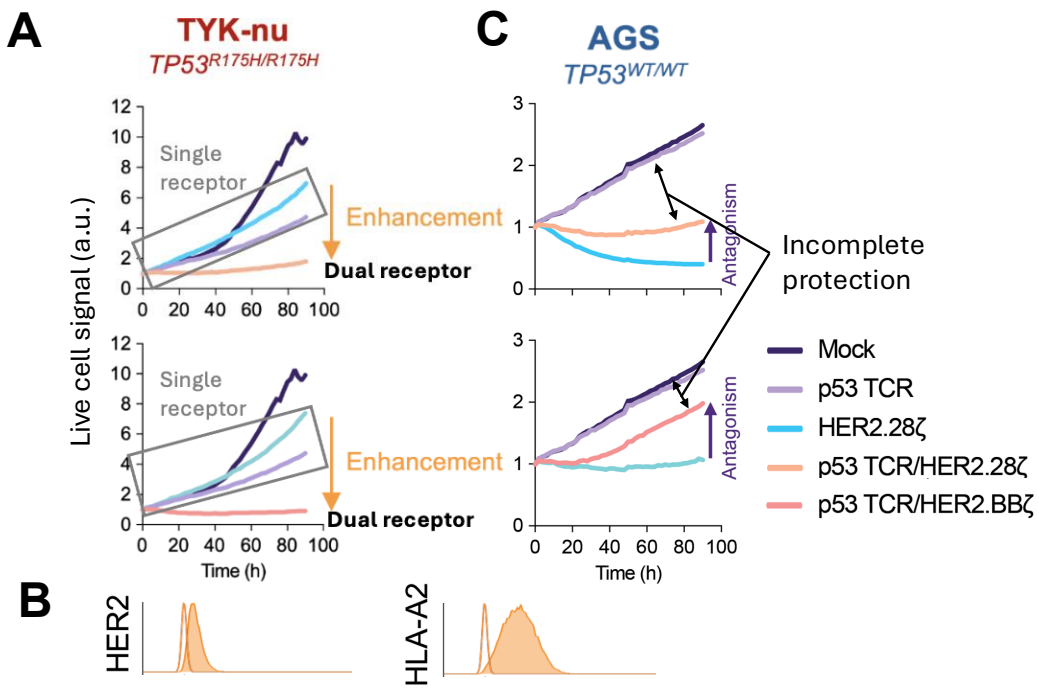

Figure 68: **Crosstalk Limitation** (A) AEBS CAR T cells exhibit improved *on-target* killing compared to both TCR+ and CAR+ cells against Tyk-nu tumors, potentially due to (B) low levels of each individual antigen on this tumor, but (C) only exhibit less *off-target* toxicity than CAR+ T cells, not TCR+ T cells, in the AGS tumor cell line

cells. Further work will be required to engineer a truly "best in class" treatment that outperforms conventional immunotherapies at both on-target tumor killing **and** off-target toxicity.

6.5 High throughput unraveling of the molecular components of TCR/CAR crosstalk

Overcoming the set of AEBS limitations described above will require deeper mechanistic insight into TCR/CAR crosstalk. The results of the colocalization and signaling molecule experiments we undertook in **Chapter 4** gave us initial indications of the importance of understanding how conventional components of the immune system interact with one another when induced by two very different receptors simultaneously. However, gaining a true understanding of how the CAR and TCR signaling networks, shown in Figure 69 below, interact with one another will require a more high throughput, unbiased interactomics approach.

T cells concurrently express 200-300 unique receptors [111], many of which are integrated along-

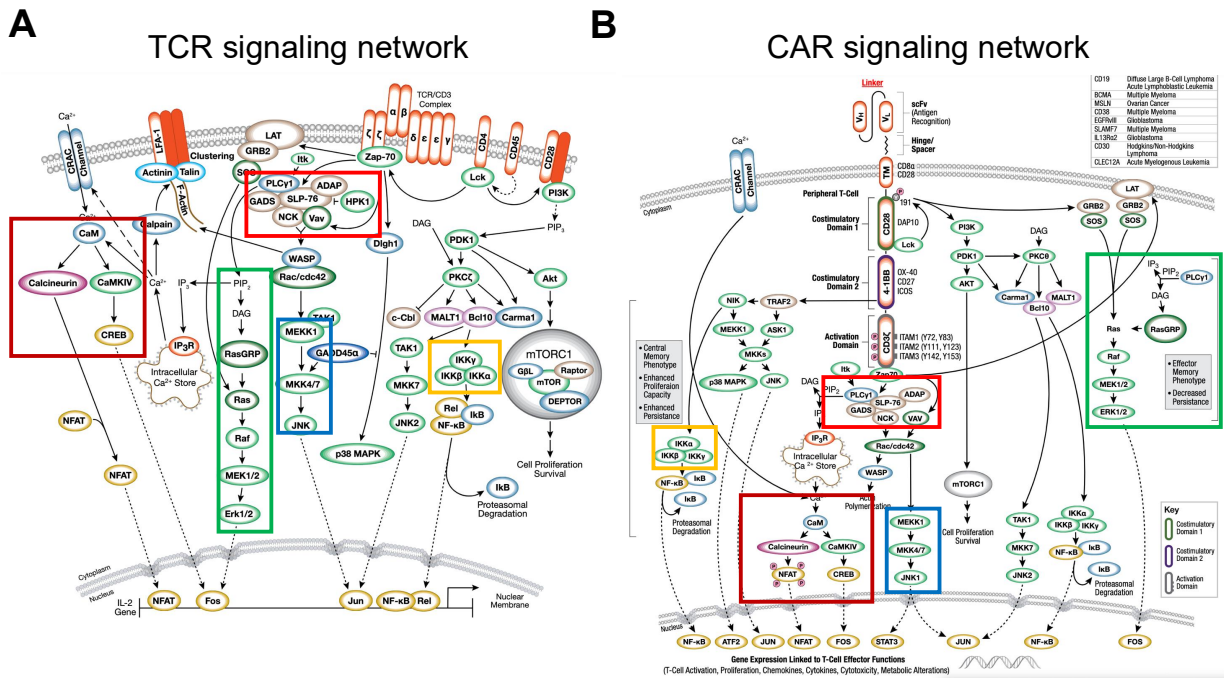

Figure 69: **TCR vs CAR signaling network comparison, adapted from Cell Signaling Technology website pages [109] and [110]** (A) TCR and (B) CAR signaling networks share the majority of their signaling pathways. A representative set of examples of this commonality are shown with matched color rectangles.

side the TCR (e.g., PD-1, CD2, Lag-3), and have differential impacts on many of the key members of the signaling networks in Figure 69, most of which are shared among the two receptors. How the presence of these surface receptors influences TCR/CAR antagonism is not known. We therefore plan to systematically examine how crosstalk between other receptors regulates TCR/CAR antagonism, using an arrayed CRISPR screen [112] to individually ablate surface receptors on a target cancer cell, and then test their effect on TCR/CAR antagonism. A key benefit is that arrayed screens enable rapid quantification of dose-response curves to different TCR stimuli; a requisite for exploring regulators of TCR/CAR antagonism.

Ultimately, through a combination of high throughput robotics, quantitative *in silico* modeling, targeted molecular perturbations, and structural optimizations, we hope to potentially improve crosstalk between the TCR and CAR even further, paving the way for the translation of AEBS CAR T cell therapy into the clinic.

References

[1] Sooraj R. Achar *et al.* "Universal antigen encoding of T cell activation from high-dimensional cytokine dynamics". *Science* 376.6595 (2022).

[2] Taisuke Kondo *et al.* "Engineering TCR-controlled fuzzy logic into CAR T cells enhances therapeutic specificity". *Cell* 188.9 (2025).

[3] Guillaume Gaud *et al.* "CD3ζ ITAMs enable ligand discrimination and antagonism by inhibiting TCR signaling in response to low-affinity peptides". *Nature Immunology* 24.12 (2023).

[4] Adam L. Kenet *et al.* "The 1000+ mouse project: large-scale spatiotemporal parametrization and modeling of preclinical cancer immunotherapies". *eLife* 14 (2025).

[5] Johannes Pettmann *et al.* "The discriminatory power of the T cell receptor". *eLife* 10 (2021).

[6] Lukas Sušac *et al.* "Structure of a fully assembled tumor-specific T cell receptor ligated by pMHC". *Cell* 185.17 (2022).

[7] Jason R. Devlin *et al.* "Structural dissimilarity from self drives neoepitope escape from immune tolerance". *Nature Chemical Biology* 16.11 (2020).

[8] Jun Huang *et al.* "A single peptide-major histocompatibility complex ligand triggers digital cytokine secretion in CD4+ T cells". *Immunity* 39.5 (2013).

[9] Baoyu Liu *et al.* "Accumulation of dynamic catch bonds between TCR and agonist peptide-MHC triggers T cell signaling". *Cell* 157.2 (2014).

[10] John R. James and Ronald D. Vale. "Biophysical Mechanism of T Cell Receptor Triggering in a Reconstituted System". *Nature* 487.7405 (2012).

[11] Derek M Britain *et al.* "Progressive enhancement of kinetic proofreading in T cell antigen discrimination from receptor activation to DAG generation". *eLife* 11 (2022).

[12] Doug K Tischer and Orion David Weiner. "Light-based tuning of ligand half-life supports kinetic proofreading model of T cell signaling". *eLife* 8 (2019).

[13] G. J. Kersh *et al.* "High- and low-potency ligands with similar affinities for the TCR: the importance of kinetics in TCR signaling". *Immunity* 9.6 (1998).

[14] E. N. Kersh *et al.* "Fidelity of T cell activation through multistep T cell receptor zeta phosphorylation". *Science* 281.5376 (1998).

[15] D. Aivazian and L. J. Stern. "Phosphorylation of T cell receptor zeta is regulated by a lipid dependent folding transition". *Nature Structural Biology* 7.11 (2000).

[16] Lisa A. Pitcher and Nicolai S. C. van Oers. "T-cell receptor signal transmission: who gives an ITAM?" *Trends in Immunology* 24.10 (2003).

[17] Guillaume Voisinne *et al.* "Kinetic proofreading through the multi-step activation of the ZAP70 kinase underlies early T cell ligand discrimination". *Nature Immunology* 23.9 (2022).

[18] J. J. Hopfield. "Kinetic Proofreading: A New Mechanism for Reducing Errors in Biosynthetic Processes Requiring High Specificity". *Proceedings of the National Academy of Sciences* 71.10 (1974).

[19] Jacques Ninio. "Kinetic amplification of enzyme discrimination". *Biochimie* 57.5 (1975).

[20] Tillmann Pape *et al.* "Induced fit in initial selection and proofreading of aminoacyl-tRNA on the ribosome". *The EMBO Journal* 18.13 (1999).

[21] M. J. Donlin *et al.* "Kinetic partitioning between the exonuclease and polymerase sites in DNA error correction". *Biochemistry* 30.2 (1991).

[22] Sean M. Burgess and Christine Guthrie. "A mechanism to enhance mRNA splicing fidelity: The RNA-dependent ATPase Prp16 governs usage of a discard pathway for aberrant lariat intermediates". *Cell* 73.7 (1993).

[23] T W McKeithan. "Kinetic proofreading in T-cell receptor signal transduction." *Proceedings of the National Academy of Sciences* 92.11 (1995).

[24] Caridad Rosette *et al.* "The Impact of Duration versus Extent of TCR Occupancy on T Cell Activation: A Revision of the Kinetic Proofreading Model". *Immunity* 15.1 (2001).

[25] Christopher C. Govern *et al.* "Fast on-rates allow short dwell time ligands to activate T cells". *Proceedings of the National Academy of Sciences* 107.19 (2010).

[26] Melissa Lever *et al.* "Architecture of a minimal signaling pathway explains the T-cell response to a 1 million-fold variation in antigen affinity and dose". *Proceedings of the National Academy of Sciences* 113.43 (2016).

[27] Kathryn M. Armstrong *et al.* "Conformational changes and flexibility in T-cell receptor recognition of peptide–MHC complexes". *Biochemical Journal* 415.Pt 2 (2008).

[28] Simon J. Davis and P. Anton van der Merwe. "The kinetic-segregation model: TCR triggering and beyond". *Nature Immunology* 7.8 (2006).

[29] Kaushik Choudhuri *et al.* "T-cell receptor triggering is critically dependent on the dimensions of its peptide-MHC ligand". *Nature* 436.7050 (2005).

[30] Veronica T. Chang *et al.* "Initiation of T cell signaling by CD45 segregation at 'close contacts'". *Nature Immunology* 17.5 (2016).

[31] Alexander S. Moffett *et al.* "Comparing kinetic proofreading and kinetic segregation for T cell receptor activation". *Physical Review Research* 7.2 (2025).

[32] Lauren E. Stopfer *et al.* "Absolute quantification of tumor antigens using embedded MHC-I isotopologue calibrants". *Proceedings of the National Academy of Sciences* 118.37 (2021).

[33] Lauren E. Stopfer *et al.* "Multiplexed relative and absolute quantitative immunopeptidomics reveals MHC I repertoire alterations induced by CDK4/6 inhibition". *Nature Communications* 11.1 (2020).

[34] Grégoire Altan-Bonnet and Ronald N. Germain. "Modeling T Cell Antigen Discrimination Based on Feedback Control of Digital ERK Responses". *PLOS Biology* 3.11 (2005).

[35] D. R. Plas *et al.* "Direct regulation of ZAP-70 by SHP-1 in T cell antigen receptor signaling". *Science* 272.5265 (1996).

[36] Joanne Sloan-Lancaster *et al.* "Partial T cell signaling: Altered phospho-ζ and lack of zap70 recruitment in APL-induced T cell anergy". *Cell* 79.5 (1994).

[37] C Reis e Sousa *et al.* "Partial signaling by CD8+ T cells in response to antagonist ligands." *Journal of Experimental Medicine* 184.1 (1996).

[38] Joaquín Madrenas *et al.* "ζ Phosphorylation Without ZAP-70 Activation Induced by TCR Antagonists or Partial Agonists". *Science* 267.5197 (1995).

[39] Ellen N. Kersh *et al.* "Partially Phosphorylated T Cell Receptor ζ Molecules Can Inhibit T Cell Activation". *Journal of Experimental Medicine* 190.11 (1999).

[40] B. N. Dittel *et al.* "Cross-antagonism of a T cell clone expressing two distinct T cell receptors". *Immunity* 11.3 (1999).

[41] Ronald N. Germain and Irena Stefanová. "THE DYNAMICS OF T CELL RECEPTOR SIGNALING: Complex Orchestration and the Key Roles of Tempo and Cooperation1". *Annual Review of Immunology* 17 (1999).

[42] Irena Štefanová *et al.* "TCR ligand discrimination is enforced by competing ERK positive and SHP-1 negative feedback pathways". *Nature Immunology* 4.3 (2003).

[43] Ofer Feinerman *et al.* "Variability and Robustness in T Cell Activation from Regulated Heterogeneity in Protein Levels". *Science* 321.5892 (2008).

[44] Paul François *et al.* "Phenotypic model for early T-cell activation displaying sensitivity, specificity, and antagonism". *Proceedings of the National Academy of Sciences* 110.10 (2013).

[45] Jean-Benoît Lalanne and Paul François. "Principles of Adaptive Sorting Revealed by In Silico Evolution". *Physical Review Letters* 110.21 (2013).

[46] S. Mangan and U. Alon. "Structure and function of the feed-forward loop network motif". *Proceedings of the National Academy of Sciences* 100.21 (2003).

[47] Wenzhe Ma *et al.* "Defining Network Topologies that Can Achieve Biochemical Adaptation". *Cell* 138.4 (2009).

[48] Gautam Reddy *et al.* "Antagonism in olfactory receptor neurons and its implications for the perception of odor mixtures". *eLife* 7 (2018).

[49] C. Torigoe *et al.* "An unusual mechanism for ligand antagonism". *Science* 281.5376 (1998).

[50] Paul François *et al.* "Phenotypic spandrel: absolute discrimination and ligand antagonism". *Physical Biology* 13.6 (2016).

[51] Raman S. Ganti *et al.* "How the T cell signaling network processes information to discriminate between self and agonist ligands". *Proceedings of the National Academy of Sciences* 117.42 (2020).

[52] M. T. De Magistris *et al.* "Antigen analog-major histocompatibility complexes act as antagonists of the T cell receptor". *Cell* 68.4 (1992).

[53] J. Alexander *et al.* "Functional consequences of engagement of the T cell receptor by low affinity ligands". *Journal of Immunology* 150.1 (1993).

[54] J. Ruppert *et al.* "Effect of T-cell receptor antagonism on interaction between T cells and antigen-presenting cells and on T-cell signaling events". *Proceedings of the National Academy of Sciences* 90.7 (1993).

[55] Stephen C. Jameson and Michael J. Bevan. "T cell receptor antagonists and partial agonists". *Immunity* 2.1 (1995).

[56] Paul Klenerman *et al.* "Cytotoxic T-cell activity antagonized by naturally occurring HIV-1 Gag variants". *Nature* 369.6479 (1994).

[57] Antonio Bertoletti *et al.* "Natural variants of cytotoxic epitopes are T-cell receptor antagonists for antiviral cytotoxic T cells". *Nature* 369.6479 (1994).

[58] A. Franco *et al.* "T cell receptor antagonist peptides are highly effective inhibitors of experimental allergic encephalomyelitis". *European Journal of Immunology* 24.4 (1994).

[59] D. Basu *et al.* "In vivo antagonism of a T cell response by an endogenously expressed ligand". *Proceedings of the National Academy of Sciences* 95.24 (1998).

[60] L. Kappos *et al.* "Induction of a non-encephalitogenic type 2 T helper-cell autoimmune response in multiple sclerosis after administration of an altered peptide ligand in a placebo-controlled, randomized phase II trial. The Altered Peptide Ligand in Relapsing MS Study Group". *Nature Medicine* 6.10 (2000).

[61] B. Bielekova *et al.* "Encephalitogenic potential of the myelin basic protein peptide (amino acids 83-99) in multiple sclerosis: results of a phase II clinical trial with an altered peptide ligand". *Nature Medicine* 6.10 (2000).

[62] Omid Sascha Yousefi *et al.* "Cross-TCR Antagonism Revealed by Optogenetically Tuning the Half-Life of the TCR Ligand Binding". *International Journal of Molecular Sciences* 22.9 (2021).

[63] Carl H. June and Michel Sadelain. "Chimeric Antigen Receptor Therapy". *New England Journal of Medicine* 379.1 (2018).

[64] David L. Porter *et al.* "Chimeric antigen receptor-modified T cells in chronic lymphoid leukemia". *New England Journal of Medicine* 365.8 (2011).

[65] Shannon L. Maude *et al.* "Tisagenlecleucel in Children and Young Adults with B-Cell Lymphoblastic Leukemia". *New England Journal of Medicine* 378.5 (2018).

[66] Grace Guzman *et al.* "CAR-T Therapies in Solid Tumors: Opportunities and Challenges". *Current Oncology Reports* 25.5 (2023).

[67] Carl H. June *et al.* "CAR T cell immunotherapy for human cancer". *Science* 359.6382 (2018).

[68] Jingming Luo and Xianwen Zhang. "Challenges and innovations in CAR-T cell therapy: a comprehensive analysis". *Frontiers in Oncology* 14 (2024).

[69] Elizabeth R. Hawkins *et al.* "Armored CAR T-Cells: The Next Chapter in T-Cell Cancer Immunotherapy". *Biologics: Targets & Therapy* 15 (2021).

[70] Joseph H. Choe *et al.* "SynNotch-CAR T cells overcome challenges of specificity, heterogeneity, and persistence in treating glioblastoma". *Science Translational Medicine* 13.591 (2021).

[71] Aidan M. Tousley *et al.* "Co-opting signalling molecules enables logic-gated control of CAR T cells". *Nature* 615.7952 (2023).

[72] Theresa L. Hunter *et al.* "In vivo CAR T cell generation to treat cancer and autoimmune disease". *Science* 388.6753 (2025).

[73] Maysoon Al-Haideri *et al.* "CAR-T cell combination therapy: the next revolution in cancer treatment". *Cancer Cell International* 22 (2022).

[74] Lei Peng *et al.* "CAR-T and CAR-NK as cellular cancer immunotherapy for solid tumors". *Cellular & Molecular Immunology* 21.10 (2024).

[75] Sophia Chen and Marcel R. M. van den Brink. "Allogeneic "Off-the-Shelf" CAR T cells: Challenges and advances". *Best Practice & Research. Clinical Haematology* 37.3 (2024).

[76] Waseem Qasim *et al.* "Molecular remission of infant B-ALL after infusion of universal TALEN gene-edited CAR T cells". *Science Translational Medicine* 9.374 (2017).

[77] Frederick L. Locke *et al.* "Allogeneic Chimeric Antigen Receptor T-Cell Products Cemacabtagene Ansegedleucel/ALLO-501 in Relapsed/Refractory Large B-Cell Lymphoma: Phase I Experience From the ALPHA2/ALPHA Clinical Studies". *Journal of Clinical Oncology* 43.14 (2025).

[78] Joseph P. McGuirk *et al.* "CTX110 Allogeneic CRISPR-Cas9-Engineered CAR T Cells in Patients (Pts) with Relapsed or Refractory (R/R) Large B-Cell Lymphoma (LBCL): Results from the Phase 1 Dose Escalation Carbon Study". *Blood* 140.Supplement 1 (2022).

[79] L. J. Nastoupil *et al.* "P1455: FIRST-IN-HUMAN TRIAL OF CB-010, A CRISPR-EDITED ALLOGENEIC ANTI-CD19 CAR -T CELL THERAPY WITH A PD-1 KNOCK OUT, IN PATIENTS WITH RELAPSED OR REFRACTORY B CELL NON-HODGKIN LYMPHOMA (ANTLER STUDY)". *HemaSphere* 6.Suppl (2022).

[80] Justin Eyquem *et al.* "Targeting a CAR to the TRAC locus with CRISPR/Cas9 enhances tumour rejection". *Nature* 543.7643 (2017).

[81] Dana Stenger *et al.* "Endogenous T-cell receptor promotes in vivo persistence of CD19-CAR-T cells compared to a CRISPR/Cas9-mediated T-cell receptor knockout CAR". *Blood* 136.12 (2020).

[82] Alexander I. Salter *et al.* "Comparative analysis of TCR and CAR signaling informs CAR designs with superior antigen sensitivity and in vivo function". *Science Signaling* 14.697 (2021).

[83] Alena Gros *et al.* "PD-1 identifies the patient-specific CD8+ tumor-reactive repertoire infiltrating human tumors". *The Journal of Clinical Investigation* 124.5 (2014).

[84] Thomas Duhen *et al.* "Co-expression of CD39 and CD103 identifies tumor-reactive CD8 T cells in human solid tumors". *Nature Communications* 9.1 (2018).

[85] Andrew Chow *et al.* "The ectonucleotidase CD39 identifies tumor-reactive CD8+ T cells predictive of immune checkpoint blockade efficacy in human lung cancer". *Immunity* 56.1 (2023).

[86] Ilya Korsunsky *et al.* "Fast, sensitive and accurate integration of single-cell data with Harmony". *Nature Methods* 16.12 (2019).

[87] Shobana V Stassen *et al.* "PARC: ultrafast and accurate clustering of phenotypic data of millions of single cells". *Bioinformatics* 36.9 (2020).

[88] Michael L. Dustin. "The immunological synapse". *Cancer Immunology Research* 2.11 (2014).

[89] Arash Grakoui *et al.* "The Immunological Synapse: A Molecular Machine Controlling T Cell Activation". *Science* 285.5425 (1999).

[90] S. E. Lindner *et al.* "Chimeric antigen receptor signaling: Functional consequences and design implications". *Science Advances* 6.21 (2020).

[91] Michael L. Dustin and Eric O. Long. "Cytotoxic immunological synapses". *Immunological Reviews* 235.1 (2010).

[92] A. J. Davenport *et al.* "Chimeric antigen receptor T cells form nonclassical and potent immune synapses driving rapid cytotoxicity". *Proceedings of the National Academy of Sciences* 115.9 (2018).

[93] Shannon F. Rosati *et al.* "A Novel Murine T-Cell Receptor Targeting NY-ESO-1". *Journal of Immunotherapy* 37.3 (2014).

[94] Kyle G. Daniels *et al.* "Decoding CAR T cell phenotype using combinatorial signaling motif libraries and machine learning". *Science* 378.6625 (2022).

[95] Yue Liu *et al.* "Chimeric STAR receptors using TCR machinery mediate robust responses against solid tumors". *Science Translational Medicine* 13.586 (2021).

[96] Marta Łuksza *et al.* "Neoantigen quality predicts immunoediting in survivors of pancreatic cancer". *Nature* 606.7913 (2022).

[97] Richard A. Morgan *et al.* "Case report of a serious adverse event following the administration of T cells transduced with a chimeric antigen receptor recognizing ERBB2". *Molecular Therapy: The Journal of the American Society of Gene Therapy* 18.4 (2010).

[98] Eric A. Collisson *et al.* "Comprehensive molecular profiling of lung adenocarcinoma". *Nature* 511.7511 (2014).

[99] Maribel Soto-Nava *et al.* "Weaker HLA Footprints on HIV in the Unique and Highly Genetically Admixed Host Population of Mexico". *Journal of Virology* 92.2 (2018).

[100] Gaurav Mendiratta *et al.* "Cancer gene mutation frequencies for the U.S. population". *Nature Communications* 12.1 (2021).

[101] Evan H Baugh *et al.* "Why are there hotspot mutations in the TP53 gene in human cancers?" *Cell Death and Differentiation* 25.1 (2018).

[102] Liang Zhang *et al.* "p53 inhibits the expression of p125 and the methylation of POLD1 gene promoter by downregulating the Sp1-induced DNMT1 activities in breast cancer". *OncoTargets and Therapy* 9 (2016).

[103] Winifred Lo *et al.* "Immunologic Recognition of a Shared p53 Mutated Neoantigen in a Patient with Metastatic Colorectal Cancer". *Cancer Immunology Research* 7.4 (2019).

[104] Rand Arafeh *et al.* "The present and future of the Cancer Dependency Map". *Nature Reviews. Cancer* 25.1 (2025).

[105] Ricard Solé *et al.* "Liquid brains, solid brains". *Philosophical Transactions of the Royal Society B: Biological Sciences* 374.1774 (2019).

[106] Haneen Shalabi *et al.* "CD19/22 CAR T cells in children and young adults with B-ALL: phase 1 results and development of a novel bicistronic CAR". *Blood* 140.5 (2022).

[107] Sourish Ghosh *et al.* "β-Coronaviruses Use Lysosomes for Egress Instead of the Biosynthetic Secretory Pathway". *Cell* 183.6 (2020).

[108] Sheng Guo *et al.* "The design, analysis and application of mouse clinical trials in oncology drug development". *BMC Cancer* 19.1 (2019).

[109] Cell Signaling Technology. *T Cell Receptor (TCR) Signaling Pathway.*

[110] Cell Signaling Technology. *Chimeric Antigen Receptor (CAR) Signaling Pathway.*

[111] Anke Graessel *et al.* "A Combined Omics Approach to Generate the Surface Atlas of Human Naive CD4+ T Cells during Early T-Cell Receptor Activation". *Molecular & Cellular Proteomics* 14.8 (2015).

[112] Jiang-An Yin *et al.* "Arrayed CRISPR libraries for the genome-wide activation, deletion and silencing of human protein-coding genes". *Nature Biomedical Engineering* 9.1 (2025).